STUDY OF THE MAGNETO- AND ELECTRO-PROPERTIES IN AN ALL-OXIDE JUNCTION DEVICE

LI MING KEI

M.Phil

The Hong Kong Polytechnic University

2011

The Hong Kong Polytechnic University

Department of Applied Physics

STUDY OF THE MAGNETO- AND ELECTRO-PROPERTIES IN AN ALL-OXIDE JUNCTION DEVICE

LI Ming Kei

A thesis submitted in partial fulfillment of

the requirements for the degree of

Master of Philosophy

September 2010

CERTIFICATE OF ORIGINALITY

I hereby declare that this thesis is my own work and that, to the best of my knowledge and belief, it reproduces no material previously published or written, nor material that has been accepted for the award of any other degree or diploma, except where due acknowledgement has been made in the text.

_____ (Signed)

LI MING KEI (Name of student)

Abstract

This project attempts to realize an all-oxide junction device that integrates the electric field modulation of a p-n junction diode with the magnetic field modulation of a spin valve in the same unit. This study envisages manipulation of the spin variable of electrons to control their transport in a p-n junction, in contrast to conventional electronics, which use only the charge property. Theoretically, there are certain advantages of spintronics over electronics, some of which emanate from longer spin relaxation lifetimes and diffusion lengths as compared to charge momentum relaxation times and lengths. These advantages, however, can only be harnessed if the corresponding devices can be realized in practice.

The physical characteristics of oxide systems cover a broad range of interesting properties, such as ferroelectricity, high permittivity, piezoelectricity, photoelectricity, superconductivity and magnetoresistance, which have attracted the attention of technologists for quite some time. Many oxides are intrinsic semiconductors or can become good semiconductors by proper doping or by variation of their composition. In our study, we focus primarily on the exploration of thin films and device configurations involving ferromagnetic oxides with high spin polarization. Indeed, ferromagnetic

oxides such as manganates have been used to make spin valves in recent years. At the same time, there is considerable emphasis in materials research on tailoring the magnetic properties of functional nonmagnetic materials by introducing a dilute concentration of magnetic impurities therein. This material is thereby a potential candidate in spintronics with the benefits of magnetic response and the application bearing attractive properties of the non-magnetic host.

At the beginning of our project, $La_{0.7}Sr_{0.3}MnO_3$ (LSMO) and cobalt doped titanium dioxide were identified as suitable materials for our study. Heteroepitaxial junctions formed by *p*-type strontium doped lanthanum manganite and *n*-type cobalt doped titanium dioxide were fabricated on LAO (100) substrates by pulsed laser deposition. The layers were grown at 650^0C and under 150 mTorr ambient oxygen pressure. The $Co_xTi_{1-x}O_2$[x = 0.05 and 0.1] (CTO), which, at anatase phase, was reported as a wide-band-gap dilute magnetic semiconductor, were deposited on the LSMO film surface at 600^0C with an ambient oxygen pressure of 20 mTorr. The as-grown CTO films exhibited pure anatase crystalline phase and semiconductor-like conduction. Under optimized fabrication conditions the CTO/LSMO junction revealed a heteroepitaxial relationship of $(004)_{CTO}||(001)_{LSMO}||(001)_{LAO}$. Electrical characterization of these p-n junctions yielded excellent rectifying characteristics with a current

rectifying ratio over 1000 at room temperature. The electrical transport across these diodes was dominated by diffusion at low current (low bias voltage) regime and by recombination at high current (high bias voltage) regime.

Our results have demonstrated an all-oxide junction diode with good transport property. The simultaneous of electrical and magnetic modulation in a diode junction is therefore potentially realizable. LMSO showed room temperature ferromagnetism and metallic-like electrical conduction with a resistivity of 0.015 ohm cm at 300 K. Nevertheless, since the magnetization of CTO is very close to the detection limit of our equipment, we have yet to demonstrate the simultaneous electric and magnetic modulation with this combination. Therefore, we have explored other n-type ferromagnetic oxide as an alternative to CTO.

Carbon doped TiO_2 was one of the candidates investigated in our study. It is predicted that ferromagnetism at room temperature can occur in titanium dioxide with this non-magnetic dopant, carbon. As we have prepared specimen with different concentration of carbon, it was confirmed that they all showed ferromagnetic property under the vibrating sample measurement. On the other hand, the conductivity of carbon doped TiO_2 was improved at least two orders of magnitude when compared with pure

TiO_2. A further step is to look into the possibility of formation of p-n junction by using carbon doped TiO_2 and LSMO.

Other than diluted magnetic semiconductors, cobalt ferrite $CoFe_2O_4$ (CFO) has also been studied successfully. We have demonstrated that CFO can be epitaxially grown on LSMO. Double coercivity of CFO/LSMO was observed. It indicated that the junction was magnetized in two stages. The magnetoresistance response of this combination has been evaluated. As the magnetic field was decreased from 5000 to -80 G, the resistance of these heteroepitaxial junctions increased MR ratio = 6%. These changes are corresponded to the switching of LSMO magnetization, which gives result in the change of parallel to anti-parallel magnetization in the CFO and LSMO layer.

Publication

M. K. Li & K. H. Wong, "Structural and Electrical Properties of Heteroepitaxial Magnetic Oxide Junction Diode Fabricated by Pulsed Laser Deposition," *AIP Conference Proceeding*, vol 1292, p. 201 – 204, 2010.

Acknowledgements

This thesis is based on the experimental work carried out in the department of Applied Physics, The Hong Kong Polytechnic University, during the years of 2008-2010.

I sincerely express my deep gratitude to my supervisor Prof. K.H. Wong for his invaluable guidance, encouragement and continuous support throughout the whole period of my research study. I truly appreciate for the opportunity Prof. Wong has given me. His advice and assistance over the past three years has been a tremendous asset in my research career.

I would like to extend my gratitude Dr. C.W. Leung for his suggestions during many experiments. I thank him for his patience shown in repeatedly explaining concepts and phenomena from different perspectives. I have learned a tremendous amount from him during this study. His contribution was essential in this work.

My genuine thanks go to the academic members in our department: Dr. C. L. Mak for his insightful suggestions during the group meeting discussions, Prof. S. P. Lau for

his advice and generous assistance in every aspect of investigation on ferromagnetism in carbon-doped titanium dioxide and Dr Y. W. Wong for furnishing my experimental skills when I was a research assistant.

I am very grateful for being a member of pulsed laser deposition research group in Department of Applied Physics as I am always enlightened by the discussions and assistances in the research work with the team. I would like to express my thanks to the help of both present and previous members (in no particular order): Mr. H. F. Wong, Mr. H. K. Lau, Mr. C. H. Wong, Mr. Y. K. Chan, Mr. W. F. Cheng, Dr. P. F. Lee, Dr. C. Y. Lam, Dr. W. L. Sin, Dr. M. Zhang, Dr. Q. G. Zeng and Dr. J. Qiu.

I wish to acknowledge Mr. H. F. Wong for his advices and kind assistance in pulsed laser deposition and junction fabrication, Mr. H. K. Lau for his thoughtful assistance in AFM investigations, Mr. M. N. Yeung of the Materials Research Centre for his technical support in XRD investigations, Mr. C. S. Lo for his proficient assistance in SEM investigation, Mr. L. H. Chan for his assistance in VSM operation and Mr. W. M. Ho for his sophisticated work on sample preparations.

I would like to thank my former and present colleagues in our department for

sharing my happiness and burden no matters in my research work or personal life. They include: Mr. Y. M. Tang, Mr. C. K. Chow, Mr. S. M. Mok, Mr. H. F. Wong, Mr. W. K. Li, Miss W. F. Ng, Miss W. P. Suen, Mr. K. Wang, Mr. N. Y. Chan and Y. Y. Hui,

Also, I gratefully acknowledge the financial support from the Department of Applied Physics and the Hong Kong Research Grants Council. This study was supported by the Hong Kong Research Grants Council (Project codes: PolyU5022-08P), with the award of a research studentship by the Hong Kong Polytechnic University.

Last but not least, I would like to express my deepest appreciation to my family, especially my parents for their continuous love, endless support and patience that accomplish me to be mature both as a person and as a professional.

Table of Contents

Chapter 3

Chapter 4

Chapter 5

List of Figures

List of Acronyms

Acronyms	Description
AFM	Atomic force microscope
B	Magnetic flux density
CFO	Cobalt ferrite
CTO	Cobalt doped titanium dioxide
CMR	Colossal magnetoresistance
CPP	Current-Perpendicular-to-Plane
CTO	Cobalt doped titanium dioxide
DMS	Diluted magnetic semiconductor
EDX	Energy dispersive X-ray spectroscopy
FC	Field-cooled
FWHM	Full width at half maximum
H	Magnetic field strength
H_c	Coercivity
LAO	Lanthanum aluminate
LNO	Lanthanum nickel oxide
LCMO	Lanthanum calcium mangantie
LSMO	Lanthanum strontium manganite
M_r	Remanent magnetization
MR	Magnetoresistance
M_s	Saturation magnetization
SEM	Scanning electron microscope
T_c	Curie temperature
VSM	Vibrating sample magnetometer
XPS	X-ray photoelectron spectroscopy
XRD	X-ray diffraction
ZFC	Zero field-cooled

Chapter 1
Introduction

1.1 Motivation

In modern microelectronics industries, the “charge” degree of freedom of an electron has been utilized by manipulating a collective flow of current in metals or semiconductors among solid-state devices. The charges in electronic devices, such as a field effect transistor, are controlled by external electric fields. However, it has been known for several decades that electrons are also characterized by another quantum parameter, the “spin”, i.e. the spin angular momentum.

The electronic spin confers a magnetic moment on electrons, which can then be manipulated by magnetic fields as well as by electrical fields. In addition to the fundamental electronic charge in solid-state devices, a latest discipline of electronics, “spintronics”, also known as “magnetoelectronics”, brings the microelectronics into a new era by exploiting the spin degree of freedom and its associated magnetic moment.

Manifestations of the electronic spin are most notably found in ferromagnetic metals where an imbalance of populations near the Fermi level is responsible for spin-dependent electrical transport properties, i.e. the charge carriers are net spin-polarised. In fact, the modulation of a spin-polarised current in ferromagnetic metals by an external magnetic field has received intensive interest in both spintronics

applications and fundamental physics studies.

More recently, magnetoresistive effects in semiconductors, which would be compatible with the existing semiconductor technology, have also been arousing more interests. Spin manipulation in these magnetic semiconductors could involve not just magnetic fields but also some other types of spin dynamics controlled by polarized light or electric fields. Nevertheless, the manipulation of the spin states in such semiconductors is only prototypical, owing to the lack of effective ways to produce high spin injection and spin decoherence of the carriers.

The basic principles of spintronic devices rely on a variety of magnetoresistive (MR) effects that come from various physical origins. Historically, MR effects have been discovered in different materials systems and their physical bases have implications for technological developments.

The discoveries of giant magneto resistance (GMR) by Fert et. al. [1] in 1988 on hetero-structures that consist of alternating ferromagnetic and metallic thin films has aroused numerous studies on material systems with enhanced magneto-resistive response. Indeed, with the advancement in thin film fabrication technology, commercial devices based on GMR effect such as magnetic memory chips, magnetic field sensors and read heads have been available in the market.

The development of ferromagnetic functional oxide has generated much interest in

the possibility of magnetoelectronic devices. Spin-polarized transport in oxide based half-metals is being explored for potential applications in spintronics. The oxide systems have enormous range of desirable physical properties that can be applied in spin electronic devices such as spin valve, which is a three-layer device comprising a thin film of non-magnetic metal sandwiched between two films of ferromagnetic oxides.

The physical properties of oxide systems cover a broad range of interesting properties, which have attracted the attention of technologists for quite some time. However, oxides have not yet made the expected impact on the high technology sector, primarily due to a relatively poorer control on their growth and properties in thin film form. This situation appears to be changing quite rapidly with increased use of in situ growth characterization and control, and the growing recognition of the uniqueness and value of the novel electronic, magnetic, and optical responses of oxides in the context of modem micro and nanoelectronics.

Some of the most investigated half-metallic oxides include CrO_2, Fe_3O_4, double perovskites such as Sr_2FeMoO_6, and manganites $La_{1-x}Sr_xMnO_3$ (LSMO) for certain doping [2]. In particular, the perovskite manganites are highly desirable due to their fully spin polarized conduction bands, which favour the GMR effect. In addition, oxides are more tolerant towards extreme working conditions, making them attractive for wide

range of operations.

The perovskite manganite-based *p*-*n* junctions have in recent years attracted much attention because they exhibit good rectifying characteristics with magnetic tenability. It is expected that manganites interfaced with other kinds of oxides could be a promising way for making novel devices [3].

In close examination, the tri-layer spin valve has a very similar structure as the *p*-*n* junction diode. In fact, if the *p*-type and *n*-type conductors are both ferromagnetic, they will be virtually the same. The depletion layer in an oxide *p*-*n* junction is known to be very thin due to the stability of the oxide and the small thermal diffusion at the interface. The small thickness of the depletion layer of ~ 10 nm is exactly what is required for the spacer layer in tri-layer spin valve. A very interesting point is that by varying the reverse bias voltage of the all-oxide *p*-*n* junction we can tune the thickness of depletion layer (spacer layer) in order to optimize the spin polarized current through the spin valve, a feat that cannot be done otherwise. In the meanwhile, it reveals that some of the oxides used are common in both systems.

Indeed, it is the aim of most researchers in this field to have spintronics that integrate the electric field modulation of a p-n junction diode with the magnetic field modulation of a spin valve in the same unit. The realization of such an objective represents a major step forward in spintronic research. The demonstration of

simultaneous electric field and magnetic field induced switching can add new dimensions to device design and potentially lead to completely new breed of electronics.

1.2 Fundamentals of magnetism

The origins of magnetism lie in the motion of electrons orbiting the nucleus in an atom. The atoms that make up all matter contain moving electrons whose motions produce tiny magnetic fields in the space around them. When an electron travels with a uniform angular speed around a circle of radius r, the period of the motion is $2\pi/\omega$. So the current is $e\omega/2\pi$ and the magnitude of the magnetic moment is $\mu = (e\omega/2\pi)\pi r^2 = \frac{1}{2} e\omega r^2$ [4]. The direction of the moment is shown in Figure 1.1. The particle also possesses an intrinsic spin (s), which can be thought of as a rotation about its own axis [5]. This produces an associated, intrinsic magnetic moment. In most materials these individual currents are randomly oriented and there is no net, magnetic effect. But, in some materials, a field exerted by an external source can cause the microscopic magnets to align along the external field direction. The result is a net addition to the external field and the material is then described as being magnetized.

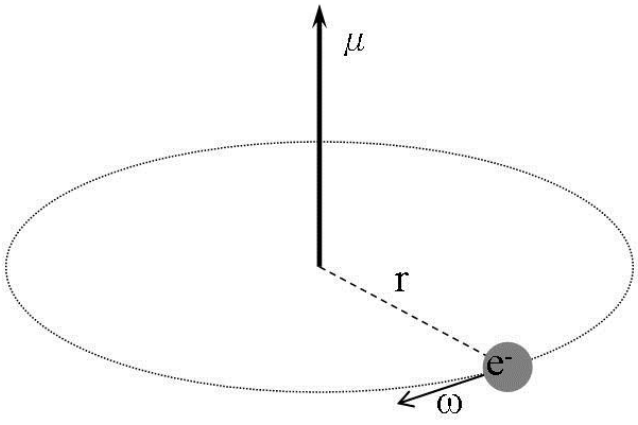

Figure 1.1 Magnetic moment produced from the electron movement

1.3 Magnetoresistance

Magnetoresistance (MR) refers to the change in electrical resistance of a material under the influence of an external magnetic field. It has a variety of physical origins, depending on the material's intrinsic and extrinsic properties. They include ordinary MR (OMR), anisotropic MR (AMR), tunneling MR (TMR), colossal MR (CMR), and giant MR (GMR). When talking about magnetoresistive materials, MR ratio is a universal parameter to be considered. Generally, the MR ratio is defined to be the ratio of the change in resistance when the field is applied to the resistance at zero field, that is

$$MR\ ratio\ = \frac{R_H - R_{H=0}}{R_{H=0}} \qquad \ldots (1.1)$$

Thus, a material which has a larger resistance in the presence of a field than in the absence of a field is defined to have a positive magnetoresistance, whereas if the field reduces the resistivity, the magnetroresistance is negative.

MR effect is important in technological applications as it is widely used in magnetic memories, read heads and magnetic field sensors. In the following, various MR effects will be introduced.

1.3.1 Ordinary magnetoresistance (OMR)

Consider a sample with an electric current flowing along the positive x-direction, as shown in Figure 1.2. Once there is a magnetic field applied in the positive z-direction, electrons are deflected (yellow arrow) from their original paths (red arrow) by the Lorentz force acting on them. The electrons travel with longer paths inside the sample in the presence of the magnetic field, and hence the sample resistance increases. The effect is coined as OMR.

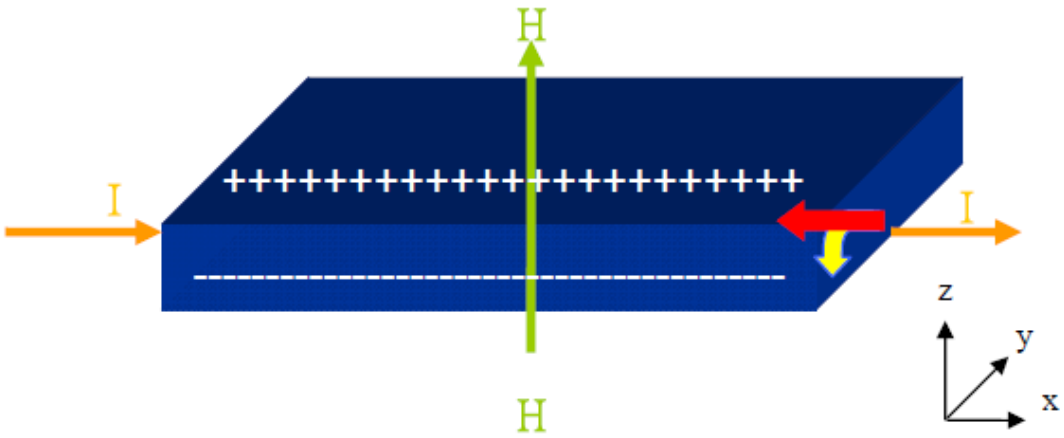

Figure 1.2 Schematic diagram showing OMR

1.3.2 Anisotropic magnetoresistance (AMR)

The physical origin of AMR arises from spin-orbit interactions, in which electron clouds around the nuclei deform as the magnetization changes in direction. This deformation changes the amount of electrons to be scattered, thus achieving a change in resistance. The phenomenon is called AMR because the change in resistance when a field is applied parallel to the current direction is different from that when the field is perpendicular

to the current direction. In fact, the resistance for current flowing parallel to the field direction increases when a field is applied, whereas the resistance for current flowing perpendicular to the field direction decreases by approximately the same amount. The effect is significant even in small fields, and the magnetoresistance saturates at 5-10 G.

1.3.3 Colossal magnetoresistance (CMR)

Colossal magnetoresistance (CMR) was first observed in 1994 by Jin et al [6] in the perovskite structure manganite, $La_{0.67}Ca_{0.33}MnO_3$. The term colossal was chosen because of the very large change in resistance, essentially from an insulating to a conducting state, on application of a magnetic field. Although the original experiments were at low temperature, similar effects have since been observed at or near room temperature. However, a large field of a few teslas is required to cause the change in resistance. Therefore, CMR materials are not considered likely to find direct practical application as magnetic sensors or read elements in recording heads currently.

1.3.4 Gaint magnetoresistance (GMR)

This effect was first observed in 1988 [1] in antiferromagnetically coupled metallic multilayers of Fe/Cr. Data from the original paper are shown in Figure 1.3. Typical magnetoresistance values are an order of magnitude larger than those seen in AMR materials.

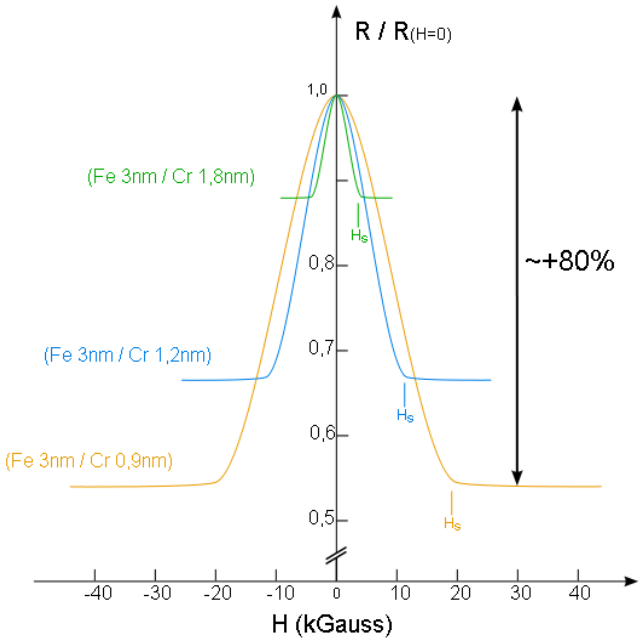

Figure 1.3 Magnetoresistance of three Fe/Cr superlattices at 4.2 K. The current and the applied field are along the same [110] axis in the plane of the layers [1]

In GMR materials, thin layers of magnetic material are separated by layers of non-magnetic material. Depending on the thickness of the non-magnetic layers, the magnetic layers couple either ferromagnetically or antiferromagnetically. GMR occurs when the thickness are chosen such that the adjacent layers are antiferromagnetic in zero applied field, as shown in Figure 1.4. This results in a high-resistance state as up-spin electrons are scattered by regions of down-spin magnetization and vice versa. Then the GMR effect works by changing the relative magnetization directions between adjacent magnetic layers. A low resistance state is obtained when a magnetic field strong enough to overcome the antiferromagnetic coupling is applied and the magnetization of the layers is rotated to a ferromagnetic configuration. When the

magnetic layers are ferromagnetically aligned, conduction electrons of compatible spin-type are able to move through the heterostructure with minimal scattering, and the overall resistance of the material is lowered.

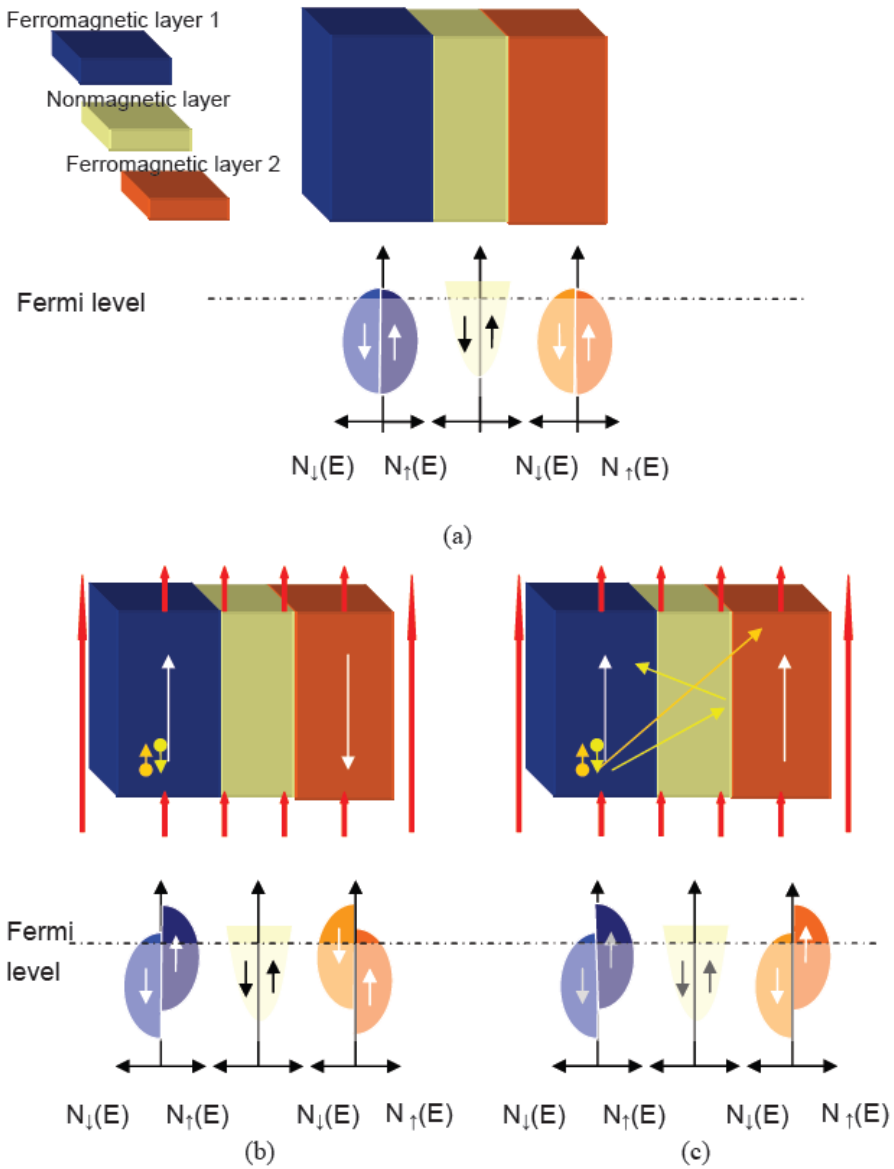

Figure 1.4 Schematic diagram of GMR and the corresponding density of states of different layers when (a) no field is applied (b), it is in the antiparallel state (high resistance state) and (c) it is in the parallel state (low resistance state)

1.4 Reference

1. M. N. Baibich , J. M. Broto, A. Fert, F. Nguyen Van Dau, F. Petroff, P. Eitenne, G. Creuzet, A. Friederich & J. Chazelas, "Giant Magnetoresistance of (001)Fe/(001)Cr Magnetic Superlattices," *Phys. Rev. Lett.*, vol. 61, no. 21, p. 2472–2475,1988
2. P. K. Muduli & R. C. Budhani, "Tailoring exchange bias in half-metallic $La_{2/3}Sr_{1/3}MnO_3$ thin films for spin valve applications," *Appl. Phys. Lett.*, vol. 94, p. 202510, 2009
3. B. T. Xie, Y. G. Zhao, C. M. Xiong, S. Park & W. Wu, "Current-voltage characteristics of phase separated $La_{0.5}Ca_{0.5}MnO_3$/Nb–$SrTiO_3$ p-n junction and magnetic tenability," *Appl. Phys. Lett.*, vol. 92 p. 232109, 2008
4. J. R. Christman, "Fundamentals of solid state physics," *John Wiley & Sons, Inc.*, p. 344, 1988
5. J. R. Christman, "Fundamentals of solid state physics," *John Wiley & Sons, Inc.*, p. 345, 1988
6. S. Jin, T. H. Tiefel, M. McCormack, R. A. Fastnacht, R. Ramesh & L. H. Chen, "Thousandfold Change in Resistivity in Magnetoresistive La-Ca-Mn-O Films," *Science*, vol. 264, p. 5157, 1994

Chapter 2
Experimental techniques

2.1 Basic principle of analysis techniques

2.1.1 XRD

X-ray diffraction (XRD) is an analytical technique based on at X-ray scattering from crystalline materials. It is a common and non-destructive method for characterization of crystal structure and for determination of atom location of various materials in bulk solid, powders, or thin films. Each material produces a unique X-ray "fingerprint" of X-ray intensity versus scattering angle that is characteristic of its crystalline atomic structure. Qualitative analysis is possible by comparing the XRD pattern of an unknown material to a library of known patterns.

A typical XRD system uses Cu K_α radiation (λ= 0.154 nm) and operates either in four-circle mode or Bragg-Brentano (θ-2θ) geometries. The Cu K_β radiation is normally filtered by a Nickel filter.

When the X-ray radiation from the X-ray source interacts with the atoms, it scattered in all directions. Most of the X-ray will destructively interfere with each other except in certain directions which constructive interference occurs as shown in Figure 2.1.

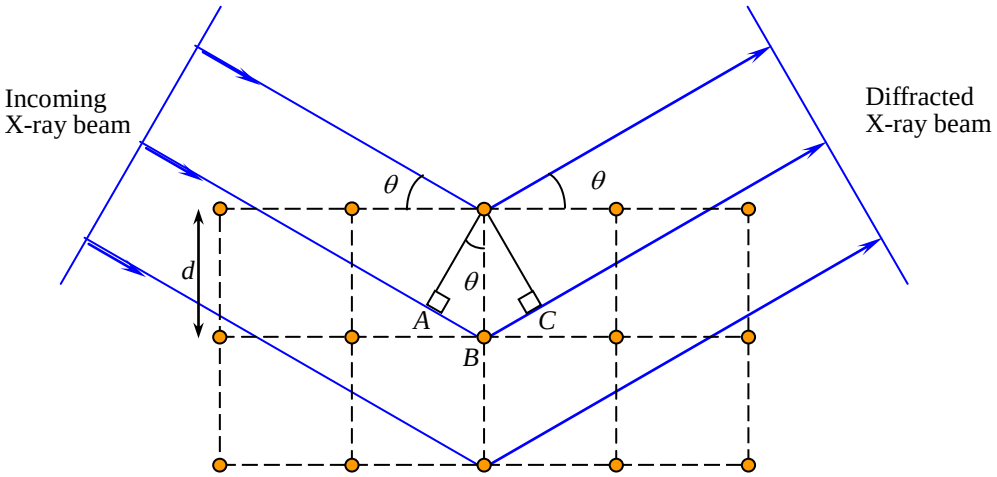

Figure 2.1 Bragg diffraction of X-rays from successive planes of atoms

The diffraction condition follows Bragg's Law:

$$2d\sin\theta = n\lambda,\ n = 1, 2, 3, \ldots \tag{2.1}$$

where n is the order of the intensity maximum, λ is the X-ray wavelength, d is the interplanar spacing, and θ is the incident angle of X-ray beam.

The interplanar spacing for a simple cubic structure can be determined by the following equation

$$d = \frac{a}{\sqrt{h^2 + k^2 + l^2}} \tag{2.2}$$

where a is the lattice constant of the crystal structure and h, k and l are the reciprocal lattice indices for a, b, c axis respectively.

The experimental geometry of X-ray diffractometer (XRD) is illustrated in Figure

2.2. It consists of the X-ray source, detector, monochromator and different kinds of slits. Also, there are four rotating axes of θ (ω), 2θ, χ and ϕ for different scan modes. All different scan modes, θ-2□, ω and ϕ scans, were utilized to investigate the crystal structure of the films in this project.

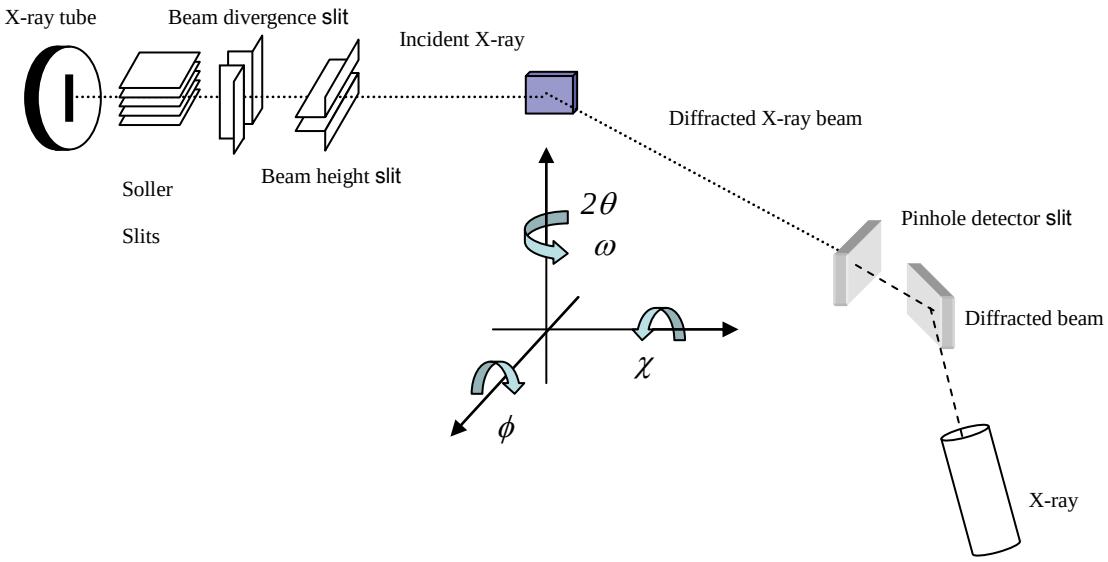

Figure 2.2 Experimental geometry of X-ray diffractometer

2.1.2 SEM

Scanning electron microscopy (SEM) is one of the most versatile and well proven micro-imaging techniques. It is not an optical instrument as it consists of no image forming lens but probe forming-Signal detecting device for electron optics. It is based on the interaction of high energy electrons beam with the specimen. It images the microstructures of a sample's surface by scanning a beam of high energy electrons across the sample's surface. Compared to conventional microscopy, an electron microscope offers many advantages including high magnification, large depth of focus, better resolution, and simplicity for sample preparation and observation.

In SEM, a focused high-energy electrons beam is scanned over the surface of the specimen. The electrons are accelerated over a voltage of a few 100 eV to 30 keV. The electron beam interacts with the material giving out a variety of signals. The interaction can either be elastic or inelastic collision between the electron beam and specimen. As shown in Figure 2.3, they include secondary electrons, backscattered electrons, characteristic x-ray etc., each of which may be used to characterize a material with respect to some specific properties. The detecting device in SEM mainly detects the reflected electrons from the surface of a specimen. These signals are collected by detectors to form images of the sample displayed on a cathode ray tube screen.

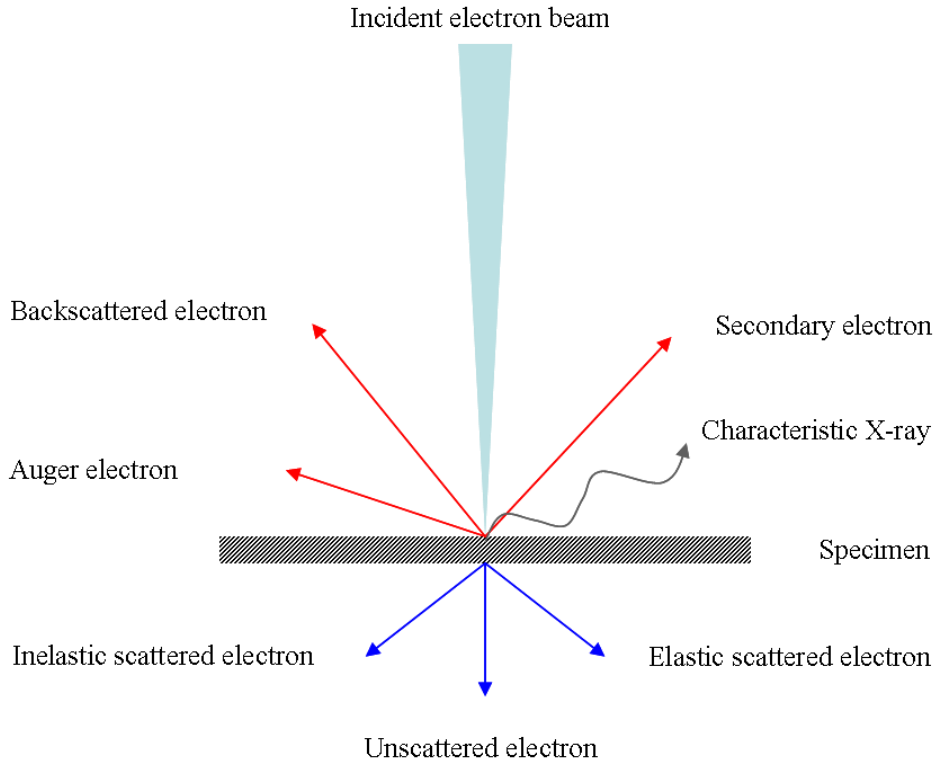

Figure 2.3 Schematic diagram of different electron interactions

The most commonly used imaging mode of the scanning electron microscope is the secondary electron emissive mode. Since those secondary electrons that are produced within a very short distance from the surface can escape from the sample. This means that this detection mode provides topographical images with high resolution, making this the most widely used for imaging surface topography, such as porosity, particle size distributions and surface roughness.

In this study, a JEOL JSM-6335F field emission scanning electron microscope was used to obtain the images of thin films. Normally, the energy range of the high energy electron beam is between a few hundreds eV to 40 keV. The base pressure of the chamber is around 5 x 10^{-3} Pa. The resolution of the SEM can be below 10 nm.

2.1.3 EDX

Energy dispersive X-ray (EDX) is a widely used tool for chemical analysis. An EDX system is commonly found on SEM equipped with an X-ray detector. The characteristic X-rays emitted from the sample serve as fingerprints and give elemental information of the samples including, quantitative analysis. The elemental composition of specimen in 1-D and 2-D can also be investigated by EDX.

Specimens for EDX require that the surfaces be ground and polished to an ultra smooth surface. The elemental distribution of targets used in this project is evaluated by using Energy Dispersive X-ray spectroscopy (EDS).

2.1.4 XPS

X-ray photoelectron spectroscopy (XPS, Phi 5600) was applied to analyze the depth profiles of the relative contents of carbon (C), titanium (Ti) and oxygen (O). Aluminium (Al) K_α radiation with a characteristic energy of $h\upsilon$ = 1487 eV was used as the the excitation source. When an Al K_α photon knocks out a core electron, the electron would escape from the atom and becomes a photoelectron, which kinetic energy (U_k) is determined by an electron energy analyzer, such that the binding energy of the electron (U_B) can be calculated according to the following equation:

$$h\upsilon = U_k + U_B \qquad (2.3)$$

The area of a characteristic peak in a XPS spectrum is known to be proportional to the atomic concentration of the corresponding kind of atoms (donated by the symbol "i"). Thus, its atomic concentration can be calculated according to the following equation:

$$C_i = \frac{A_i / S_i}{\sum_j A_j / S_j} \tag{2.4}$$

where symbol "j" is used to index any kinds of atoms in the film. A_i is the area under the corresponding peak after removing the Shirley background while S_i and S_j represent the sensitivity factors of the atoms indexed by "i" or "j" respectively. The sensitivity factors were determined by standard calibration procedure in the factory.

In order to obtain a depth profile from the film surface by using XPS, an Ar ion beam of 4 keV was used to etch the film material layer by layer. The etching rates of the film materials were based on that of silicon (Si), which were measured to be 4 nm min^{-1}. A charge neutralizer is activated during measurement to generate "soft" electrons to compensate the charge accumulated on the surface.

2.1.5 SPM

Scanning probe microscope (SPM) has a number of family members. For examples, scanning tunneling microscope (STM), atomic force microscope (AFM), magnetic force microscopy (MFM), lateral force microscopy (LFM), and etc. In this study, the surface morphology of the films was investigated with AFM operating in tapping mode.

AFM is a non-destructive and ultra-high resolution microscopic technique that can reveal the surface morphology and deduce the average roughness of a film surface. Instead of using a beam of electrons to image the sample, it uses a fine mechanical probe to scan over the surface of the sample.

Figure 2.4 shows the major components of an AFM. The image is produced by dragged a vibrating cantilever with Si_3N_4 tip across the surface. When the tip brought close to the sample, various inter-atomic force between the tip and the sample surface varies with their proximity, causing the cantilever to deflect to different extents. The direction of the laser reflected from the back of the cantilever is then deviated. The deflection of the laser beam is coherent with the undulation of the detected area and is recorded to form an image of the scanned surface.

The scanner is piezoelectric ceramic which provides the precise positioning control. Piezoelectric ceramic changes its geometry when a voltage is applied. The voltage applied is proportional to the resulting mechanical movement. The piezoelectric scanner is designed to bend, expand, and contract in a controlled, predictable manner. Therefore, it can provide a way of controlling the tip-sample distance and of moving the tip over the surface. The lateral resolution is around a few nanometers and that in the vertical direction is less than 1 Å.

Root mean square roughness (Z_{RMS}) is a parameter used to represent the roughness

of a film surface. This value is defined by equation (2.5), where z_i is the deviation from the mean position, and n is the number of date points collected over the detected area.

$$z_{rms} = \sqrt{\sum_i \frac{z_i^2}{n}} \tag{2.5}$$

The typical area observed in this study is about 3.0 x 3.0 μm. The vibration frequency of the tip was 0.5 Hz with scanning speed 2.97 μm s^{-1}.

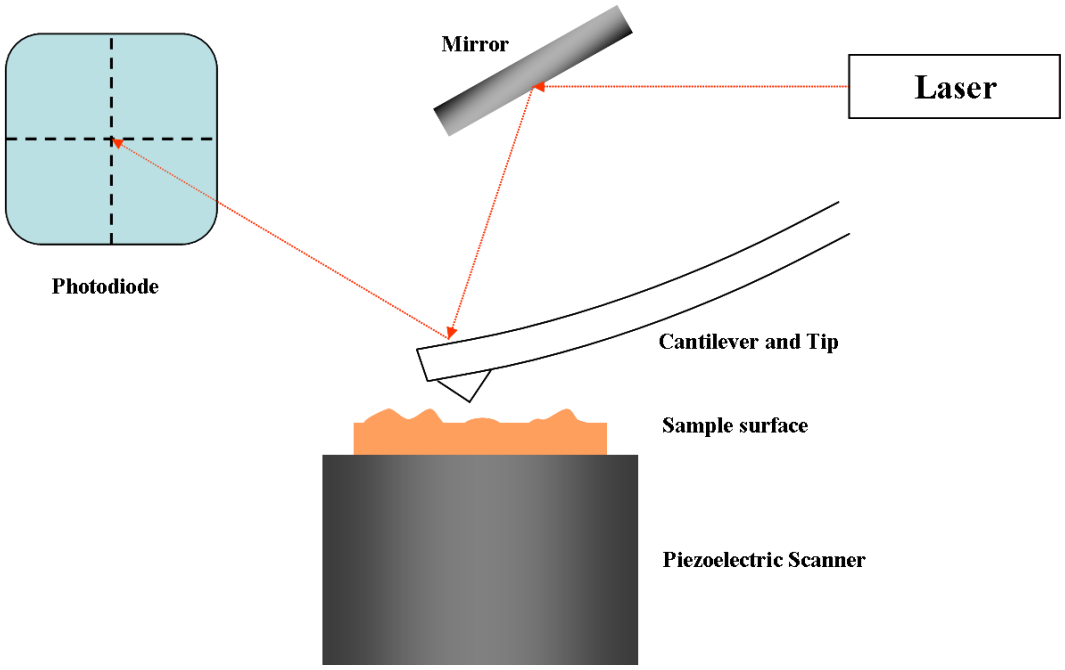

Figure 2.4 Schematic of the major components of AFM

2.1.6 Resistivity against temperature measurement

Four-point probe measurement is used in this project to determine the phase transition temperature of the ferromagnetic thin film. By using four point measurements, the issue of contact resistance was minimized. In electrical measurements, four parallel electrodes with 1 mm separations were deposited on a sample through a stainless steel

mask by pulsed laser deposition. Four aluminium wires are wire-bonded on the electrodes. The sample is then attached to the cold finger of the cryostat by using thermal grease for better thermal conduction.

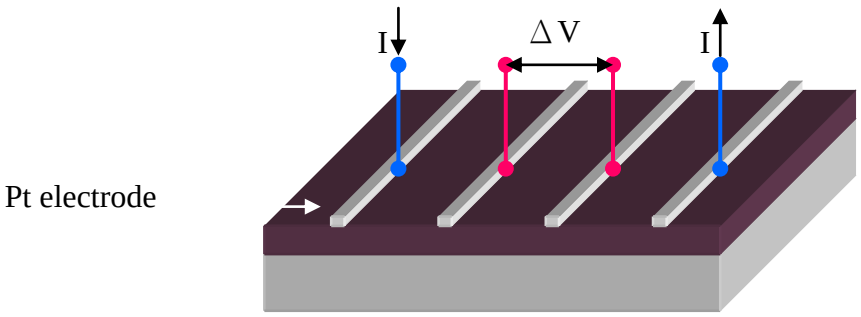

Figure 2.5 Configuration of resistivity against temperature measurement

Figure 2.5 shows the configuration for such measurements. The measured resistance R was used to calculate the resistivity ρ by using the equation 2.6,

$$\rho = \frac{RA}{l} \tag{2.6}$$

where l is the distance between the current contacts and A is the cross section area that the current flows through.

A Keithley 2400 sourcemeter was used for resistance measurements. It has two pairs of terminals for four point resistance measurements. A He closed-cycle cryostat was used to cool down the sample to a desired temperature. The sample is cooled by a cold finger directly through direct thermal conduction. A temperature controller was used to regulate the heater and measure the temperature of the cold finger, maintaining the cold finger at a desired temperature. The temperature range lies

between 20K and 400K. Both the temperature controller and the sourcemeter are computer-controlled by a LabView program. The data were recorded automatically throughout the whole measurement.

2.1.7 VSM

The vibrating sample magnetometer (VSM) measures the magnetic moment by moving the sample between two pick-up coils at frequency of 1 to 100Hz. If a sample of any material is placed in a uniform magnetic field, created between the poles of a electromagnet, a dipole moment will be induced. If the sample vibrates with sinusoidal motion, a sinusoidal electrical signal can be induced in suitable placed pick-up coils. The signal has the same frequency of vibration and its amplitude will be proportional to the magnetic moment, amplitude, and relative position with respect to the pick-up coils system.

The system used in this study is a Lakeshore 7407 system. It mainly includes a pair of 7-inch electromagnet with variable sample space, a vibrating stage, a set of special probes which carry the sample, a low temperature cryostat for low temperature measurement down to 77 K with continuous flow of liquid nitrogen and an oven for high temperature measurement up to 1273 K. The pick-up coils are built into the electromagnets. These have the advantage that the coils are independent of the sample temperature.

The standard temperature range for low temperature cryostat is from 77 K to 450 K with fields up to 1.2 Tesla. The sensitivity is up to 10^{-6} emu with a suitable averaging time at room temperature.

2.2 Experimental Details

2.2.1 Target Fabrication

A $La_{0.7}Sr_{0.3}MmO_2$ target was fabricated by the standard solid state reaction method. Table 2.1 shows the information of chemicals used and Table 2.2 summarizes the condition of fabrication involved in the whole process.

Powders of La_2O_3, $SrCO_3$ and MnO_2 were weighed according to the desired stoichiometric ratios and mixed with ethanol. The mixture was ball milled for 6 hours, and then calcinated at 1100 °C for 10 hours and then 1200 °C for 10 hours to complete the chemical reaction. The calcinated powder was grinded into fine powder and compressed to a 5-mm thick circular pellet of diameter 2.5 cm by an oil compressor, at a force of 5 Ton. Finally the pellet was sintered at 1320 °C for 10 hours.

	Required Chemicals		
	La^{3+}	**Sr^{2+}**	**Mn^{4+}**
Powder	La_2O_3	$SrCO_3$	MnO_2
Molar mass	325.81	147.83	86.94
Weight (g)	10.03	3.94	7.73

Table 2.1 The information of chemicals used for LSMO target fabrication

	Temperature	Duration
Ball milling (in ethanol)	Room Temp	8 hr
Calcinations	1100 ^{o}C	10 hr
	1200 ^{o}C	10 hr
Sintering	1320 ^{o}C	10 hr

Table 2.2 Conditions of fabrication of LSMO target

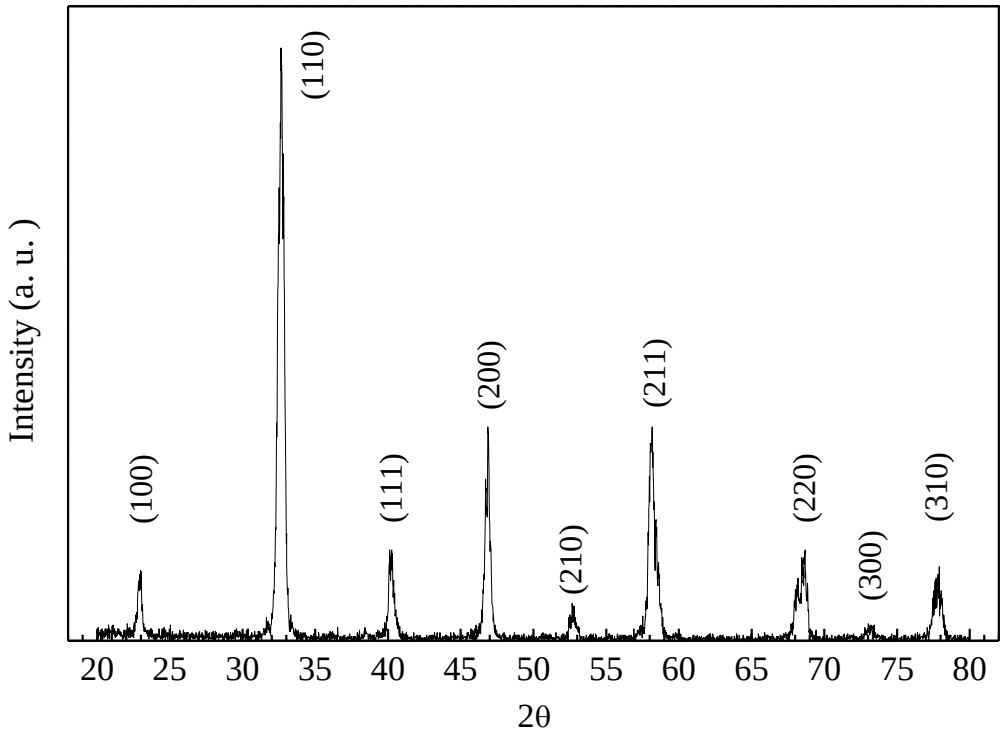

Figure 2.6 XRD pattern of LSMO target

The as-prepared LSMO target was structurally characterized by XRD. In the θ-2θ scan shown in Figure 2.6, all peaks can be matched to those listed in the International centre for Diffraction Data (ICDD) database. Also, its chemical composition was verified by EDX and the ratio of La: Sr was found to be 7:3.

2.2.2 Pulsed Laser Deposition System

In our PLD system, a KrF excimer laser (COMPex 200 manufactured by Lambda Physik) with wavelength 248 nm was used to generate laser pulses (~20 ns) with energy in the range of 150 – 300 mJ. The cross sectional area of the beam was 1 cm × 3 cm confined at the exit of the laser. The maximum pulse repetition rate was 20 Hz.

Figure 2.7 shows the configuration of the PLD system used in this project. The PLD deposition chamber comprised of several elements: stainless stain vacuum chamber, target manipulator, substrate holder, vacuum pump, gas supply and vacuum gauges. A rotary pump and a diffusion pump were connected to the chamber at the bottom via a butterfly valve. As the side wall of the vacuum chamber had eight ports, components like gas inlet, pressure gauge, target manipulator, substrates holder were mounted on the side of the wall. The rest of the ports were sealed with laser-quality optical lenses made of "UV-grade fused silica" with a transmittance over 90 % for the wavelength range of 185 to 2000 nm.

For target ablation, laser beam was focused by a convex lens to form a spot on the target so that desired laser energy density (~ 5 Jcm^{-2}) can be achieved. The focal length of the lens was 30 cm, matching the size of the chamber. A gas inlet port was used for the afflux of oxygen gas (99.7 % purity), which provided an oxygen environment for oxide thin film fabrication.

Before ablation, the chamber was pumped down to a base pressure of 5 mTorr by the rotary pump. Afterwards, oxygen was filled into the chamber to the desired film growth pressure.

A 4-cm diameter substrate holder was used to control the substrate temperature during the film deposition process. It provided a stable temperature up to 700 °C. Tungsten wire with ceramic shielding was enclosed in a cylindrical stainless steel case, which was used as the heating elements. A type-K thermocouple was used to register the temperature on the substrate holder, while the heating rate was controlled by a programmable regulator. The substrates were mounted on the substrate holder with silver paste compatible for high temperature uses. Due to the high thermal conductivity of silver paste, a uniform temperature distribution on the substrate could be achieved.

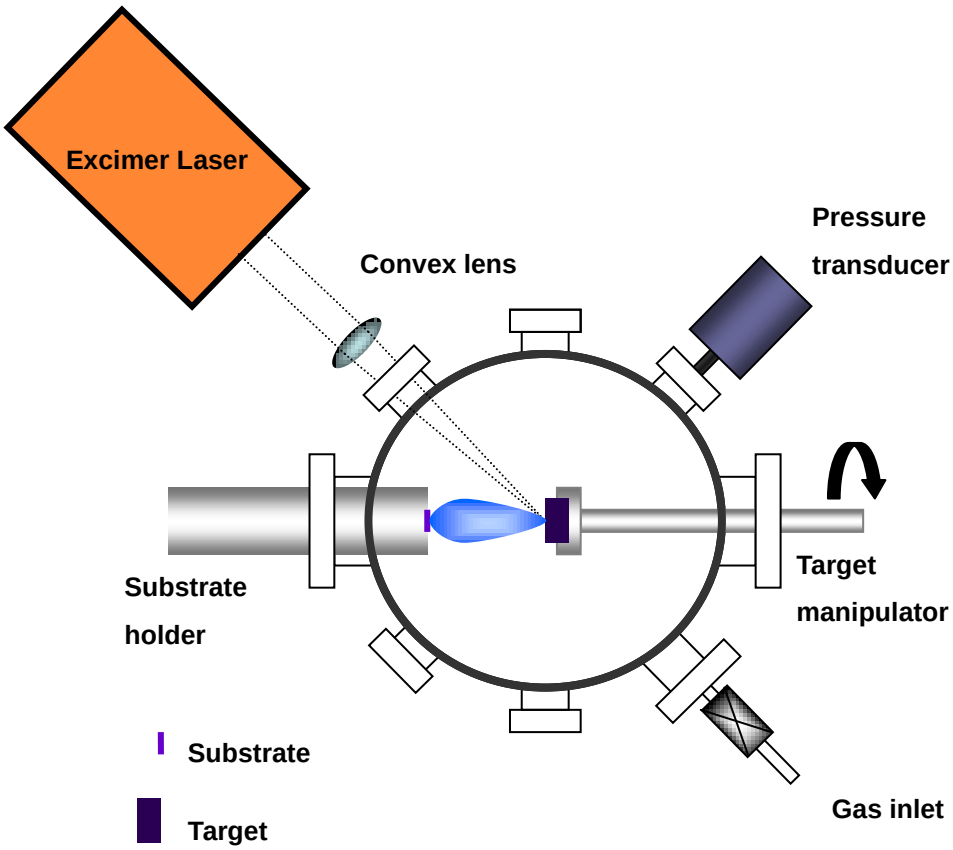

Figure 2.7 Pulsed Laser Deposition Setup

2.2.3 Choice of substrate: $LaAlO_3$

$LaAlO_3$ (LAO) is a very common material used as substrates for epitaxial growth of many transition metal oxides thin films due to the similarities in crystal structure and small mismatch between the lattice constants. Since the melting point of LAO is high, about 2450 K, interfacial reactions can be minimized under normal growth conditions. It is a typical perovskite structure that a simple cubic phase is favored at temperature above 708 K. However, at room temperature, it exhibits the rhombohedral perovskite structure with a slight distortion (a= b= c= 0.379 nm and angle of 90.066^o). This

structural transition results in strain, caused by the lattice distortion, which is relieved by twinning. Previous studies have shown that the phase transition in LAO leads to (100) and (110) twins. The (100) is more readily formed in comparison to (110). Although the crystal structure of $LaAlO_3$ is rhombohedral, it can be regarded as a perovskite having displaced O ions. In terms of a pseudocubic cell, the unit cell parameter is 0.379 nm.

2.2.4 Substrate Mounting and Cleaning

Samples were mounted on a substrate holder with a transferable platen constructed of stainless steel that incorporated chromel-alumel (K-type) thermocouple and tungsten filament at the bottom.

LAO substrates were cleaned in an ultrasonic cleanser by using spectroscopic grade acetone for 15 minutes. Then the sample was blow dry and mounted on the holder immediately. The sample was adhered by high temperature silver paste on the platen in order to provide a good thermo conductance between the sample and the platen.

Chapter 3
Epitaxially grown Manganese oxides

The manganese oxide with perovskite structure, known as manganites, is probably best known for exhibiting colossal magnetoresistance (CMR) [1]. Over the years, manganites with mixed-valences have been predicted to have 100% spin-polarization [2-4].

3.1 Introduction

Manganites crystallize in the perovskite structure ABO_3, which is represented in Figure 3.1 [5]. The perovskite structure is one of the common crystal structures found in complex oxide. It can be regarded as a closely packed cubic structure of large A-site cations at the corners, with a small B-site cation at the center surrounded by O^{2-} octahedra. Typically, A-site is an alkaline, alkaline-earth or rare-earth cation, while B-site is a transition metal cation [6]. However, most of the metallic ions can be accommodated into the perovskite structure. Under geometrical considerations, A-site cations must be large in order to be able to pack efficiently with large oxygen anions. On the contrary, B-site cations should be small enough to fit into the octahedral interstice. For stoichiometry, the total charge of A and B cations must be 6+ [7]. Thus, the types and the amount of element which can be fitted into the structure are limited under certain requirements.

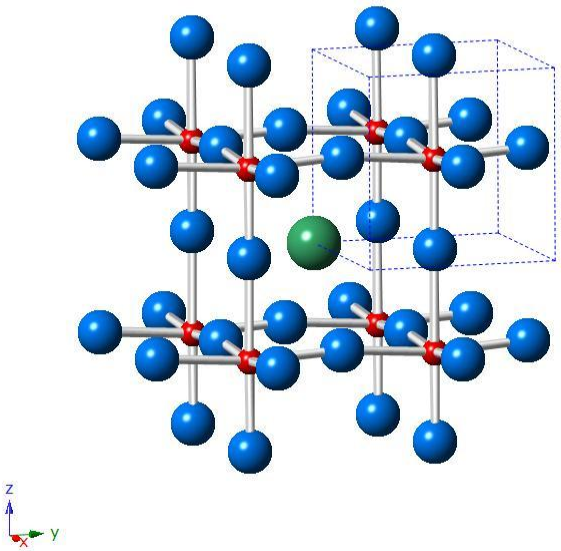

Figure 3.1 The ball and stick model of perovskite structure ABO_3 showing blue O^{2-} octahedral around B site (small red ball) while A site (large green ball) at the corner of cubic structure.

The physical properties of the doped manganites involve a complex interplay between the spin, charge, orbital and the lattice degrees of freedom, which strongly depended on the site of occupancy of the d orbital. In general, there are two fundamental concepts governing their behavior, namely tunability of kinetic energy and multiphase coexistence [8-11].

The tunability of kinetic energy is basically the conduction electron bandwidth of the oxides and competes with other interactions in the system that act to localize electrons. The major contributor on the conduction band is the electrons in the d orbital. They form an electrically inert ‘core spin’, while some of them can move from one transition metal site to another, with its spin parallel to the core spin on that site, subject

to the constraint imposed by Hund's coupling. The electron itinerancy from one site to another is strongly influenced by spin correlations. This is so-called 'double exchange' which implies the tunability of kinetic energy by altering the spin correlations. By varying the magnetic field and/or temperature, the spin correlations can be diversified.

The mixed-valent manganites exhibit the property of multiphase coexistence: the coexistence of two or more metallic, insulating, ferro-, ferri- and antiferromagnetic, charge- and orbitally-ordered phases, with typical domain sizes ranging from 10-100 nm [12-13] occurs because the state of the material can be easily perturbed and switched from kinetic-energy-dominated (i.e. metallic) to interaction-dominated (i.e. insulating, and charge/orbitally ordered) behavior by changing spin correlations. Indeed, the energy balance between different electronic/magnetic states of these materials is quite delicate. Multiphase coexistence is being increasingly looked upon as the primary cause of the high sensitivity of manganite properties to perturbations.

Mixed-valent manganites are interesting for scientists because their physical properties can be tailored by proper doping in A-site cations. For example, $La_{1-x}Sr_xMnO_3$ (LSMO) and $La_{1-x}Ca_xMnO_3$ (LCMO) are believed to exhibit the property of complete or nearly complete spin polarization owing to the double exchange process in them. The following section will give a detailed discussion on LSMO.

3.2 $La_{0.7}Sr_{0.3}MnO_3$

For LSMO, its parent compound $LaMnO_3$ is antiferromagnetic. Upon doping, the trivalent La cation is replaced with a divalent Sr cation. A mixed 3+/4+ valence in the Mn sites must be assumed so that electro-neutrality is conserved. Electrons which hop among or are localized on the Mn^{3+} and Mn^{4+} ions govern the physical properties of LSMO [14]. The presence of mixed 3+/4+ valences not only alter to magnetic property, but also the electrical property of LSMO. The magnetic properties of the perovskite manganite are interrelated with the electrical properties, which originate from electron transfer between Mn 3d orbit and O 2p orbit. In Figure 3.2, it shows the electronic phase diagram in the plane of temperature versus concentration of Sr ($0.0 \leq x \leq 0.6$) in LSMO [15].

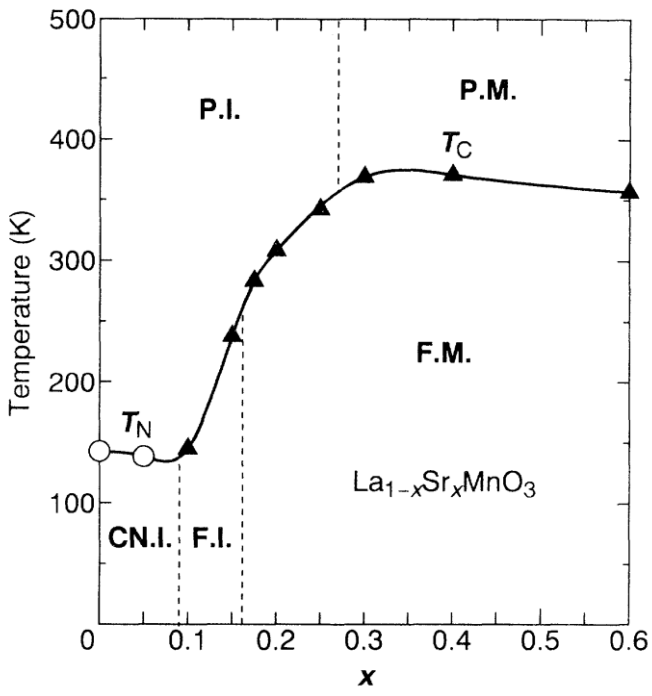

Remarks:

P.M. : paramagnetic metal

P.I. : paramagnetic insulator

F.M. : ferromagnetic metal

F.I. : ferromagnetic insulator

CN.I. : spin-canted antiferromagnetic insulator

T_N : Neel temperature

T_C : Curie termperature

Figure 3.2 Electronic phase diagram of perovskite $La_{1-x}Sr_xMnO_3$ [15]

In the ideal case, the perovskite is cubic and this structure provides a crystal field [5] to split the Mn 3d orbitals into 5-fold degeneracy as shown in Figure.3.3. The 3d orbital levels consist of higher energy e_g doublets and lower energy t_{2g} triplets. Referring to Figure 3.3 , the crystal field splitting $\Delta \sim$ 1.5 eV is lower than the exchange energy $J_H \sim 2$ eV [16] so that three electrons occupy the three $t_{2g} \uparrow$ levels, and the remaining electron lies on the first $e_g \uparrow$ level on a Mn^{3+} site. The introduction of Mn^{4+} thus represents a form of hole doping of the e_g sub-band.

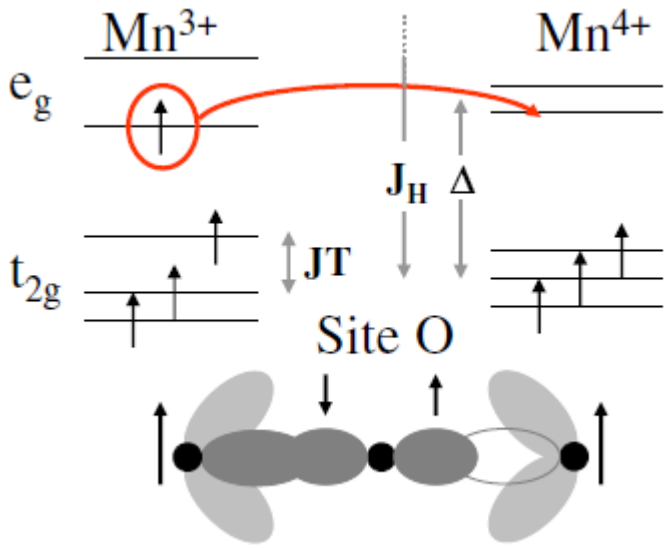

Figure 3.3 Schematic of the double exchange mechanism in $La_{2/3}Sr_{1/3}MnO_3$ between the σ orbitals of Mn^{3+} and Mn^{4+} sites across the oxygen 2p orbitals. For Mn^{3+}, the lifting of degeneracy between the two e_g levels, and between the top two t_{2g} levels, reflects the Jahn–Teller (JT) distortion of the oxygen octahedral around this site.

3.2.1 Double exchange mechanism

The double exchange mechanism, proposed by Zener [17], takes place between Mn mixed-valence sites across O and contributes to the effective delocalization of $e_g \uparrow$ electron among all Mn sites. These exchange interaction requires that the initial state

(Mn^{3+}-O-Mn^{4+}) and final state (Mn^{4+}-O-Mn^{3+}) be degenerated in energy, leading to a delocalization of the hole on the Mn^{4+} site or electron on the Mn^{3+} site. This process is a real charge transfer process that an electron is transferred from Mn^{3+} to O^{2-} and from O^{2-} to Mn^{4+} with an overlap integral between Mn 3d and O 2p orbitals.

Meanwhile, the transfer of electrons occurs only when the core spins of the Mn ions are aligned ferromagnetically due to strong Hund's rule coupling. This implies an identical spin referential on each Mn site, which is pinned by the three localized t_{2g} electrons in Mn 3d orbital. This spin-conserving process of electron transfer thus ensures long-range ferromagnetism, and the conduction of e_g electrons with spin ↑.

3.2.2 Half-metal nature

Half metals are ferromagnets whose density of states shows only one occupied spin-polarized sub-band at the Fermi level, i.e. all the electrons at the Fermi level in the half metal are either spin up or spin down. Spin polarization (*P*) is a physical quantity to determine a material having half-metallic property or not. It is a degree of spin aligned in certain direction at the Fermi level. It can be calculated as follow:

$$P = \frac{[N_{\uparrow}(E_F) - N_{\downarrow}(E_F)]}{[N_{\uparrow}(E_F) + N_{\downarrow}(E_F)]}$$

Non-magnetic materials, such as silver (Ag) or Zinc (Zn) have no net spin polarization, i.e. P = 0 since their density of states of up-spin and down-spin electrons are equal. For magnetic elements like iron (Fe) or nickel (Ni), as they have imbalance of

up-spin and down-spin, P is known to be around 50%. For those materials produce 100% spin polarization, they are defined as half metal. This characteristic has major implications for the efficiency of spintronic devices and increases their potential magnetoresistance by a huge factor.

A few compounds have been predicted to be half metallic. They are chromium dioxide (CrO_2) , iron oxide (Fe_3O_4), chromium arsenide (CrAs), mixed-valence manganites, and Heuslers alloy such as NiMnSb and Co_2MnSi [18]. In the particular case of manganites such as LSMO and LCMO, there are a lot of controversies regarding their half metallic property. However, the half-metallic property of them is of great importance for applications in spintronic. For example, a tunnel magnetroresistance junction (MRJ) of LSMO/STO/LSMO heterostructures with magnetoresistance (MR) in excess of 1800% at 4 K has been demonstrated [19]. Indeed, these oxides have a potential on enhancing the performance of spintronic device such as spin valve.

3.3 Experiment

$La_{0.7}Sr_{0.3}MnO_3$ thin films were grown on single crystal LAO (100) substrates at a substrate temperature of 650 °C by using pulsed laser deposition. The distance between the target and the substrate was 4 cm. The base pressure of the deposition chamber was 5 mTorr. Since thin films produced by PLD were always oxygen deficient, there was a constant oxygen flow to maintain oxygen pressure at 150 mTorr during the deposition.

After the deposition, films were annealing at 650 °C for 15 min. Figure 3.1 summarizes conditions of the fabrication of LSMO thin films.

LSMO has a pseudo-cubic structure with the a-axis lattice parameter equals to 0.388 nm. It is expected that epitaxial LSMO thin film can be grown on LAO substrate with a lattice mismatch of only 2.3 %.

Pulsed Laser Deposition		
Substrate		LAO (100)
Target-to-substrate distance (cm)		4
Temperature (°C)		650
Laser	**Energy (mJ)**	220
	Frequency (Hz)	5
Oxygen pressure (mTorr)		150
Deposit time (min)		10
In-situ annealing time (min)		15

Table 3.1 Parameters of LSMO fabrication using pulsed laser deposition.

3.4 Results

3.3.1 Structural characterization

The θ-2θ scan of LSMO thin film grown on LAO (100) single crystal substrate is shown in Figure 3.4. Only the (h00) peaks are observed, indicating the growth of single phase LSMO thin film on LAO. The in-plane structural quality and grain orientation can be determined by a 360° φ-scan. In Figure 3.5, 360°φ-scans of (202) LSMO and (202) LAO are displayed. Figure 3.6 shows the rocking curve of the thin film in (200) orientation. The full width half maximum was found to be 0.48°.

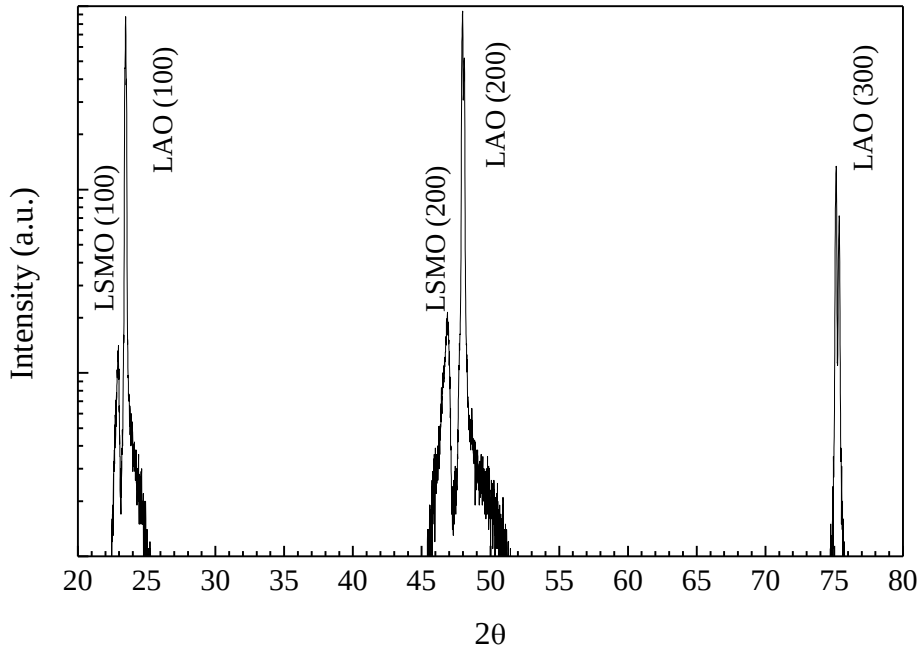

Figure 3.4 X-Ray θ-2θ diffraction pattern of LSMO/LAO structure.

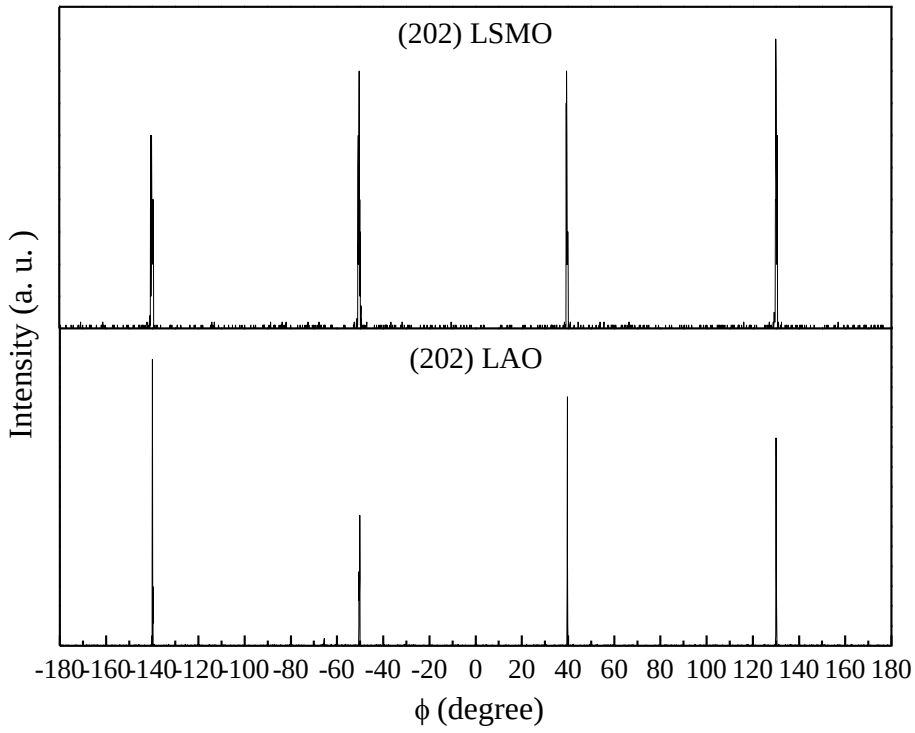

Figure 3.5 360° ϕ-scans of LSMO thin film on LAO

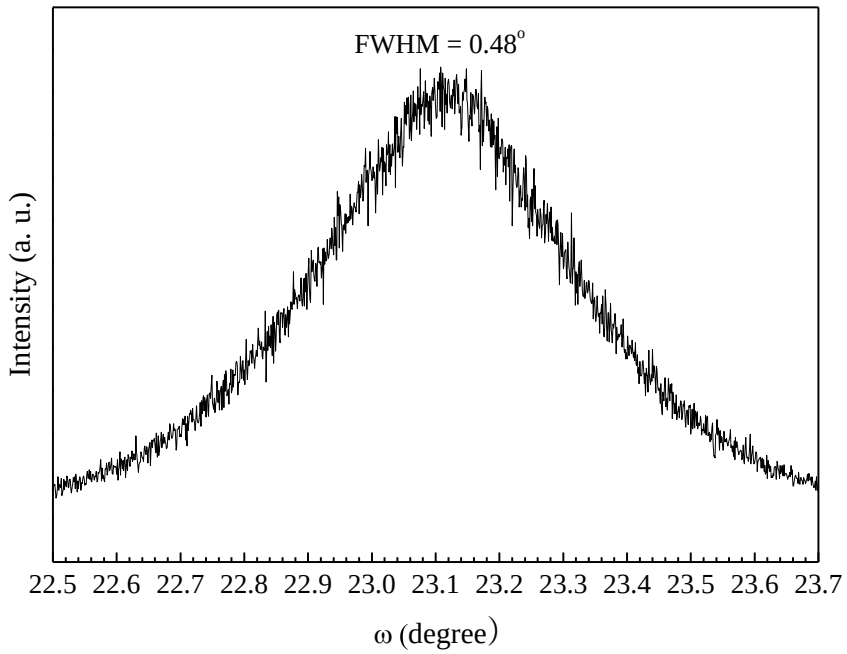

Figure 3.6 The rocking curve of LSMO thin film

3.3.2 Surface morphology

The surface roughness was investigated by using AFM. Figure 3.7 shows the AFM image of a LSMO thin film over an area 1 x 1 μm^2. The root mean square surface roughness of the film was found to be 1.4 nm. The grain size was found to be 200 to 250 nm.

3.3.3 Electrical Characterization

RT measurement was conducted after the structural and surface characterization. Figure 3.8 shows the RT curve of LSMO thin film from 70 K to 400 K. The ferromagnetic transition temperature of LSMO thin film was found to be 310 K. It showed metallic-like electrical conduction below 310 K. The maximum resistivity at 310 K was 5.05 x 10^{-6} ohm-cm

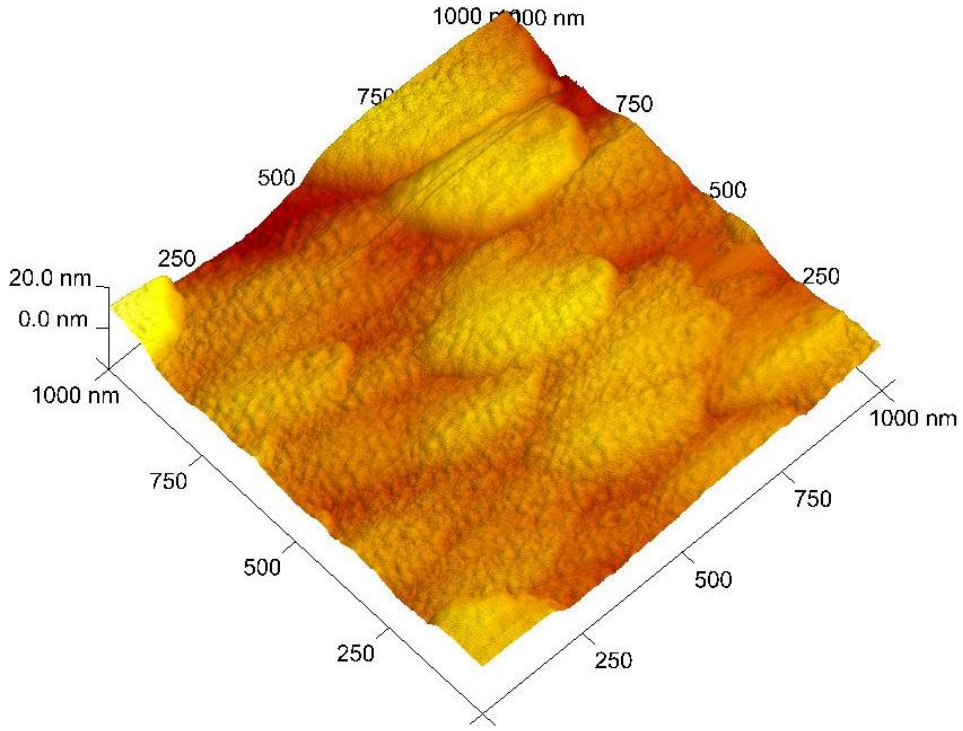

Figure 3.7 AFM image of LSMO thin film

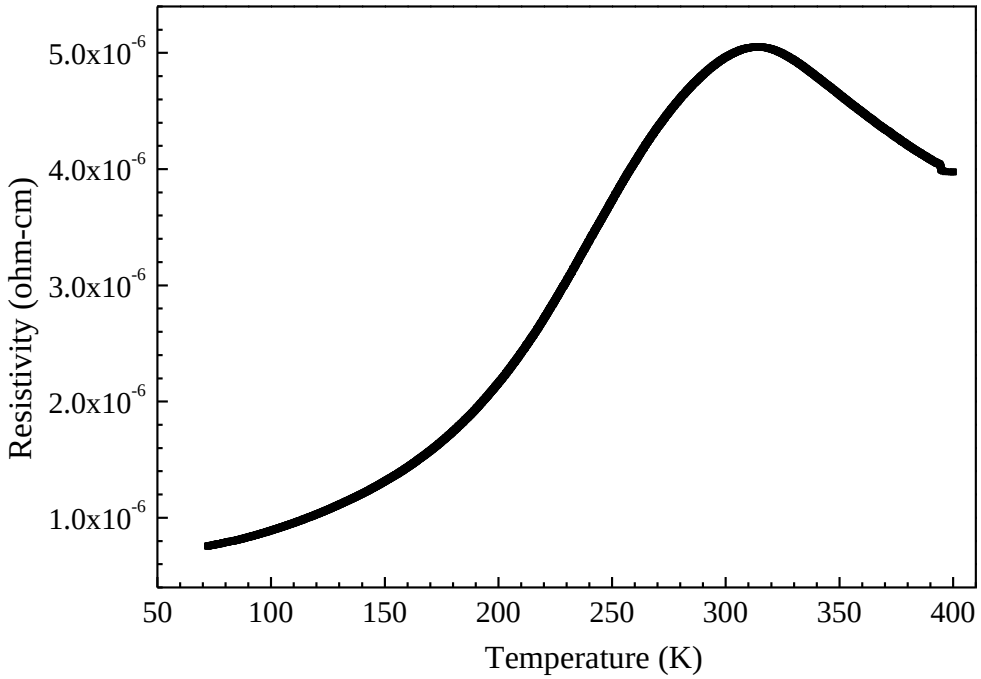

Figure 3.8 Temperature dependence of resistivity of LSMO thin film.

3.3.4 Magnetic properties and magnetoresistance

The magnetization and magnetic hysteresis loops of the LSMO film has been measured using a VSM. Figure 3.9 displays the field-dependent magnetization (MH) measurement of a LSMO thin film (thickness 100 nm) at 100 K, 200 K and 300 K, when the magnetic field was applied in the in-plane direction. At 300 K, the saturation magnetic magnetic moment was about 200 memu while the coercive field of the film was about 200 G at 300 K.

Magnetotransport measurements have been carried out using a standard four-probe dc method. A uniform magnetic field (up to 2000 G) for these measurements was applied in the plane of the sample, and aligned either parallel or perpendicular to the current flow direction.

The LSMO thin film exhibited negative magnetoresistance as shown in Figure 3.10. The variations in the MR as a function of field for the LSMO film at 18 K are shown in Figure 3.10. The MR data are displayed as ratio $\Delta R/ R \times 100\ \% = [R(H) - R(H_c)/ R(H_c)] \times 100\ \%$, where R ($H_c$) is value of the peak resistance which occurs at the coercive field, as described later.

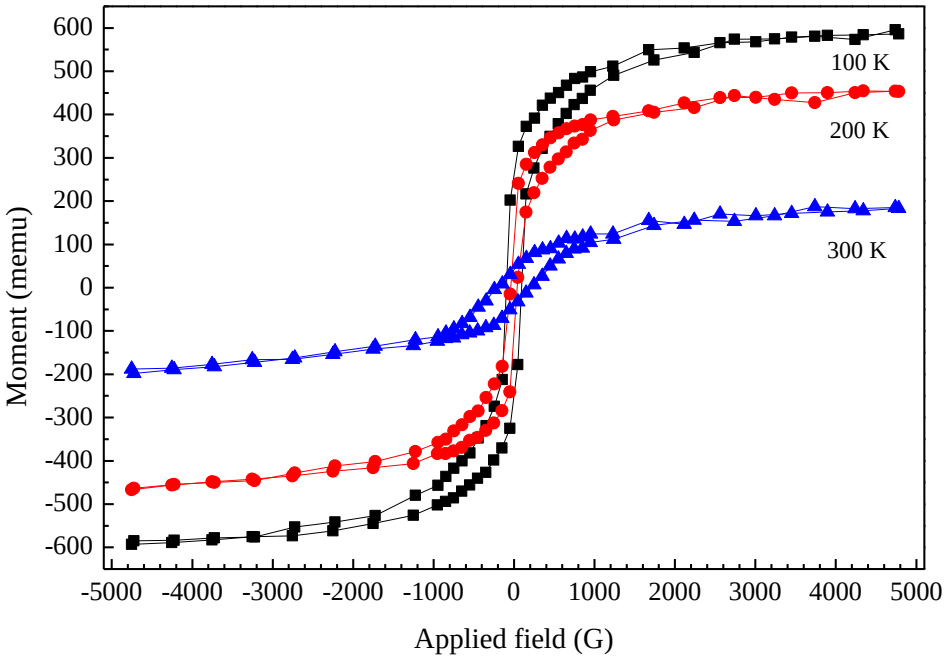

Figure 3.9 Temperature dependent M-H plot of LSMO layer

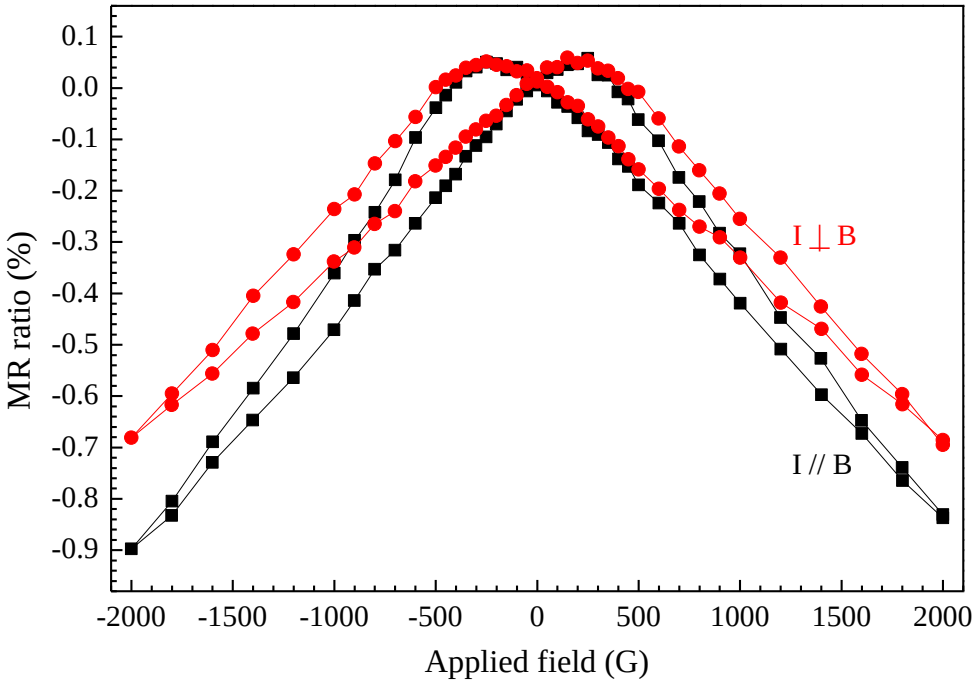

Figure 3.10 Magnetresistance measurement of LSMO layer at 18 K

3.5 Discussions

A single phase LSMO thin film was epitaxially grown on a LAO (100) substrate. The lattice constant of LSMO was found to be 3.88 Å. From the rocking curve, the FWHM is about 0.5°, which reflects the alignment of grains is not good enough in epitaxial growth. Since the maximum growth temperature in our system is 700 ℃, our films were *in-situ* annealed at 650 ℃, which is considered to be too low for post-annealing of LSMO. In fact, the quality of films can be improved by *ex-situ* annealing at 900 ℃ in a furnace.

As LSMO is a pseudo-cubic structure, both out-of-plane and in-plane epitaxial relationships can be verified by identifying the four-folded symmetric feature of the (202) planes of the (200) cut substrate. The φ-scan was performed to locate the diffraction peaks of (202) planes of both film and substrate. If both peaks from the film and substrate are aligned at the same φ angles with 90° separation, cube-on-cube epitaxial film can be confirmed. The diffraction angle of (202) LSMO and (202) LAO characteristics peaks shown in Figure 3.5 are completely matched. It suggests that the LSMO thin film grown on LAO is a cube-on-cube heteroepitaxy.

Apart from epitaxy, the surface roughness of the LSMO thin films was also studied at room temperature. It is important to obtain low surface roughness for the realization of Co doped TiO_2/LSMO heterostructure with smooth interface. For the LSMO thin

film grown on LAO substrate, the rms roughness of 1.4 nm was found, with a peak to peak value of 9.6 nm in an area of 1 x 1 μm^2. This low surface roughness allowed the formation of a good interface in the heterostructure study later on.

From the RT measurement, the metallic-semiconducting transition occurred at around 310 K. The films exhibit a metallic behavior at the temperature below 310 K, implying the existence of a ferromagnetic behavior in room temperature. The resistivity at 310 K was about 5.05 x 10^{-6} ohm-cm. In fact, the resistivity of the film can be significantly increased by enhanced disorder scattering at the grain boundaries. It implies that better the crystallinity of the film gives higher electrical conductivity.

In Figure 3.10, a modest change in resistivity (MR = 0.75% at 2000 Oe), with a rather sharp drop from the peak value followed by a more gradual decrease, is observed with the current flowing perpendicular to the applied field. In contrast, the film exhibits a much larger drop in resistivity for the same applied field (MR = 1 %) when the current is flowing parallel to the applied field.

This kind of dependence of MR behavior to the relative orientation between applied current and field arises from the intergranular tunneling MR as reported by Hwang *et al.* [4] That means the film did not demonstrate AMR. It has been reported that such intergranular tunneling magnetoresistance can be as small as 0.25% in highly epitaxial film and as large as 15% in polycrystalline films [20]. The magnitude of MR was about 1 % at 2000 G,

which is comparable with reported value in the literature. It also indicates the MR peaks at 200 G, which match well with the coercivity of the film as obtained from MH measurement.

In this work, both structural and magnetotransport properties measurements reflect that the PLD grown LSMO thin films are of high quality and they are fit for device fabrication.

3.6 References

1. P.K. Siwach, H.K. Singh & O.N. Srivastava, "Low field magnetotransport in manganites," *J. Physics: Condensed Matter*, vol. 20, p. 273201, 2008.
2. J.H. Park, E. Vescovo & H.J. Kim, "Direct evidence for a half-metallic ferromagnet," *Nature*, vol. 392, p. 794, Apr. 1998.
3. Y. Okimoto, T. Katsufuji, T.Ishikawa, A. Urushibara, T. Arima & Y. Tokura, "Anomalous Variation of Optical Spectra with Spin Polarization in Double-Exchange Ferromagnet: $La_{1-x}Sr_xMnO_3$," *Phys. Rev. Lett.*, vol. 75, no. 1, p. 109, 1995.
4. H.Y. Hwang, S.-W. Cheong, N.P. Ong & B. Batlogg, "Spin-Polarized Intergrain Tunneling in $La_{2y}3Sr1y3MnO3$," *Phys. Rev. Lett.*, vol. 77, no. 10, p. 2041, 1996.
5. M. Bowen, J-L. Maurice, A. Barthelemy, M. Bibes, D. Imhoff, V. Bellini, R. Bertacco, D. Wortmann, P. Sensor, E. Jacquet, A. Vaures, J. Humbert, J.-P. Contour, C. Colliex, S. Blugel & P. H. Dederichs, "Using half-metallic manganite interfaces to reveal insights into spintronics," *J. Physics: Condensed Matter*, vol. 19, p. 315208, 2007.
6. E.L. Nageav, "Colossal Magnetoresistance and Phase Separation in Magnetic Semiconductors," *Imperial College Press*, p. 298, 2002.
7. G. Venkataiah, V. Prasad & P.V. Reddy, "Influence of A-site cation mismatch on structural, magnetic and electrical properties of lanthanum manganites," *J. Alloys Compounds*, vol. 429, p. 1, 2007.
8. A.P. Ramirez, "Colossal magnetoresistance," *J. Physics: Condensed Matter*, vol. 9, p. 8171, 1997.
9. T. Hotta, A.L. Malvezzi & E. Dagotto, "Charge-orbital ordering and phase separation in the two-orbital model for manganites: Roles of Jahn-Teller phononic and Coulombic interactions," *Phys Rev. B*, vol. 62, no. 14, p. 9432, 2000.
10. Y. Tokura & Y. Tomioka, "Colossal magnetoresistive manganites," *J. Magnetism Magnetic Materials*, vol. 200, pp. 1–23, 1999.
11. M.B. Salamon & M. Jaime, "The physics of manganites: Structure and transport," *Reviews of Mordern Physics*, vol. 73, p. 583, 2001.
12. T. Wu, S.B. Ogale, J.E. Garrison, B. Nagaraj, Amlan Biswas, Z. Chen, R. L. Greene, R. Ramesh, & T. Venkatesan, "Electroresistance and Electronic Phase Separation in Mixed-Valent Manganites," *Phys. Rev. Lett.*, vol. 86, no. 26, p. 5998, 2001
13. M. Uehara, S. Mori, C.H. Chen & S. -W. Cheong, "Percolative phase separation underlies colossal magnetoresistance in mixed-valent manganites," *Nature*, vol. 399, p. 560, 1999.
14. T. A. Kaplan, S. D. Mahanti, "Physics of Manganites," *Kluwer Academic/Plenum*

Publishers - New York, p.71, 1998

15. A. Urushibara, Y. Moritomo, T. Arima, A. Asamitsu, G. Kido & Y. Tokura, "Insulator-metal transition and giant magnetoresistance in $La_{1-x}Sr_xMnO_3$," *Phys. Rev. B*, vol. 51, no. 20, p. 14103, 1995.
16. J.M.D. Coey, M. Viret & S.Von Molnar, "Mixed-valence manganites," *Advances in Physics*, vol. 48, no. 2, p. 167, 1999.
17. C. Zener, "Interaction between the d-Shells in the Transition Metals. II. Ferromagnetic compounds of Manganese with perovskite structure," *Phys. Rev.*, vol. 82, no.3, p. 403, 1951.
18. C.M. Fang, G.A. de Wijs & R.A. de Groot, "Spin-polarization in half-metals," *J. Applied Physics*, vol. 91, no. 10, p. 8340, 2002.
19. M. Bowen, M. Bibes, A. Barthelemy, J. P. Contour, A. Anane, Y. Lemsitre & A. Fert, "Nearly total spin polarization in La2/3Sr1/3MnO3 from tunneling experiments," *Appl. Phys. Lett.*, vol. 82, no. 2, p. 233, 2003
20. X.W. Li, A. Gupta, G. Xiao & G. Q. Gong, "Low-field magnetoresistive properties of polycrystalline and epitaxial perovskite manganite films," *Appl. Phys. Lett.*, vol. 71, no. 8, p. 1124, 1997.

Chapter 4
Anatase TiO_2 and its diluted magnetic oxide systems

Titanium dioxide has three common crystal phases: rutile, anatase and brookite. Although all three phases are stable at room temperature, rutile is usually found while brookite rarely exists due to the relative stability: rutile > anatase > brookite. Anatase undergoes an irreversible phase transition to rutile at temperature above 850 K [1]. However, this transition temperature strongly depends on a variety of factors such as impurities and crystal size [2].

4.1 Introduction

There is significant interest in the synthesis of phase-pure anatase thin films, both for applications and fundamental studies. In catalysis, photocatalysis, and dye-sensitized solar cells, anatase has proven advantageous over the rutile phase [3-5]. Electronic properties, surface structure, and morphology are key elements that must be controlled in these applications.

Both anatase and rutile possess tetragonal symmetry with different lattice parameters while brookite has an orthorhombic structure. Table 4.1 shows the structure of these three phases with their lattice constants [6].

Phase	Structure	Lattice constant	
Anatase	Tetragonal	a = 3.78 Å b = 3.78 Å c = 9.51 Å	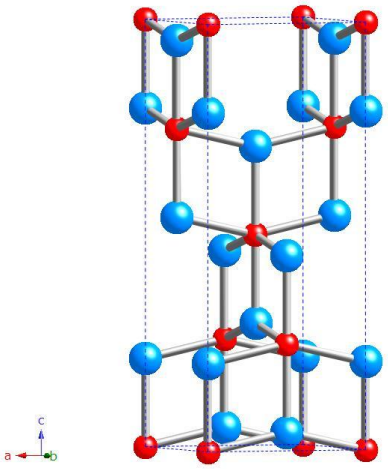
Rutile	Tetragonal	a = 4.59 Å b = 4.59 Å c = 2.96 Å	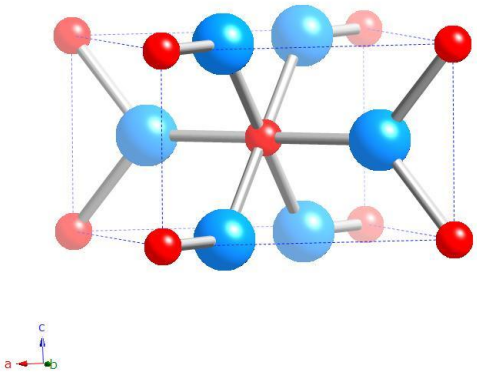
Brookite	Orthorhombic	a = 9.18 Å b = 5.45 Å c = 5.15 Å	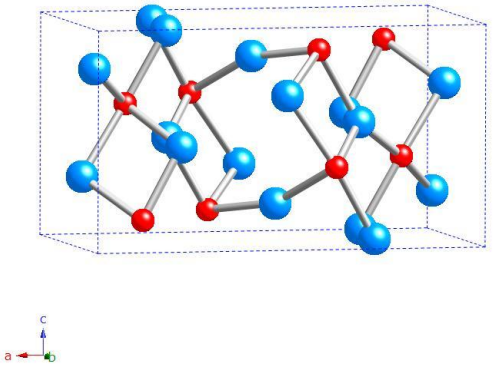

Table 4.1 Unit cells of titanium dioxide in three phases. For the ball-and-stick model, the small red balls and large blue balls are Ti^{4+} ions and O^{2-} ions respectively.

In anatase, each Ti atom is surrounded by a distorted octahedron of O atoms with axial and equatorial bond lengths of 0.198 and 0.195 nm, respectively. In rutile, compared to anatase, the octahedral coordination shell is less distorted, even though the bond lengths are the same as those in anatase. Moreover, there is a significant degree of buckling associated with O-Ti-O bonds in anatase when compared with rutile. This buckling reduces the crystal symmetry and results in a layer unit cell dimension in the [001] direction.

Numerous efforts have been focused on finding ways to produce crystallized and phase pure anatase films. As a low-temperature polymorph, anatase thin films are typically realized via deposition at low temperature where crystallinity is not optimal. In most cases, polycrystalline TiO_2 films possess either a mixture of rutile and anatase, or solely rutile. In general, epitaxial stabilization offers a means by which anatase thin films can be obtained on lattice-matched substrates, often for processing conditions where the phase is thermodynamically unstable in bulk. There are some reports on epitaxial anatase thin films deposited on $SrTiO_3$ (001) substrate by metal-organic chemical vapor deposition (MOCVD), or molecular-beam epitaxy (MBE) [7-9]. The considerable lattice mismatch between $SrTiO_3$ and anatase (lattice mismatch: -3.1%), however, makes it difficult to obtain high-quality epitaxial films. Therefore, another substrate to be considered is LAO (001), with smaller lattice mismatch

$[(a_{anatase}-a_{LaAlO3})/a_{LaAlO3}] = -0.26\%$.

Since LSMO thin films are grown on LAO, it is also used as substrate for the investigation of epitaxy growth of anatase TiO_2 single layer by using PLD method in our project.

4.1.1 Cobalt doped titanium dioxide

The first report of room temperature ferromagnetism in Co doped anatase TiO_2 thin films by Matsumoto et al [10] has aroused hectic research activities in many laboratories around the world to confirm this significant claim. While some groups support that this is a uniform DMS system (with evident suggesting oxygen plasma assisted molecular beam epitaxy OPA-MBE gives better results than laser deposition)[11], many take the view that it is the result of cobalt clustering [12-14], either in the form of cobalt metal clusters or clusters of Co-Ti-O complex. These clusters are suggested to be the cause of the observed ferromagnetism. Since the processing conditions can cause significant changes in the properties of this system, disorder or defects states might play an important role in this context. T. Venketesan et al. has reported that the clusters were seen to dissolve with a relaxation of lattice parameter under a specific processing condition of high temperature annealing (suggesting matrix incorporation of cobalt and RBS ion channeling for cobalt) [13]. They have also used high temperature growth instead of high temperature annealing in

order to obtain samples with no apparent clusters [15].

Interestingly such high temperature grown or annealed samples are fairly insulating thereby ruling out the possibility of RKKY type ferromagnetism initially suggested for the rather conducting or semiconducting anatase TiO_2 films grown at relatively lower temperatures. Other mechanisms such as the polaronic mechanism [15-16] appear more likely in such a case.

Phase relations in the system CoO-TiO_2 (Figure 4.1) [17] in the temperature range from 1130 to 1569 °C is determined by the quenching technique. Three crystalline phases (Co_2TiO_4, $CoTiO_3$, and $CoTi_2O_5$) are stable in equilibrium. The phase $CoTi_2O_5$ is less stable than the phase assemblage $CoTiO_3$ + TiO_2 when the temperature is below 1140 °C. During the growth of Co-doped TiO_2 thin film, we can not exclude the formation of $CoTi_2O_5$, which is unstable below 1140 °C in bulk Co-Ti-O phase diagram, because of the quasi-equilibrium nature of sputtering.

Ferromagnetism was observed at room temperature in Co-doped semiconducting anatase thin films [10]. To achieve ferromagnetic properties, as in other DMS materials, the Co ions must be magnetically aligned by some means. The mechanism of magnetic coupling can be determined by finding out the formal charge of the Co ions and the majority carrier type in the material. Chamber et al. [11] reported that the oxidation state of Co in the lattice is +2. They also revealed that the local structural environment for Co

in anatase is very similar to that of Co in $CoTiO_3$. In the structural similarities between the cation site in anatase and the Co site in $CoTiO_3$, this result corroborates the XRD-based conclusion that Co substitutes for Ti in the anatase lattice. The presence of substitutional Co at cation sites in the TiO_2 lattice requires an equal number of oxygen vacancies to maintain overall electrical neutrality. It can be understood by recognizing the substitution of Co^{2+} for Ti^{4+} being equivalent to reducing the formal charge of a cation from +4 to +2. In doing so, the removal of one O^{2-} for each Co is required to achieve charge balance. The resulting oxygen vacancies are expected to be electrically neutral.

It is also reported that the nonmagnetic $Co_xTi_{1-x}O_2$ films are found to be insulating. Pure, bulk TiO_2 is n-type by virtue of charged oxygen vacancies, which create shallow electron donor levels in the band gap. Therefore, Co impurities in the lattice are locally compensated by electrically inactive oxygen vacancies. If there is additional oxygen vacancies not associated with Co sites, they exhibit the n-type behavior. These experiments suggest that Co impurities are magnetically coupled by electrons in the conduction band, resulting in ferromagnetism via an electron-mediated exchange interaction.

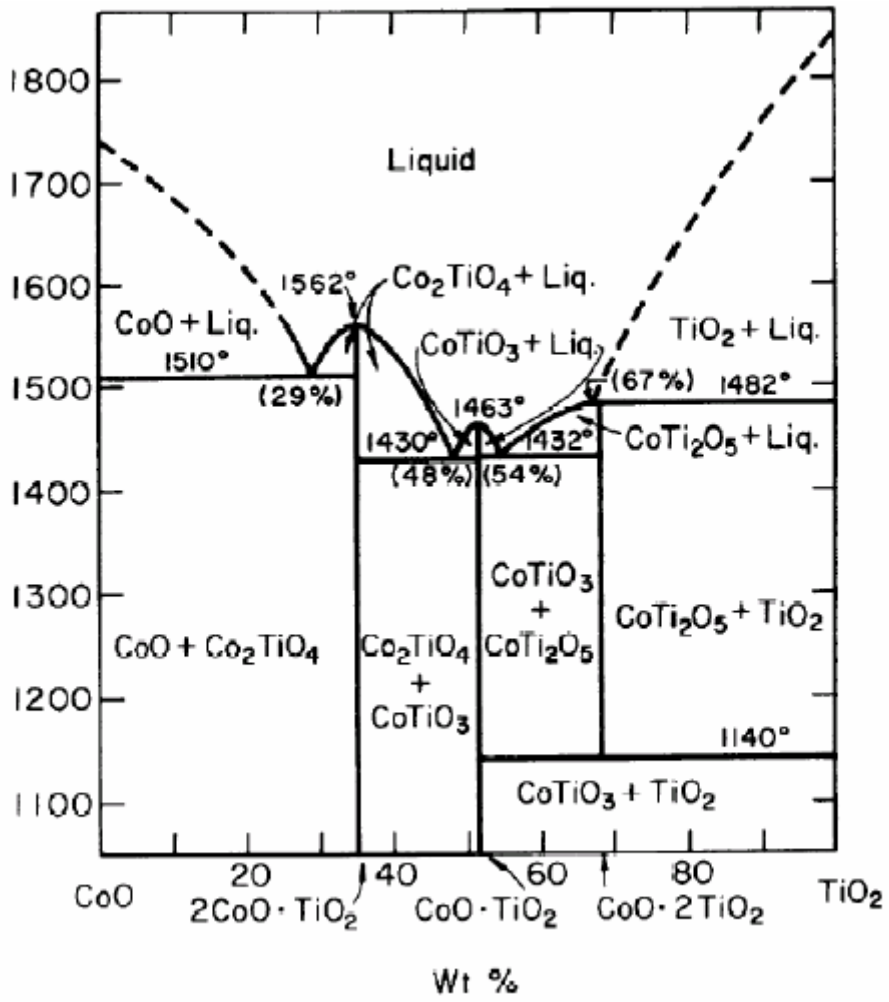

Figure 4.1 Phase relations and stabilities of compounds in the system CoO-TiO_2[17]

4.2 Experiment

TiO_2 thin films were grown on single crystal (100) LAO substrate at a substrate temperature of 550 °C by pulsed laser deposition. The distance between the target and the substrate was 4 cm. The base pressure of the deposition chamber was 5 mTorr.

There is a constant oxygen flow to maintain oxygen pressure at 20 mTorr during the deposition. After the deposition, films were annealing in-situ at 550 °C for 15 min.

Table 4.2 summarizes conditions of the fabrication of LSMO thin films.

Pulsed Laser Deposition		
Substrate		LAO (100)
Target-to-substrate distance (cm)		4
Temperature (°C)		600
Laser	**Energy (mJ)**	220
	Frequency (Hz)	10
Oxygen pressure (mTorr)		20
Duration (min)		10
In-situ annealing time (min)		15

Table 4.2 Parameters of TiO_2 fabrication using pulsed laser deposition.

4.3 Results

4.3.1 Structural and morphology characterization

The *θ-2θ* scan of TiO_2 thin film grown on LAO (100) single crystal substrate is shown in Figure 4.2. Since only the anatase (004) peak is observed, it indicates the growth of pure anatase phase TiO_2 thin film on LAO. From the phi scan shown in Figure 4.3, TiO_2 was epitaxially grown on LAO as the four characteristic peaks of TiO_2 match those that of LAO. Figure 4.4 shows the rocking curve of the thin film in (004) orientation. The FWHM is found to be 0.16°. In addition to crystallinity, we have examined the TiO_2 film morphology by AFM. Figure 4.4 shows the AFM image of a TiO_2 thin film with area 3 x 3 μm^2. The rms surface roughness of the film is found to be 4 nm.

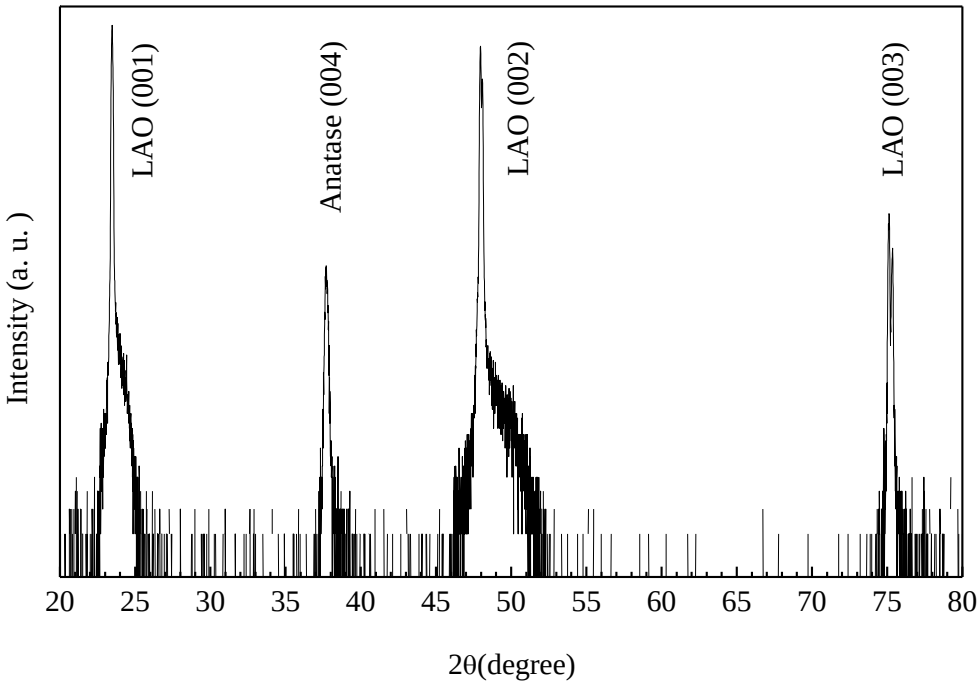

Figure 4.2 X-Ray θ-2θ diffraction pattern of TiO_2/LAO structure

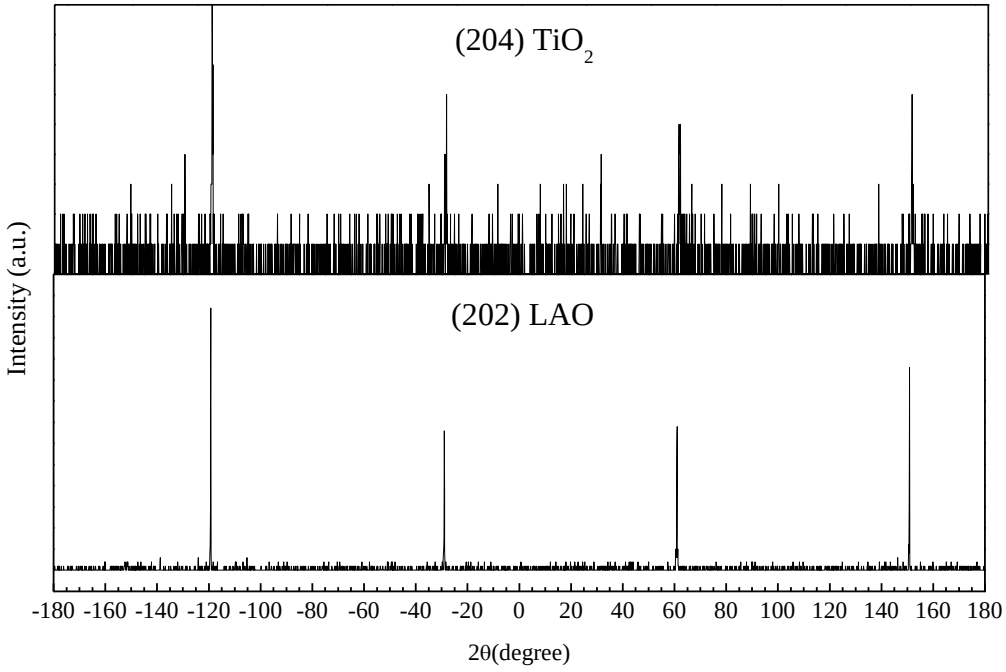

Figure 4.3 360° ϕ-scans of TiO_2 thin film on LAO

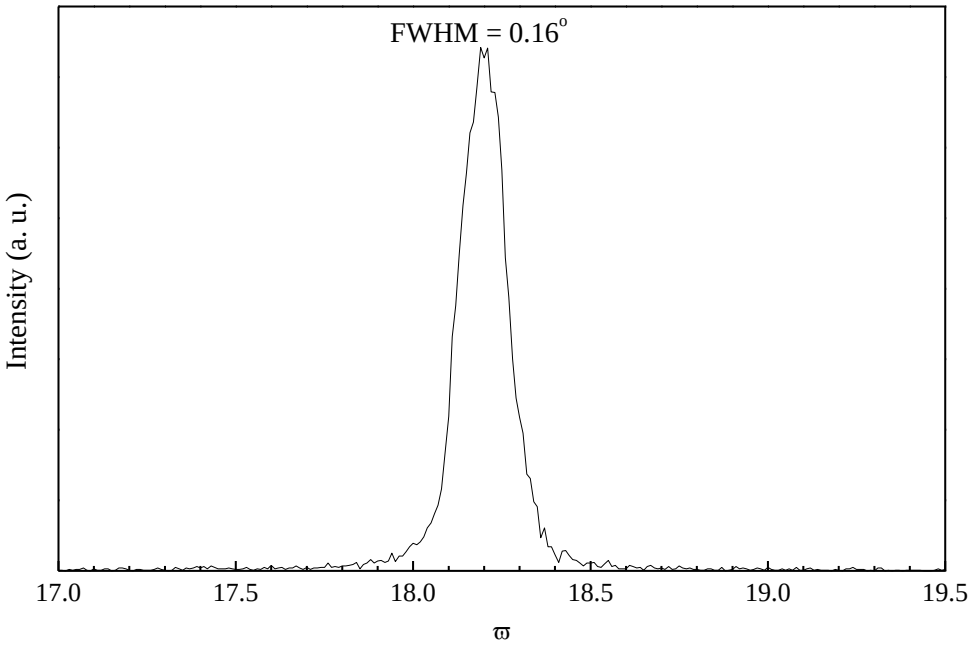

Figure 4.4 The rocking curve of TiO_2 thin film

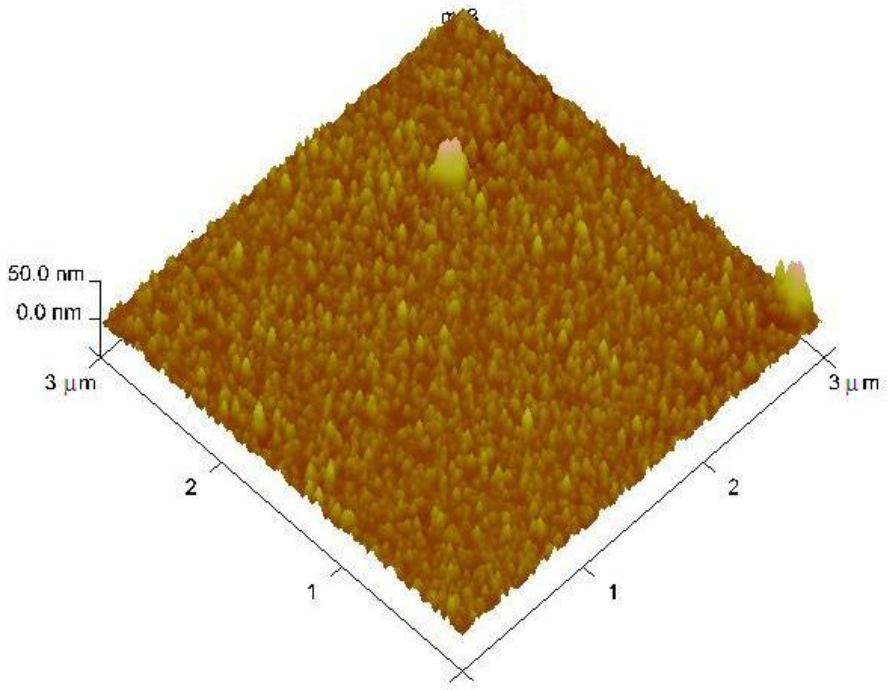

Figure 4.5 AFM image of TiO_2 thin film on LAO substrate

4.3.2 Electrical characterization

The pure anatase titanium dioxide thin film is an insulator. After doping with Co, its conductivity has been improved to a measurable range. Figure 4.6 shows the RT measurement of the 10% cobalt doped titanium dioxide at a temperature range from 180 K to 380 K. It shows the film is a semi-conductor as its resistivity decreases with increasing temperature. In fact, its resistivity was found to be 5.9 kΩ-cm at 380 K. However, the similar measurement can not perform on the 5% Co doped titanium dioxide thin film because of the high resistivity.

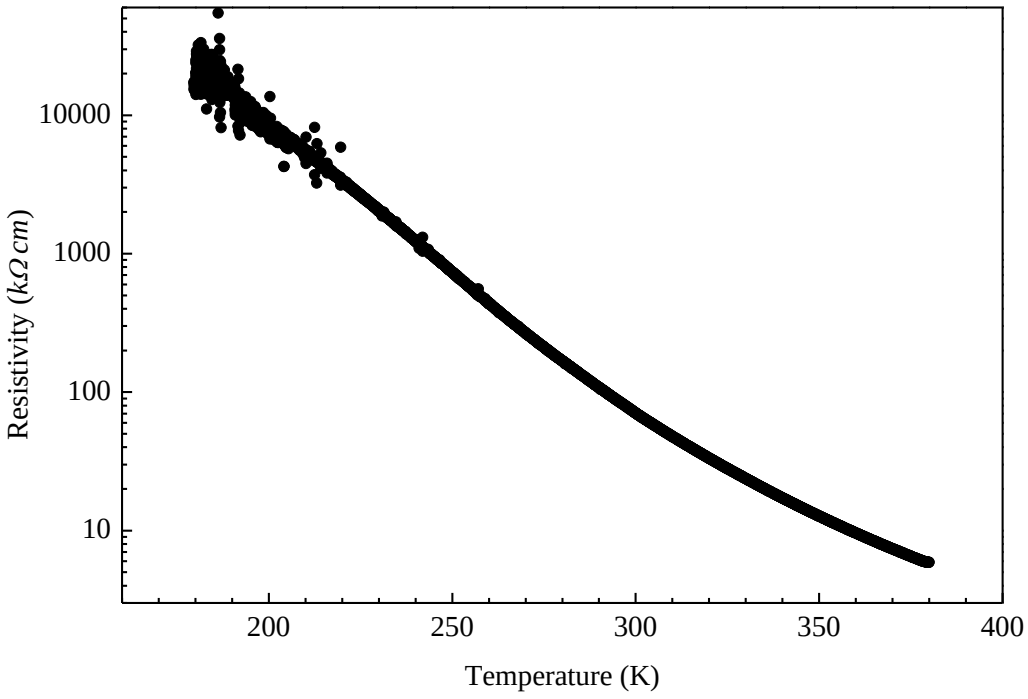

Figure 4.6 RT measurement of $Co_{0.1}Ti_{0.9}O_2$.

4.3.3 Optical characterization

Room temperature transmission $T(\omega)$ and reflection $R(\omega)$ measurements of near-normal incidence light at frequencies (ω) from 1.55 to 6 eV were performed using a Fourier transform spectrometer. By numerically inverting the Fresnel formulas for T and R, we obtain the complex index of refraction $\tilde{n} = n + ik$ without the need for Kramers-Kronig analysis [6, 7]. From $\tilde{n}$ (ω), we may derive other optical constants, e.g., the optical absorption α (ω) or the complex optical conductivity σ(v).

Historically, the spectral dependence of the band edge is characterized using the absorption coefficient, $\alpha = 4\pi\omega k$, where ω is the frequency in cm^{-1} and k is the extinction coefficient (k = Im $\{\tilde{n}\}$). At photon energies above the band gap E_g, $\alpha \propto (\hbar\omega - E_g)^{1/2}$ for a direct gap while $\alpha \propto (\hbar\omega - E_g)^2$ for an indirect gap. For TiO_2, band-structure calculations predict a direct gap at an energy level just lower than the onset of indirect transitions.

Consistent with the behavior of a direct gap, we plot α^2 versus frequency in Figure 4.7. Linear fits to the high-frequency part above the band-edge onset are extrapolated to zero absorption, giving the direct band-gap energy E_g . Pure TiO_2 exhibited E_g = 4.0 eV, while $Co_{0.05}Ti_{0.95}O_2$ and $Co_{0.1}Ti_{0.9}O_2$ are 4.1 eV and 4.2 eV respectively.

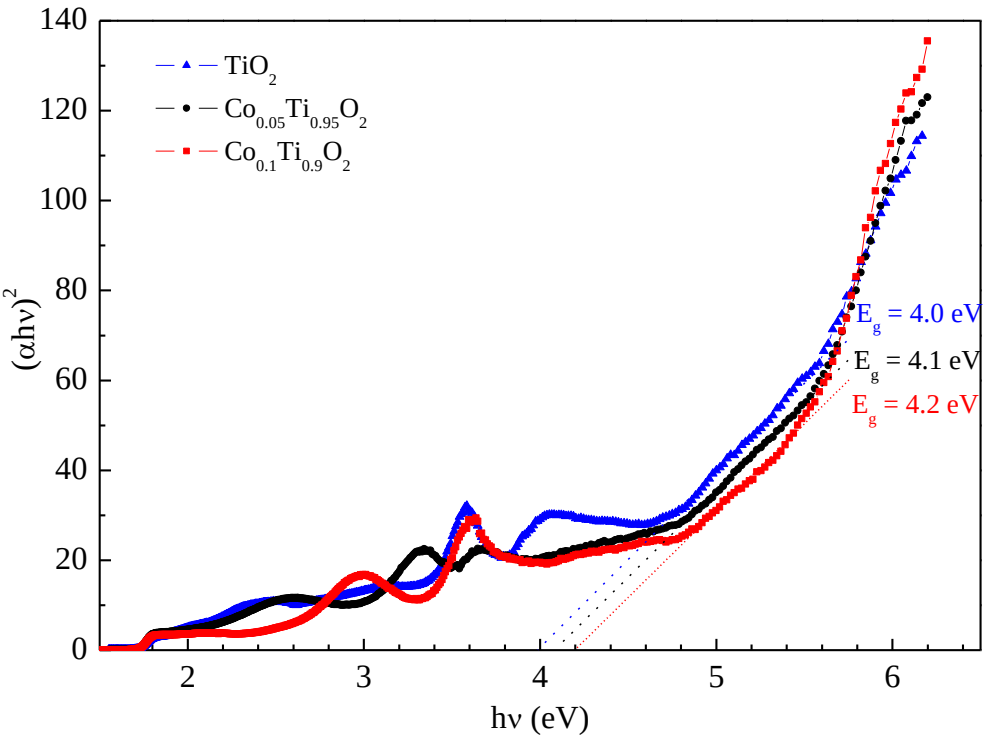

Figure 4.7 Optical measurements of pure TiO_2, $Co_{0.05}Ti_{0.95}O_2$ and $Co_{0.1}Ti_{0.9}O_2$.

4.3.4 Magnetic properties

The magnetic properties of pure TiO_2, $Co_{0.05}Ti_{0.95}O_2$ and $Co_{0.1}Ti_{0.9}O_2$ were investigated by using VSM under room temperature. Pure TiO_2 thin film was not ferromagnetic while the cobalt doped TiO_2 thin films gave a hysteresis response under the applied field. The coercive field of $Co_{0.05}Ti_{0.95}O_2$ film and $Co_{0.1}Ti_{0.9}O_2$ film were 80 G and 70 G respectively. The saturation magnetization of $Co_{0.05}Ti_{0.95}O_2$ film was about 3 μemu while $Co_{0.1}Ti_{0.9}O_2$ film was about 5 μemu at room temperature.

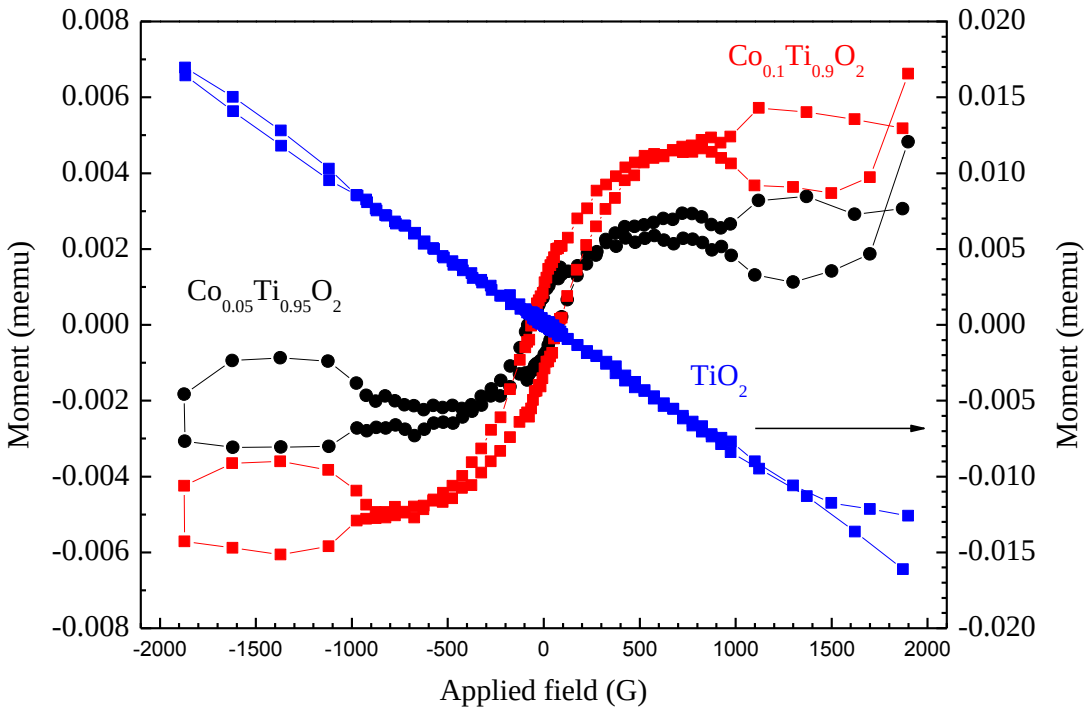

Figure 4.8 M-H plots of of pure TiO_2, $Co_{0.05}Ti_{0.95}O_2$ and $Co_{0.1}Ti_{0.9}O_2$.

4.4 Discussions

The XRD experimental results suggest that the titanium dioxide films are of pure anatase phase with high quality crystallinity. Although anatase titanium dioxide is not a stable phase when compared with rutile, there is no rutile phase observed by XRD. Both anatase and rutile exhibit a square surface mesh along the (001) orientation with a lattice constant of 3.78 Å and 4.59 Å respectively, as does the perovskite LAO, for which the lattice constant is 3.79 Å. Thus, the lattice mismatch between anatase and LAO, which is defined as $(a_{film} - a_{substrate})/a_{substrate}$, is only ~ 0.26 % while that between rutile and LAO is 21.1 %. It makes LAO a good substrate for the growth of TiO_2 anatase films

along (001) direction with such small lattice mismatch.

It was confirmed that the fabrication condition was also suitable for the growth of cobalt doped titanium dioxide. The rest of the cobalt doped titanium dioxide thin films in the present investigation are all grown under the same condition, if not specified.

The resistivity of the titanium dioxide film has been improved after being doped with Co. The films became more conductive with higher Co concentration. Upon doping Co, it is believed that the Ti^{4+} site is being substituted by Co^{2+} ion, generating more oxygen vacancies and hence lowering the resistivity. From Figure 4.6, it can be deduced that Co doped TiO_2 is semiconducting oxide as its resistance increased with the falling temperature.

In a detailed study of the absorption edge of single crystal anatase TiO_2, Simpson *et al*.[18] report a band edge with E_g = 3.420 eV and tentatively assigns the transition to a direct gap. However, we found that our TiO_2 with E_g = 4.0 eV. Consistent with the behavior of a direct gap, we plot α^2 versus frequency in Figure 4.5. Linear fits to the high-frequency part above the band-edge onset are extrapolated to zero absorption, giving the direct band-gap energy E_g. Pure TiO_2 exhibits E_g = 3.6 eV. With increasing Co concentration *x*, the band edge shifts to higher frequencies, showing a maximum blue shift of 0.1 eV for x = 0.05 and 0.1 eV for x = 0.1.

It has been reported that the oxygen deficient TiO_2 shows ferromagnetic property

at room temperature. [19] The ferromagnetism is caused by oxygen deficiency. Since the formation of oxygen vacancies is accompanied with the transformation of Ti^{4+} ion to Ti^{3+} ion for charge neutralization, magnetic moment could exist in the distorted lattice. There is no ferromagnetism in pure TiO_2 confirmed by our VSM measurement. It might be due to two reasons. First of all, the signal of it was too weak to be detected by our VSM. Secondly, the condition of fabrication (20 mTorr O_2 pressure) was not low enough to grow an oxygen deficient TiO_2 film possessing ferromagnetism.

4.5 References

1. H. Zhang & J. F. Banfield, "Understanding Polymorphic Phase Transformation Behavior during Growth of Nanocrystalline Aggregates: Insights from TiO_2," *J. Phys. Chem. B*, vol. 104, p. 3481, 2000.
2. U. Diebold, N. Ruzycki, G.S. Herman & A. Selloni, "One step towards bridging the materials gap: surface studies of TiO_2 anatase," *Catalysis Today*, vol. 85, p. 93, 2003.
3. R. O'Regan & M. Gratzel, "A low-cost, high-efficiency solar cell based on dye-sensitized colloidal TiO_2 films," *Nature*, vol. 353, p. 737, 1991.
4. K.I. Hadjiivanov & D.G. Klissurski, "Surface chemistry of titania (anatase) and titania-supported catalysts," *Chem. Soc. Rev.*, vol. 25, p. 61, 1996.
5. A.L. Linsebigler, G. Lu & J.T. Yates, "Photocatalysis on TiOn Surfaces: Principles, Mechanisms, and Selected Results," *Chem. Rev.*, vol. 95, p. 735, 1995.
6. S.D. Mo & W.Y. Ching, "Electronic and optical properties of the three phases of titanium dioxide: Rutile, anatase and brookite," *Phys. Rev. B*, vol. 51, no. 19, p. 13023, 1995.
7. S. Chen, M. G. Mason, H. J. Gysling, G. R. Paz-Pujalt, T. N. Blanton, TM. Chen, C. P. Fictorie, W. L. Gladfelter, A. Franciosi & P. I. Cohen, "Ultrahigh vacuum metalorganic chemical vapor deposition growth and in situ characterization of epitaxial TiO_2 films," *J. Vac. Sci. Tech. A*, vol.11, p. 2419, 1993
8. W. Sugiyama, A. Yamazaki, H. Shigetani, J. Tanaka & T. Mitsuhashi, "Anatase-type TiO2 thin films produced by lattice deformation, " *Jap. J. App. Phys.*, vol 36, p. 7358, 1997.
9. M. Murakami, Y . Matsumoto, K. Nakajima, T. Makino, Y. Segawa, T. Chikyow, P.Ahmet, M. Kawasaki & H. Koinuma, "Anatase TiO2 thin films grown on lattice-matched $LaAlO_3$ susbstrate by laser molecular-beam epitaxy," *Appl. Phys. Lett.*, vol. 78, p. 2664, 2001.
10. Y. Matsumoto, M. Murakami, T. Shono, T. Hasegawa, T. Fukumura, M. Kawasaki, P. Ahmet, T. Chikyow, S.-Y. Koshihara & H. Koinuma, "Room-Temperature Ferromagnetism in Transparent Transition Metal-Doped Titanium Dioxide," *Science* vol. 291, p. 854, 2001.
11. S. A. Chambers, S. Thevuthasan, R. F. C. Farrow, R. F. Marks, J. U. Thiele, L. Folks, M. G. Samant, A. J. Kellock, N. Ruzycki, D. L. Ederer, & U. Diebold, "Epitaxial growth and properties of ferromagnetic co-doped TiO_2 anatase," *Appl. Phys. Lett.*, vol. 79, p. 3467, 2001.
12. J.-Y. Kim, J. H. Park, B.-G. Park, H.-J. Noh, S.-J. Oh, J. S. Yang, D.-H. Kim, S. D. Bu, T. W. Noh, H.-J. Lin, H. H. Hsieh & C. T. Chen, "Ferromagnetism Induced by

Clustered Co in Co-Doped Anatase TiO_2 Thin Films," *Phys. Rev. Lett.*, vol. 90, p. 017401, 2003.

13. S. R. Shinde, S. Ogale, S. Das Sarma, J. R. Simpson, H. D. Drew, S. Lofland, C. Lanci, J. P. Buban, N. D. Browning, V. N. Kulkarni, J. Higgins, R. P. Sharma, R. L. Greene & T. Venketesan, "Ferromagnetism in laser deposited anatase $Ti_{1-x}Co_xO_{2-\delta}$ films," *Phys. Rev. B*, vol. 67, p. 115211, 2003.
14. S. R. Shinde, S. Ogale, J. Higgins, H. Zheng, A. J. Millis, R. Ramesh, R. L. Greene & T. Venketesan, "Co-occurrence of Superparamagnetism and Anomalous Hall Effect in Highly Reduced Cobalt-Doped Rutile $TiO_{2-\delta}$ Films," *Phys. Rev. Lett.*, vol. 92, p. 166601, 2004.
15. A. Kaminski & S. Das Sarma, "Polaron Percolation in Diluted Magnetic Semiconductors," *Phys. Rev. Lett.*, vol. 88, p. 247202, 2002.
16. J. M. D. Coey, M. Venkatesan & C. B. Fitzgerald, "Donor impurity band exchange in dilute ferromagnetic oxides," *Nature Materials*, vol. 4, p. 173, 2005.
17. B. Brezny & A. Muan, "Phase relations and stabilities of compounds in the system CoO-TiO_2, " *J. Inorganic and Nuclear Chem.*, vol 31, p. 649, 1969.
18. J. R. Simpson & H. D. Drew, "Optical band-edge shift of anatase $Ti_{1-x}Co_xO_{2-\delta}$, " *Phys. Rev. B*, vol. 69, p. 193205, 2004.
19. N.H. Hong, J. Sakai, N. Poirot & V. Brize, "Room-temperature ferromagnetism observed in undoped semiconducting and insulating oxide thin films, " *Phys. Rev. B*, vol. 73, p. 132404, 2006

Chapter 5
Cobalt doped TiO_2 and $La_{0.7}Sr_{0.3}MnO_3$ heterojunction

5.1 Introduction

LSMO and cobalt doped TiO_2 (CTO) are known to be p-type and n-type semiconducting oxides respectively. In this chapter, we demonstrate the epitaxial growth of cobalt doped TiO_2 onto (001) oriented LSMO. The CTO/LSMO heterojunction could be considered a p-n junction as it consisted of p-type and n-type semi-conductors.

The heterostructure thus obtained are characterized using XRD and SEM. Titanium dioxide with 5 at.% and 10 at.% cobalt were investigated in order to further the study of electrical properties and magnetic properties of the junctions, i.e. $Co_{0.05}Ti_{0.95}O_2$/LSMO and $Co_{0.1}Ti_{0.9}O_2$/LSMO junctions were fabricated.

5.2 Experiment

The growth of two-layer heterostructure by PLD followed the same conditions of single layer fabrication mentioned in the previous two chapters. The substrate used was also single crystal LAO. LSMO was first deposition on LAO substrate. Then CTO was then grown on top of the LSMO layer. The PLD chamber was opened once for changing

the LSMO target to CTO target as it was a single target holder.

		LSMO	$Co_{0.05}Ti_{0.95}O_2$	$Co_{0.1}Ti_{0.9}O_2$
Substrate		LAO (100)	LSMO/LAO (100)	LSMO/LAO (100)
Target-to-substrate distance (cm)		4	4	4
Temperature (°C)		650	600	600
Laser	**Energy (mJ)**	220	220	220
	Frequency (Hz)	5	10	10
Oxygen pressure (mTorr)		150	20	20
Duration (min)		10	10	10
In-situ annealing time (min)		15	15	15

Table 5.1 The condition of heterojunction fabrication.

The parameters used for the fabrication are listed in Table 5.1. The area of junctions was defined during the second layer deposition (CTO) by using a stainless steel shadow mask with 0.5 x 0.5 mm square array. Platinum was deposited on the LSMO layer as electrode while silver was deposited on the CTO layer. All electrodes were deposited at room temperature using PLD method. The choice of electrode material is matched according to the work function of the two layers.

The rectifying property of a *p-n* junction was verified by current-voltage measurement using a source meter (Keithley 2410). The configuration of the heterojunction for the measurement is shown in Figure 5.1.

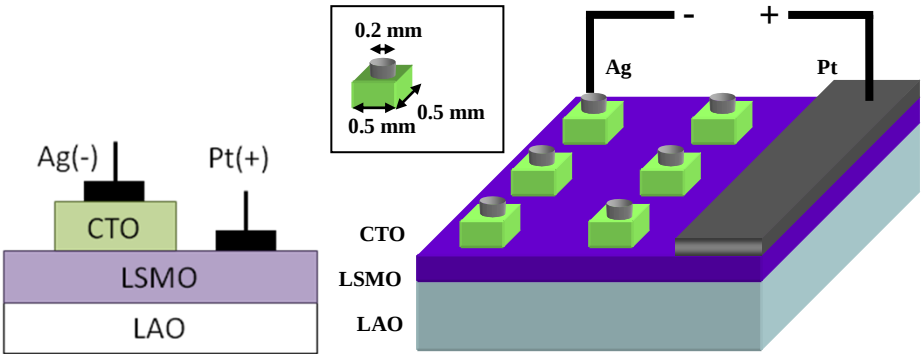

Figure 5.1 Configuration of the heterojunction

5.3 Results

5.3.1 Structural Characterization

Figure 5.2 and 5.3 show the *θ-2θ* scan of $Co_{0.05}Ti_{0.95}O_2$/LSMO and $Co_{0.1}Ti_{0.9}O_2$/LSMO junctions respectively. They clearly demonstrate that pure (004) anatase cobalt-doped titanium dioxide thin films have been grown on the (001) oriented LSMO layer. The 360° ϕ scans corresponding to the two layers and the substrate (Figure 5.4) also prove that the films were epitaxial growth on the substrates. The asterisks mark satellite peaks of LAO.

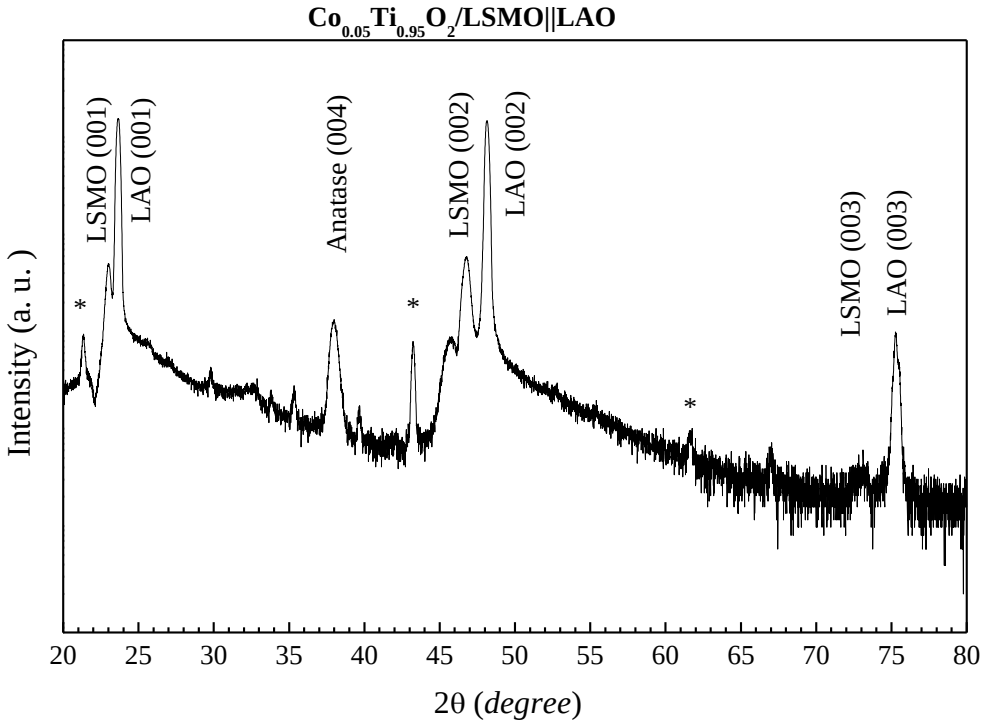

Figure 5.2 X-Ray *θ-2θ* diffraction pattern of $Co_{0.05}Ti_{0.95}O_2$/LSMO||LAO structure.

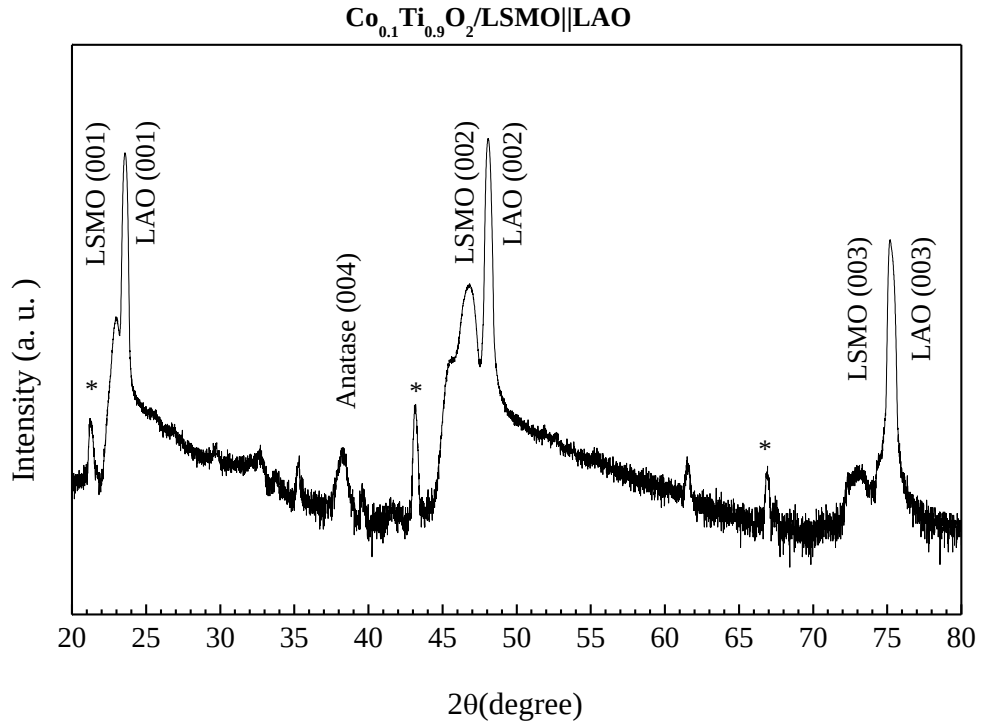

Figure 5.3 X-Ray *θ-2θ* diffraction pattern of $Co_{0.1}Ti_{0.9}O_2$/LSMO||LAO structure.

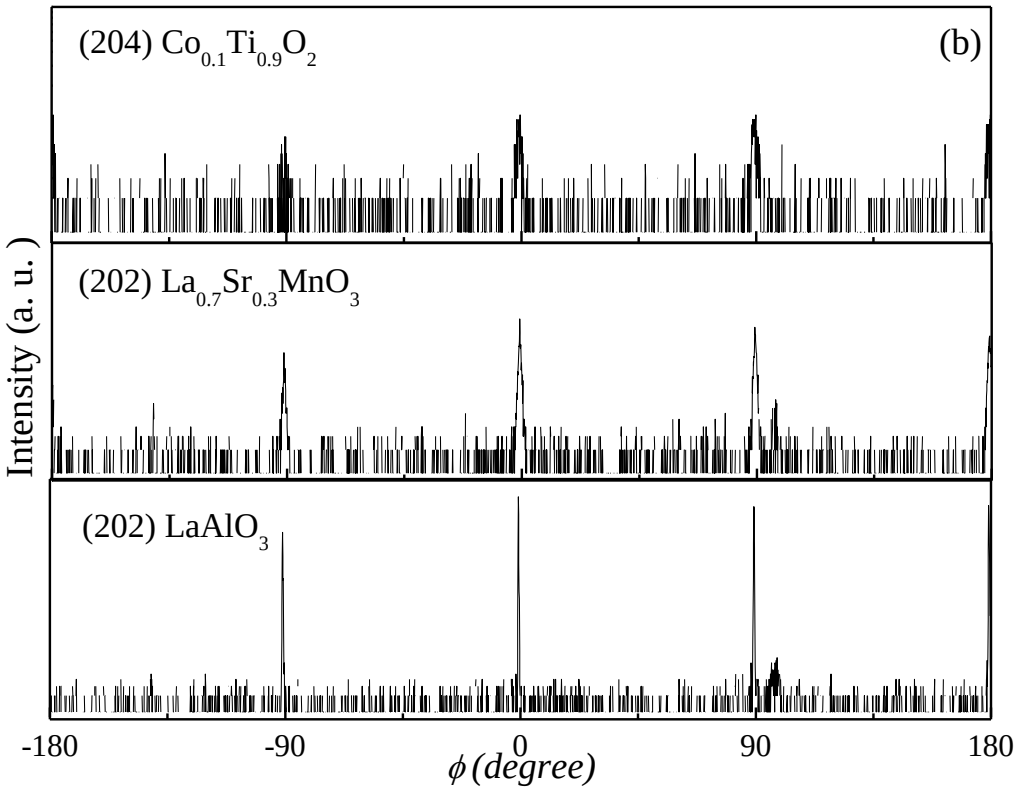

Figure 5.4 360° ϕ-scans of $Co_{0.05}Ti_{0.95}$/LSMO||LAO structure

5.3.2 Cross-section investigation by SEM

The cross-section of the junctions were observed using SEM. Figure 5.5 and Figure 5.6 show the cross-section of $Co_{0.05}Ti_{0.95}O_2$(400)||LSMO(100)||LAO(100) and $Co_{0.1}Ti_{0.9}O_2$(400)||LSMO(100)||LAO(100) respectively.

For $Co_{0.05}Ti_{0.95}O_2$(400)||LSMO(100)||LAO(100) heterojunction, the thickness of $Co_{0.05}Ti_{0.95}O_2$ and LSMO were 130 nm and 100 nm respectively.

For $Co_{0.1}Ti_{0.9}O_2$(400)||LSMO(100)||LAO(100) heterojunction, the thickness of $Co_{0.1}Ti_{0.9}O_2$ and LSMO were 120 nm and 100 nm respectively.

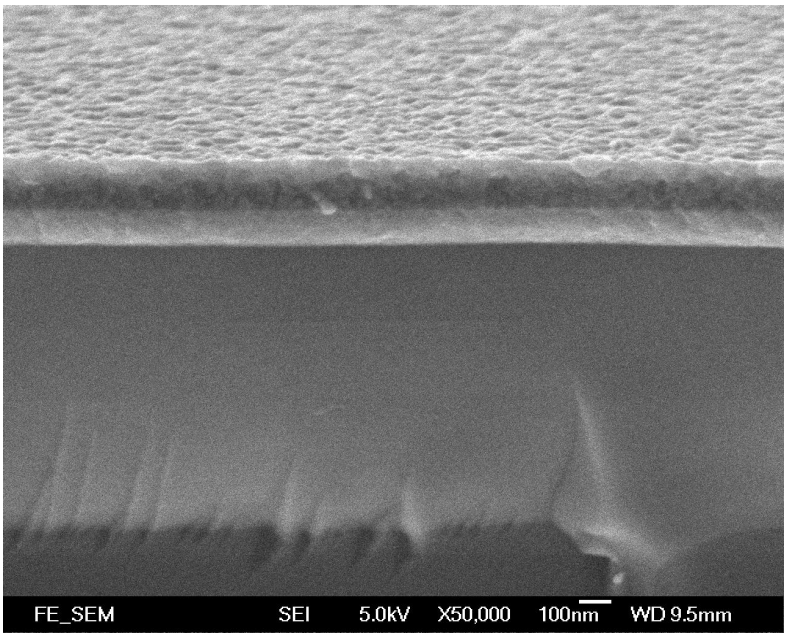

Figure 5.5 The cross-section of $Co_{0.05}Ti_{0.95}O_{2(400)}||LSMO_{(100)}||LAO_{(100)}$

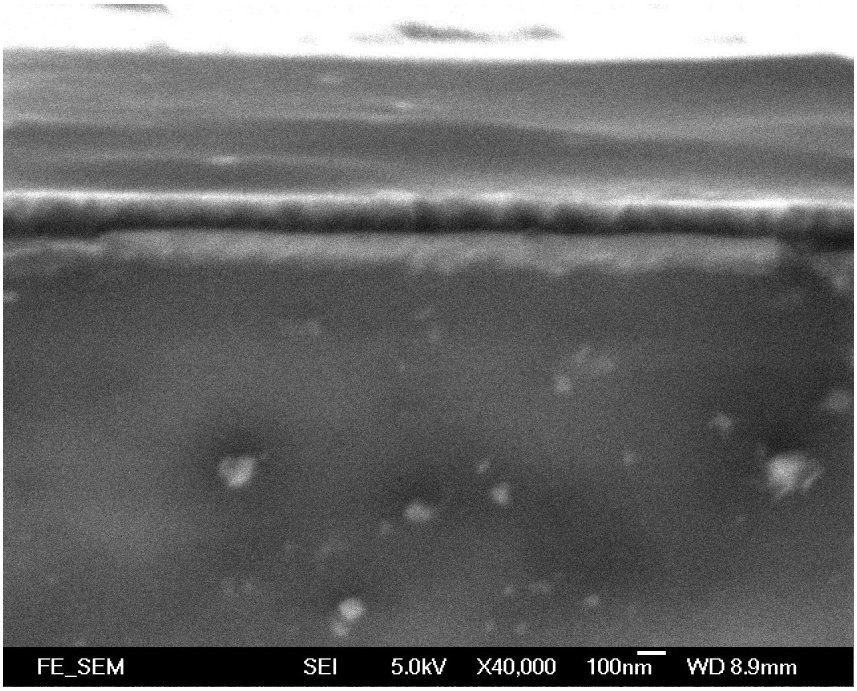

Figure 5.6 The cross-section of $Co_{0.1}Ti_{0.9}O_{2(400)}||LSMO_{(100)}||LAO_{(100)}$

5.3.3 Surface morphology

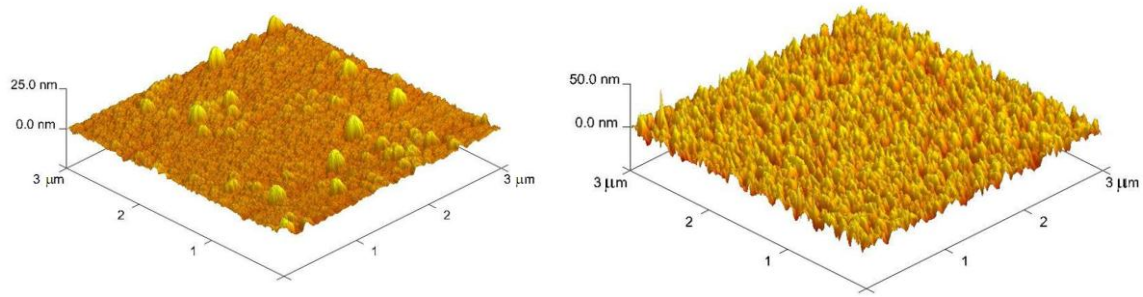

(a) (b)

Figure 5.7 AFM images of (a) LSMO and (b) $Co_{0.1}Ti_{0.9}O_2$

5.3.4 I-V measurement

Figure 5.8 and 5.9 show the I-V curves of $Co_{0.05}Ti_{0.95}O_2$/LSMO||LAO and $Co_{0.1}Ti_{0.9}O_2$/LSMO||LAO at 100 K, 200 K and 300 K respectively. Both all-oxide junctions have demonstrated good rectifying profiles and their current rectifying ratios are all of high values. At 300 K, the current rectifying ratios of $Co_{0.05}Ti_{0.95}O_2$/LSMO||LAO and $Co_{0.1}Ti_{0.9}O_2$/LSMO||LAO are 1092 and 953 respectively.

However, the rectifying ratio of $Co_{0.05}Ti_{0.95}O_2$/LSMO||LAO decreases with decreasing temperature while that of $Co_{0.1}Ti_{0.9}O_2$/LSMO||LAO increases with dropping temperature. Figure 5.10 and Figure 5.11 give the *I-V* curves plotted in logarithm scale at forward bias under 300 K, 200 K and 100 K for determination of ideality factor, which is discussed in details later.

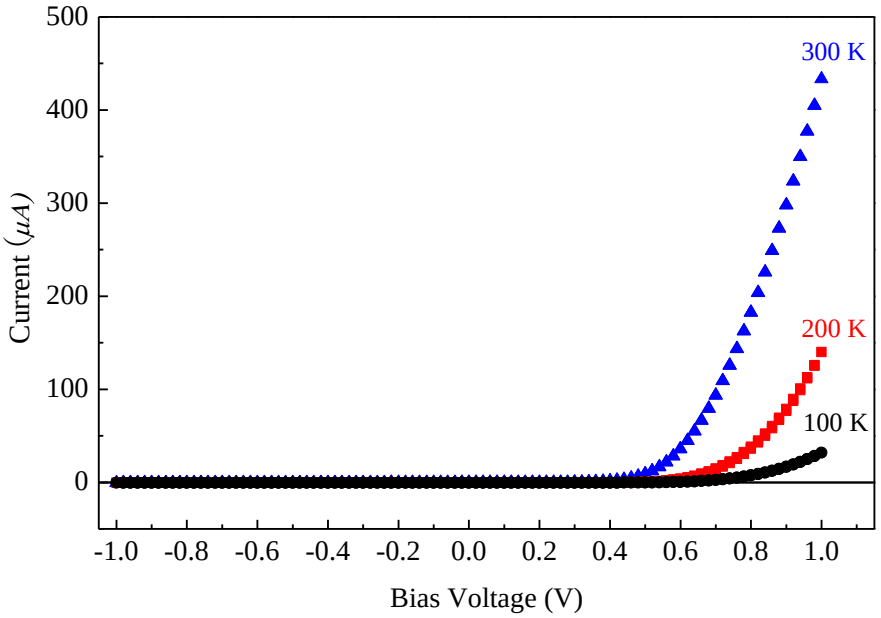

Figure 5.8 *I-V* characteristic of $Co_{0.05}Ti_{0.95}O_2$ /LSMO/LAO

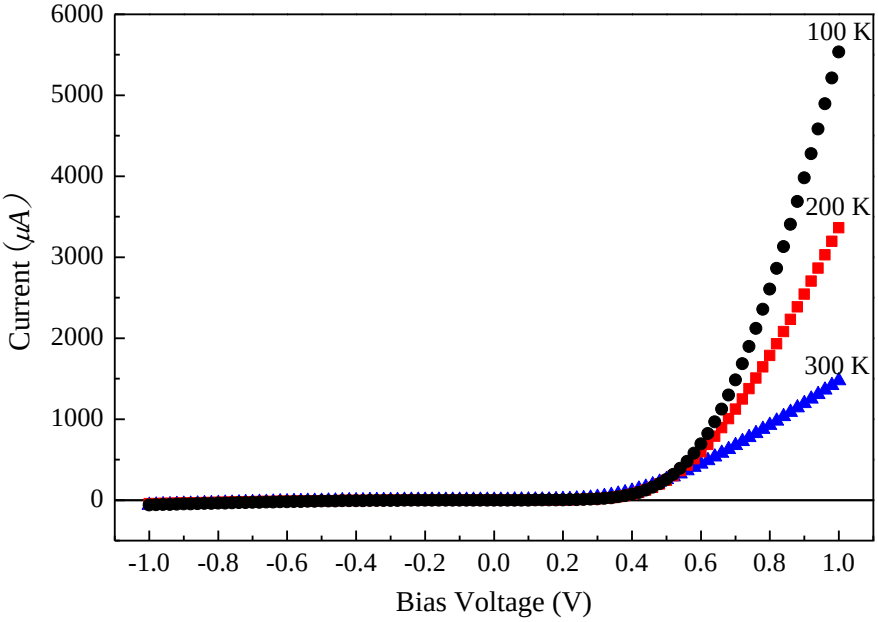

Figure 5.9 *I-V* characteristic of $Co_{0.1}Ti_{0.9}O_2$ /LSMO/LAO

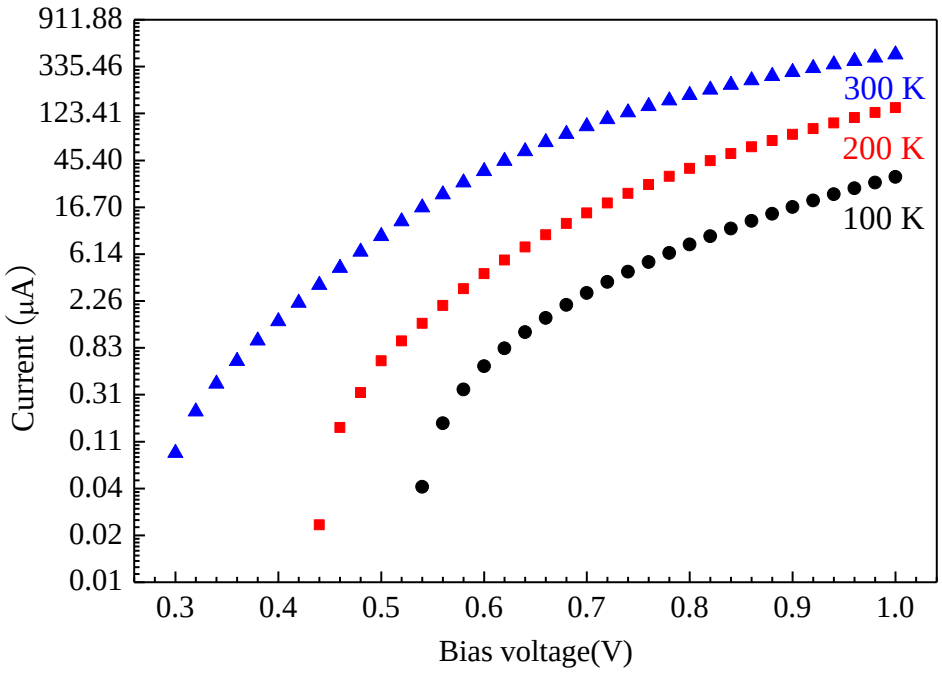

Figure 5.10 *I-V* curves plotted in logarithm scale of $Co_{0.05}Ti_{0.95}O_2$ /LSMO/LAO

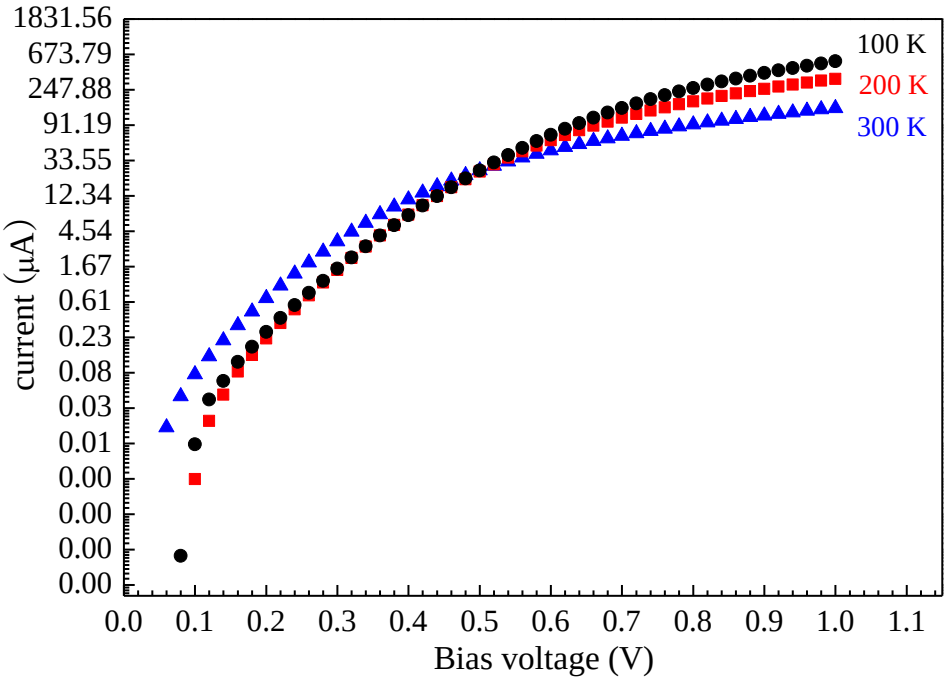

Figure 5.11 *I-V* curves plotted in logarithm scale of $Co_{0.1}Ti_{0.9}O_2$ /LSMO/LAO

5.3.5 VSM measurement

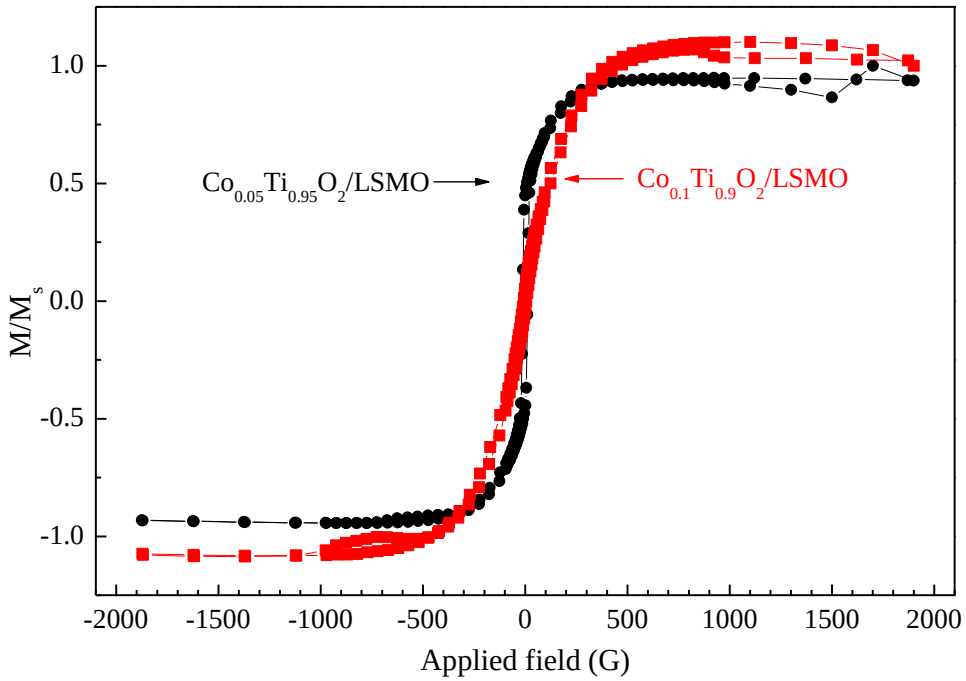

Figure 5.12 M-H plot of Co-doped TiO_2 thin films at room temperature while in-plane field was applied

5.4 Discussions

With the evidence of XRD results, cobalt doped titanium dioxide thin films were epitaxally grown on the LSMO layer. The lattice parameters are:

	LSMO	**$Co_{0.05}Ti_{0.95}O_2$**	**$Co_{0.1}Ti_{0.9}O_2$**
Lattice Constant	a = 3.88	c = 9.48	c = 9.20

I-V characteristics of the $Co_{0.05}Ti_{0.95}O_2$/LSMO/LAO heteroepitaxial junction at temperature ranging from 100 K to 300 K are shown in Figure 5.10 Good ohmic contacts of metal electrodes and oxide layers were confirmed by two-probe electrical

measurement. It ensured that the rectifying behaviours were primarily due the junction. As revealed in Figure 5.11, a current rectifying ratio (|I (1 V)/I (-1 V)|) of 1092 at 300 K was obtained.

The measured *I-V* characteristics were fit to the expression,

$$I = I \exp(\frac{qV}{\eta k_B T}) \quad \ldots (5.1)$$

where η is the ideality factor defined by the expression,

$$\eta = \frac{q}{k_b T} \frac{dV}{dInI} \quad \ldots (5.2)$$

The ideality factor is commonly used to determine the origin of diode currents: junction conduction is dominated by diffusion when η = 1, generation and recombination when η = 2, and defect assisted tunneling when η > 2. [1-2]

Figure 5.11 and 5.12 give the *I-V* curve plot in logarithm scale at forward bias under 300 K, 200 K and 100 K for determination of ideality factor. For $Co_{0.05}Ti_{0.95}O_2$/LSMO/LAO, η = 1 occurs in the bias region between 0.30 V and 0.34 V at 300 K. This indicates that diffusion current dominates the junction conduction. The conduction mechanism of the junction changes from diffusion to generation and recombination as the ideality factor increases from 1 to 2 between 0.34 V and 0.52 V. Defect-assisted tunneling occurs when the bias voltage is greater than 0.52 V. The change of ideality factor indicates that this junction is performed as a normal *p-n* junction. The turn-on bias voltage of the junction increases at low operating temperature.

As the operating temperature increases, electrons have larger internal energy to tunnel through or drift across the depletion layer. Hence, the turn-on bias dropped under a higher temperature.

The $Co_{0.1}Ti_{0.9}O_2$/LSMO/LAO heterostructure, however, shows a different temperature dependent *I-V* response. The ideality factor of the junction after turning-on exceeds 2 at all temperatures. This indicates that the conduction mechanism changes from generation and recombination to defect-assisted tunneling as the bias is increased. The increase in the ideality factor with the bias is attributed to series resistance. [3] This series resistance can be due to the contact resistance between the metal and the semiconductor, the resistivity of the semiconductor or the series resistance of the connecting wires. There is a gradual decrease in the series resistance with the lowering of operating temperature when $V_{bias} > 0.5$ V.

5.5 References

1. S. M. Sze, "*Physics of Semiconductor Devices," Wiley*, 1981.
2. P. Perlin, M. Osinski, P. G. Eliseev, V. A. Smagley, J. Mu, M. Banas & P. Sartori, " Low-temperature study of current and electroluminescence in InGaN/AlGaN/GaN double-heterostructure blue light-emitting diodes," *Appl. Phys. Letts.*, vol. 69, p. 1680, 1996.
3. S. J. May & B. W. Wessels, *J.Vac. Sci Technol. B*, vol. 23, p. 1769-1772, 2005.

Chapter 6
Room-temperature ferromagnetism in carbon doped titanium dioxide

Since the first report on stable ferromagnetism above room temperature in Co-doped TiO_2, various transition-metal-doped TiO_2 systems have been extensively studied. Stable ferromagnetism at above room temperature was confirmed for other magnetic dopant such as chromium (Cr) or iron (Fe) [1-4]. Unlike Co and Fe, Cr metal is not FM. However, one of its oxides, CrO_2 which is a ferromagnetic half metal might be formed during fabrication. Still, researchers cannot clearly identify the mechanism of ferromagnetism in these matrixes. Surprisingly room temperature ferromagnetism was also found for 10 at% Cu doped TiO_2 thin films [5].

Recently, room temperature ferromagnetism was found in carbon (C) doped ZnO in which carbon substitutes for oxygen [6, 7]. C-doped ZnO has received significant attention because of its potential application in spintronics. In the same vein, one might speculate that if ferromagnetism can occurs in carbon doped TiO_2. The original purpose of this work was to verify if ferromagnetism can be observed in C-doped TiO_2 thin films. Thin films are used because they have a much greater aspect ratio than polycrystalline ceramics, so the role of defects may be enhanced.

6.1 Introduction

According to the first-principles density functional theory (DFT) calculations, doping carbon may induce ferromagnetism in CdS [8] while a spin polarization was also predicted in rutile TiO_2 where C substitutes for a single O atom [9].

The theory of ferromagnetism in of C-doped anatase TiO_2 structure has been explored by performing spin polarized DFT calculations, in which C atoms substitute O atoms [11]. Figure 6.1 shows a model structure of C-doped anatase TiO_2 with C atoms at O sites constructed using the 2 x 2 x 1 supercell. The atomic positions of the doped structures are optimized by performing first principles spin-polarized DFT electronic structure calculations.

In C-doped anatase TiO_2, each C has spin-polarized 2p states in the band gap generating a magnetic moment of 2.0 μ_B with C at O sites. The magnetic coupling between adjacent C sites depends strongly on the C⋯C distance. A short C⋯C distance leads to a nonmagnetic state while a paramagnetic state occurs with a long C⋯C distance. When the C⋯C distance lies between 3–4 Å, the magnetic coupling between adjacent C sites is substantial leading to either antiferromagnetism or ferromagnetism.

To summarize, each C generates a magnetic moment of about 2.0□μ_B in C-doped anatase TiO_2 when its adjacent C is farther away than 3 Å. It exhibits ferromagnetism when two C atoms form a slightly bent C–Ti–C unit by replacing two oxygen atoms at

the opposite vertices of a TiO_6 octahedron. It is of great interest to prepare C-doped anatase TiO_2 and determine its magnetic properties.

On the other hand, non-spin-polarized DFT calculations of carbon-doped TiO_2 have found that under oxygen-poor conditions, substitutional (to oxygen) C atoms and oxygen vacancies are favored, while interstitial and substitutional (to titanium) C atoms are preferred under oxygen-rich conditions [10].

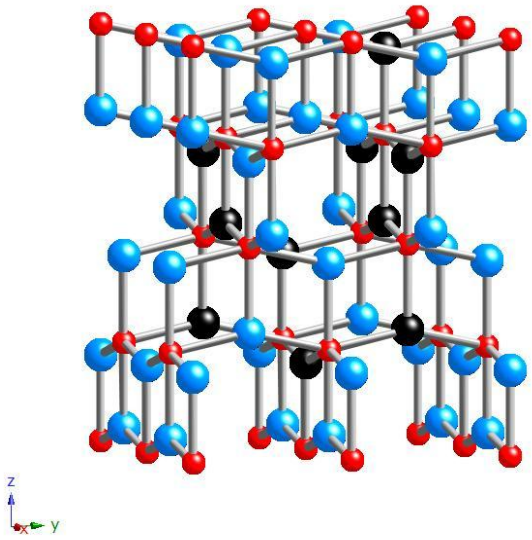

Figure 6.1 2 x 2 x 1 supercell of anatase TiO_2 employed to define model C-doped TiO_2 structures. The small red and large blue spheres represent the Ti and O atoms, respectively. The black spheres are the O sites to be replaced with C atoms. The x, y, and z axes are along the crystallographic a, b, and c directions, respectively.

6.2 Experiment

Four highly oriented (004) TiO_2 films with thickness about 200 nm was prepared on LAO substrates at 600 °C by PLD technique, as described in previous chapter. The process of carbon doping was performed in Nagoya Institute of Technology, Japan. The graphite plate serving as target was placed perpendicular to the surface of TiO_2 samples. The samples were aligned one after another in front of a graphite plate. A thin layer of carbon was deposited onto the samples. An ion beam source with 500 eV Ar^+ ions was irradiated simultaneously at an incidence angle of 45° to the target and the TiO_2 surface in order to dope carbon into the host material. Since the distances between the target and four samples were different, a gradient on the carbon content among them was expected. The samples are labeled from 1 to 4 according to their position from the target, i.e., sample 1 is the closest to the target while sample 4 is the farthest from it. The schematic diagram of the setup is shown in Figure 6.2.

The concentration of carbon was determined by XPS. Magnetic measurements were conducted using a VSM. Meanwhile, the samples were characterized by XRD before and after the carbon doping to confirm if there is any secondary phase induced after the doping process.

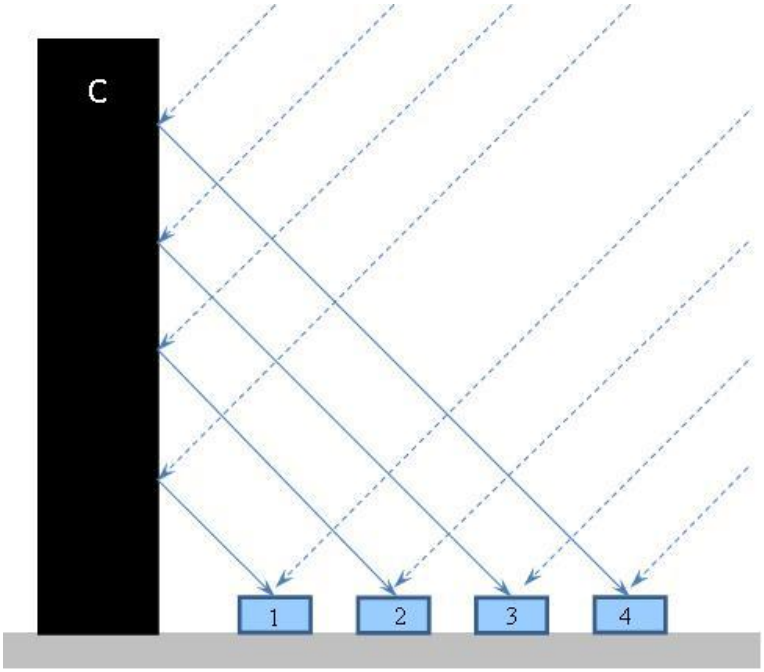

Figure 6.2 Schematic diagram of the setup during carbon doping. The dash lines represent the incident ion beam while the solid lines represent the reflected ion beam from the carbon plant.

6.3 Results

6.3.1 Structural characterization

The *θ-2θ* scans on all C doped TiO_2 thin films grown on LAO (100) single crystal substrates were performed. One of the results is shown below. *θ-2θ* scans before and after the carbon doping are shown in Figure 6.3 and Figure 6.4 respectively. Since only the anatase (004) peak is observed, it indicates no other phases are induced after the carbon doping.

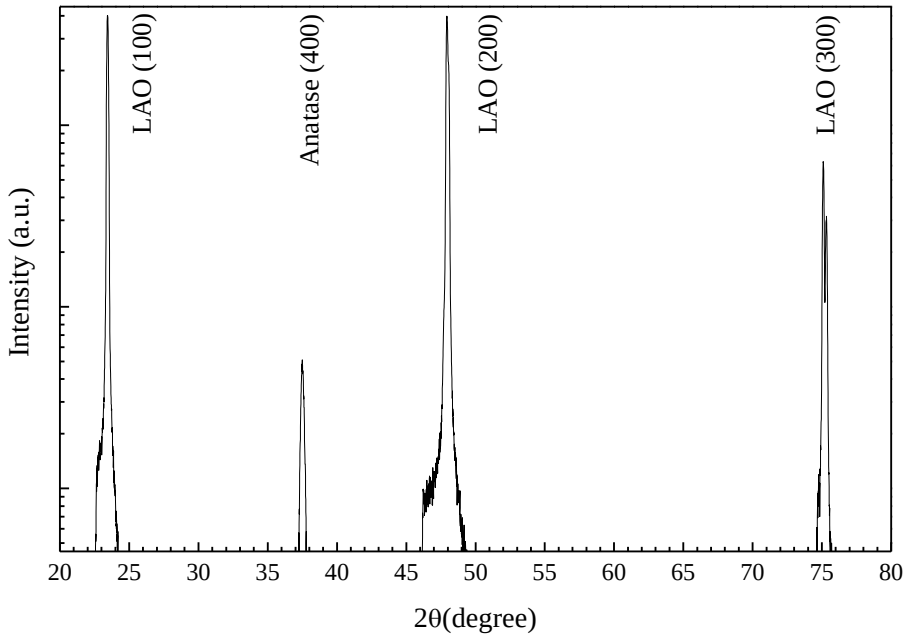

Figure 6.3 X-Ray *θ-2θ* diffraction pattern of TiO_2 before carbon doping

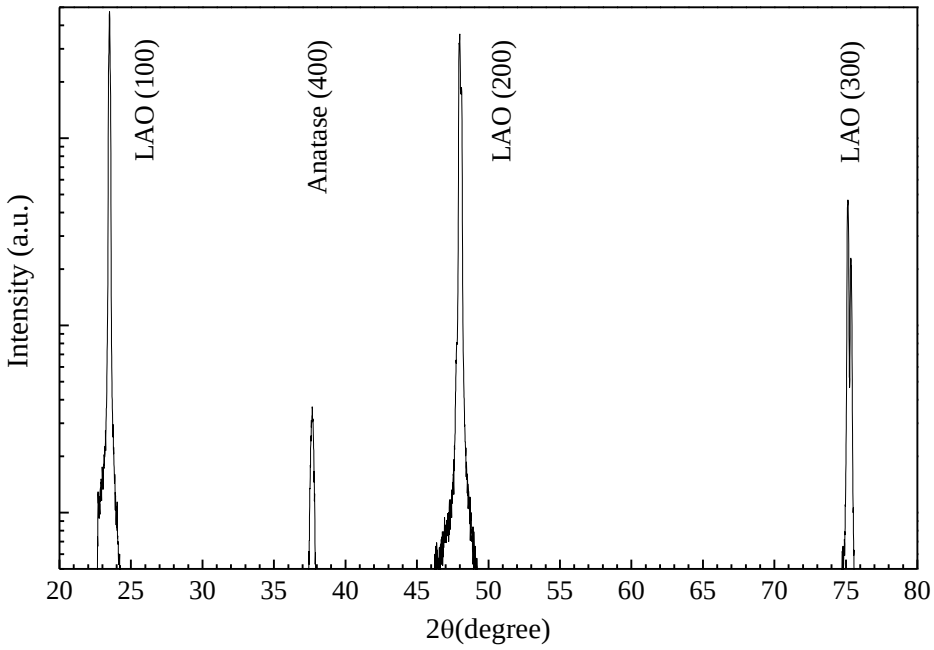

Figure 6.4 X-Ray *θ-2θ* diffraction pattern of C doped TiO_2

6.3.3 Composition analysis by XPS

Four C doped TiO_2 thin films with different C concentrations and a pure TiO_2 thin film were sent to The Hong Kong University of Science and Technology of for XPS analysis. The carbon compositions of our samples were obtained via depth profiling. An Ar ion beam of 4 keV etched the C doped TiO_2 layer at a rate of 4 nm min^{-1} (for Si). A composition scan that targeted on element Ti, O, C and Si was done every 2.5 min, assumed to be 10 nm depths relative to the last scan. The photoelectron spectra of the C 1s, Ti 2p, O 1s and Si 2p were collected. The peaks were deconvoluted with asymmetric Gauss-Lorentz profiles after subtraction of a Shirley background by using the software XPSpeak4.1. Thus, the atomic concentration as a function of time (scan depth) was obtained for all five samples. They are shown in Figure 6.5. Since the atomic concentration of all elements were steady after 2.5 min, the ratio of C:Ti and O:Ti among 5 samples at 2.5 min were plotted in Figure 6.6.

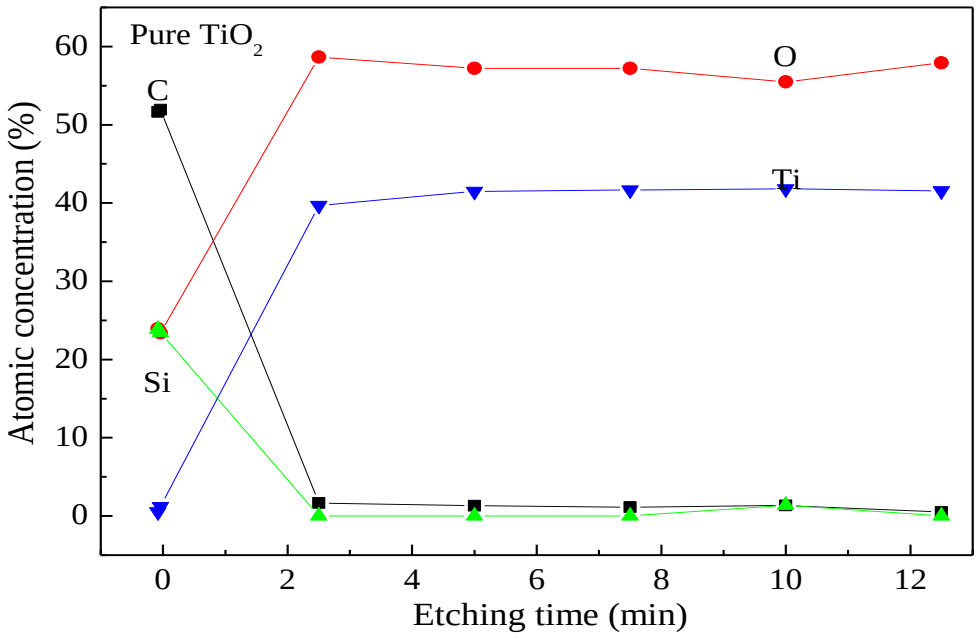

Figure 6.5a XPS depth profile of pure TiO_2

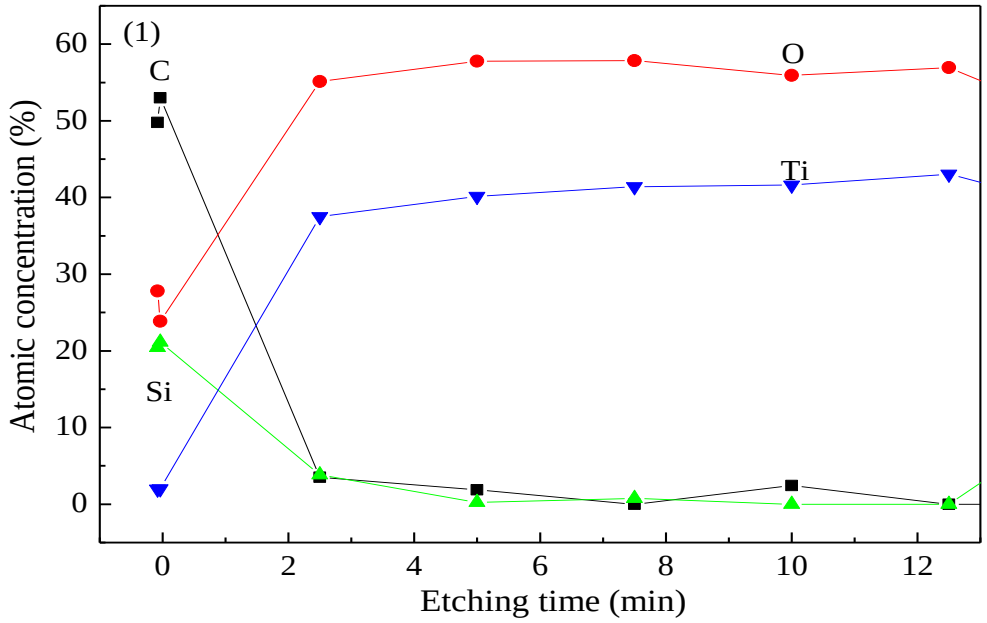

Figure 6.5b XPS depth profile of sample 1

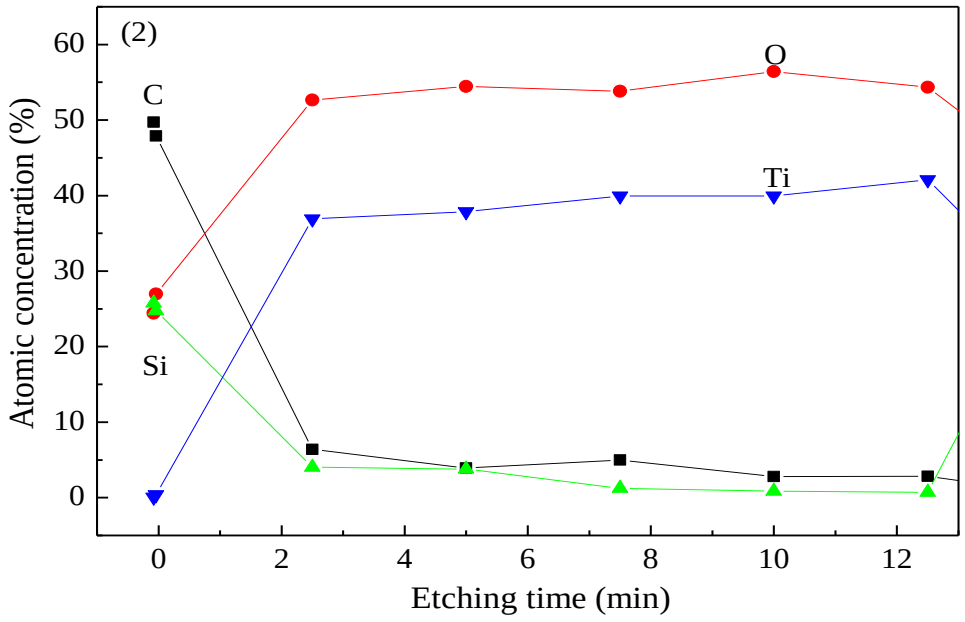

Figure 6.5c XPS depth profile of sample 2

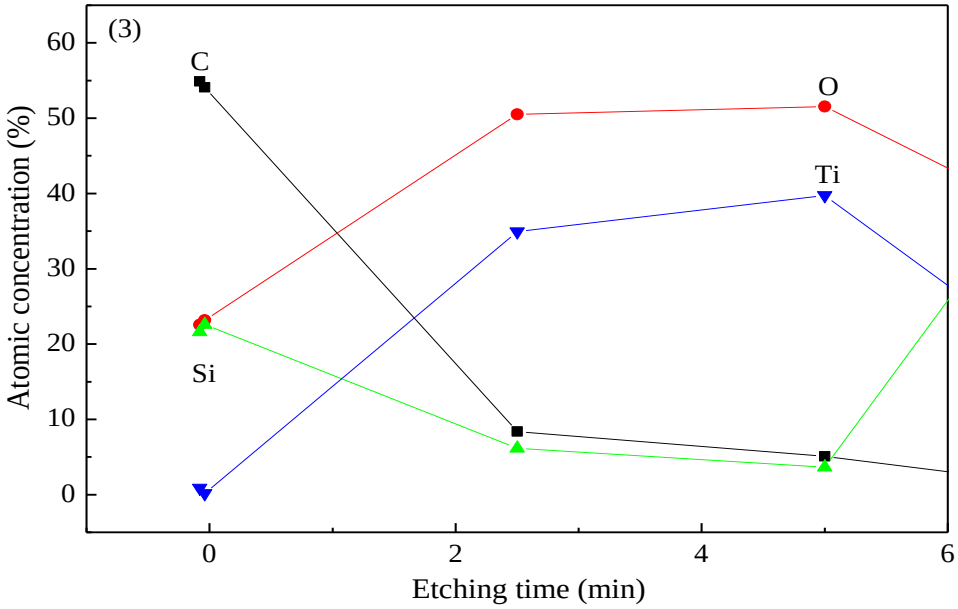

Figure 6.5d XPS depth profile of sample 3

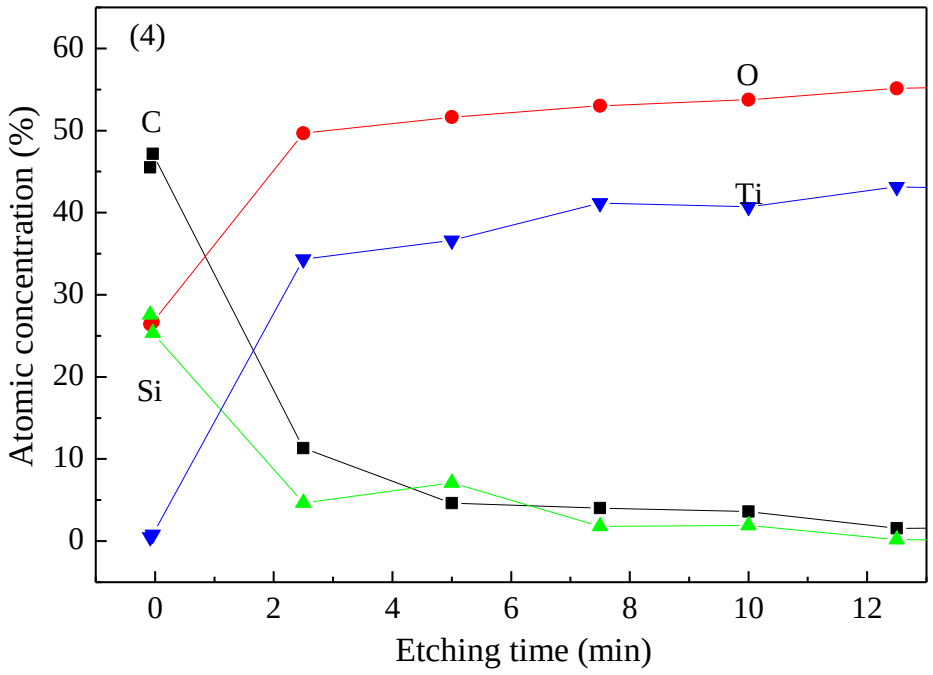

Figure 6.5e XPS depth profile of sample 4

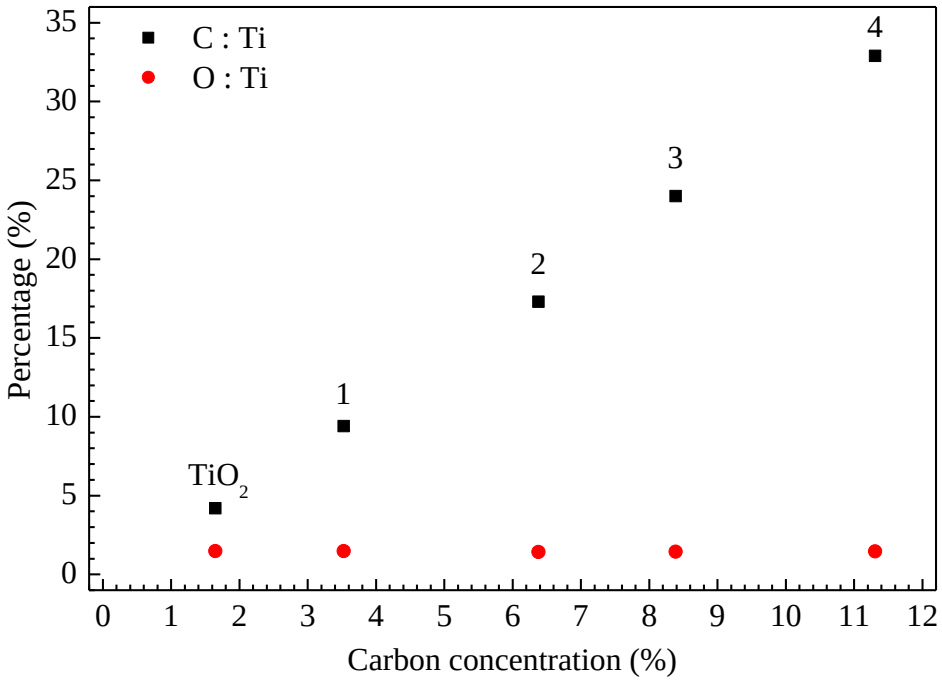

Figure 6.6 The atomic ratios of C:Ti and O:Ti against carbon concentration in 5 samples

6.3.3 Magnetic properties

The magnetic properties of four C-doped TiO_2 thin films of 100 nm thick and size 5 x 5 mm^2 were investigated using VSM measurement. Figure 6.7 shows the in-plane M-H plot of C-doped TiO_2 thin films at room temperature. The number of M-H loops from 1 to 4 corresponds to the position of samples labeled in Figure 6.2, i.e. loop 1 refers to the closest sample to the target while loop 4 refers to the farthest sample away from it. The remanent magnetization of sample 1, 2, 3 and 4 are 0.1 memu, 0.4 memu, 0.6 memu and 1.0 memu.

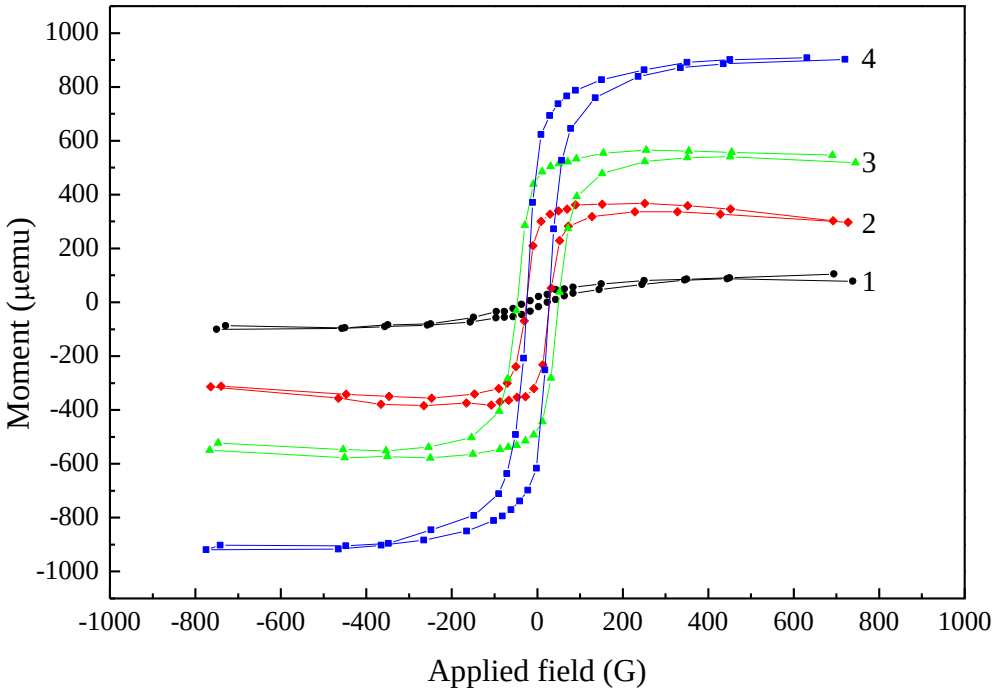

Figure 6.7 M-H plot of C-doped TiO2 thin films at room temperature while in-plane field was applied

6.4 Discussion

By comparing the XRD full scans of the samples before and after the C doping, the structure of C- doped TiO_2 thin films remains the same. Apparently there is no structural change after doping. Our C-doped TiO_2 films are transparent and strongly textured, showing only the (004) diffractions of the anatase structure.

The relative composition analysis of film was based on the photoelectron spectra of the C 1s, Ti 2p and O 1s collected in XPS. A survey scan was run over each sample to locate the elements present at the surface of the film. The photoelectron spectra of the C 1s, Ti 2p, O 1s and Si 2p were collected in XPS. Since all samples have been exposed in

air, their surfaces have been contaminated. There was relatively high carbon content (50%) at the beginning of all depth profiles in Figure 6.5, including pure TiO_2 film. Other than carbon, silicon was also found on the surface. It was contributed from the vacuum grease used during the VSM measurements. The relative contents of C and Ti in the films are determined by obtaining depth profiles with respect to etching time shown in Figure 6.5. Based on the etching rate of 4 keV Ar ion beam on silicon is 4 nm min^{-1}, the depth of C doped in TiO_2 layer is about 50 nm.

According to Figure 6.6, sample placed at longer distance from the graphite target yields higher C concentration. Owing to the incident angle of the Ar ion beam is 45°, area right in front of the target cannot be reached by the ion beam along the horizontal level. The chance of exposing to the ion beam increases as getting further away from the target. There should an optimal area with the highest possibility of doping carbon. However, the carbon content decreases again once passing-by the optimal area. Based on the tread of C concentration created, it is believed that sample placed very close to the target as sample 1 has the least chance to be the sputtered carbon.

Samples of pure TiO_2 were confirmed to be non-magnetic under VSM investigation before the C doping. As the C-doped TiO_2 samples are expected to be free of ferromagnetic precipitates, any ferromagnetic properties observed should be considered as intrinsic to the C-TiO_2 matrix.

Upon ferromagnetic properties, in-plane VSM loops measured at room temperature were shown in Figure 6.7. We have observed a significant room temperature magnetic behaviour in C-doped TiO_2 films, which seemed to have a correlation with C content in the samples. The higher the C content the sample has, the stronger the magnetization of it is. As mentioned in the theory, C has spin-polarized 2p states in the band gap generating magnetic moment and electron density may play an important role for the appearance of ferromagnetism. The magnetic coupling generated among adjacent C sites strongly depends on the distance between them (C…C). They will be at a nonmagnetic state if the distance is too short. On the contrary, a long distance between them will lead to a paramagnetic state. That means the ferromagnetism in the matrix not only simply based on the atomic ratio of C:Ti in the samples, but also the location of C-Ti-C bond, too. When the C content can be contributed by both C-Ti-C bond and C-C bond in graphite particulates, a further step is needed to verify on the distribution of C in the matrix. Although the carbon content has been verified by XPS, the magnetization per C atom cannot be determined as the content of C-Ti-C remains unknown.

This experimental result indicates that magnetic ions are not essential to obtain DMS and also eliminates the magnetic behaviour induced by impurity clustering. According to the XPS and the VSM results, sample consists of higher C concentration showed a stronger remanent magnetization. There is still a muzzle on the magnetization

per C atom generated in this system. Nevertheless, appropriately C-doped TiO_2 films can thus be a n-type dilute magnetic semiconductor and a useful material for future spintronics devices.

6.5 References

1. N.H. Hong, A. Ruyter, W. Prellier & J. Sakai, "Room temperature ferromagnetism in anatase $Ti_{0.95}Cr_{0.05}O_2$ thin films: Clusters or not?" *Appl. Phys. Lett.*, vol. 85, no. 25, p. 6212, 2004.
2. Y.X. Wang, H. Liu, Z.Q. Li, R. K. Zheng & S. P. Ringer, "Role of structural defects on ferromagnetism in amorphous Cr-doped TiO_2 films," *Appl. Phys. Lett.*, vol. 89, no. 4, p. 042511, 2006.
3. Z. Wang, J. Tang, H. Zhang, V. Golub, L. Spinu & L. D. Tung, "Ferromagnetism in chromium-doped reduced-rutile titanium dioxide thin films," *J. Appl. Phys.*, vol. 95, no. 11, p. 7381, 2004.
4. Y.J. Kim, S. Thevuthasan, T. Droubay, A. S. Lea, C. M. Wang, V. Shutthanandan, S. A. Chambers, R. P. Sears, B. Taylor, & B. Sinkovic, "Growth and properties of molecular beam epitaxially grown ferromagnetic Fe-doped TiO_2 rutile films on TiO2(110)," *Appl. Phys. Lett*, vol. 84, no. 18, p. 3531, 2004.
5. S. Duhalde, M. F. Vignolo, F. Golmar, C. Chiliotte, C. E. R. Torres, L. A. Errico, A. F. Cabrera, M. Rentería, F. H. Sánchez, & M. Weissmann, "Appearance of room-temperature ferromagnetism in Cu-doped $TiO_{2-\delta}$ films," *Phys. Rev. B*, vol. 72, p. 161313, 2005.
6. H. Pan, J. B. Yi, L. Shen, R. Q. Wu, J. H. Yang, J. Y. Lin, Y. P. Feng, J. Ding, L. H. Van, & J. H. Yin, "Room-Temperature Ferromagnetism in Carbon-Doped ZnO," *Phys. Rev. Lett.*, vol. 99, no. 12, p. 127201, 2007.
7. T. S. Herng, S. P. Lau, C. S. Wei, L. Wang, B. C. Zhao, M. Tanemura & Y. Akaike, "Stable ferromagnetism in p-type carbon-doped ZnO nanoneedles," *Appl. Phys. Lett.*, vol. 95, no. 13, p. 133103, 2009.
8. H. Pan, Y. P. Feng, Q. Y. Wu, Z. G. Huang & J. Lin, "Magnetic properties of carbon doped CdS: A first-principles and Monte Carlo study," *Phys. Rev. B*, vol. 77, no. 12, p. 125211, 2008.
9. Q. K. Li, B. Wang, Y. Zheng, Q. Wang, and H. Wang "First-principles study of the electronic structure and the associated magnetism of carbon-doped TiO2," *Phys. Status. Sol. (rrl)*, vol. 1, no. 5, p. 217, 2007.
10. C. Di Valentin, G. Pacchioni & A. Selloni, "Theory of Carbon Doping of Titanium Dioxide," *Chem. Mater.*, vol. 17, no. 26, p. 6656, 2005.
11. K. Yang, Y. Dai, B. Huang & M. H. Whangbo, "On the possibility of ferromagnetism in carbon-doped anatase TiO2," *Appl. Phys. Lett.*, vol. 93, no. 13, p. 132507, 2008.

Chapter 7
Cobalt ferrite and LSMO heterojunction

In this chapter, an experimental study on the magnetotransport properties in all-oxide heterostructures is performed. A ferrimagnetic oxide, cobalt ferrite $CoFe_2O_4$ (CFO), replaces CTO for the n-type layer. Magnetic modulation in an all-oxide heterojunction is demonstrated.

The following material properties were considered when deciding to use CFO.

(a) a high saturation magnetization,

(b) a high Néel/Curie temperature for the ferri/ferromagnetic phase, and

(c) a cubic structure with highly lattice match is preferred

CFO is one of the materials that satisfies all the above requirement and we have experience on fabricating CFO thin films by PLD [1-2].

7.1 Introduction

Cobalt ferrite (CFO) has been widely applied in fields of science/technology that include conventional magnetic recording media, microwave devices or even permanent magnets [1-2]. Due to its exceptional magnetoelastic, magnetotransport, magnetooptical, photomagnetic, electronic, and magnetic properties, CFO has also been proposed for applications in magnetic tunnel junctions [3], hybrid data storage [4], for magnetooptical media [5], noncontact force and torque sensors [6] and as anode

materials for Li-ion batteries [7]. Magnetic and magnetoelastic properties of CFO can be fine-tuned by appropriate cation substitution [3,8–10] and magnetic annealing [11] in order to fulfill the requirements of application.

Spinel ferrites have a spinel-like structure with the molecular formula AB_2O_4, where A^{2+} and B^{3+} are the divalent and trivalent cations occupying tetrahedral (A) and octahedral (B) interstitial positions of the fcc lattice formed by O^{2-} ions. The magnetic properties of these oxides depend on the type of cations and their distribution between the two interstitial positions. CFO is a well-known inverse spinel with Co^{2+} ions on B sites and Fe^{3+} ions distributed equally among A and B sites.

7.2 Experimental approach

Heteroepitaxial spin-valve junctions of CFO/LSMO were deposited on LNO buffered (001) oriented $(LaAlO_3)_{0.3}(SrAl_{0.5}Ta_{0.5}O_3)_{0.7}$ (LSAT) by PLD. Standard "Current-Perpendicular-to-Plane"(CPP) geometry shown in Figure 7.1 was employed to investigate the magnetoresistance properties of these heteroepitaxial spin-valve junctions. $LaNiO_3$ layer acts as a bottom electrode (10^{-3}ohm-cm) that allows an evenly distributed in-plane current flowing through the junction. The contribution of anisotropic magnetoresistance (AMR) effect can thus be minimized. Ferromagnetic LSMO and ferrimagnetic CFO serve as a soft magnetic layer and hard magnetic layer in this pseudo-spin valve.

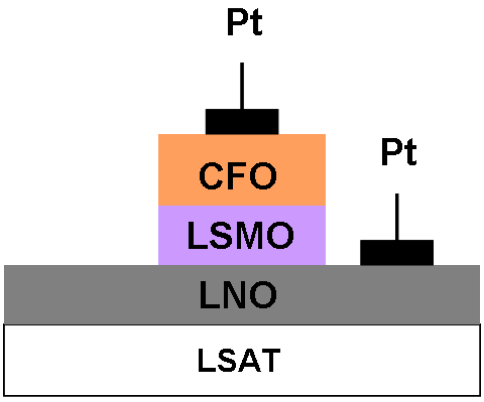

Figure 7.1 Standard "Current-Perpendicular-to-Plane"(CPP) geometry

A 200 nm thick bottom electrode LNO were fabricated on the LSAT (001) substrate, at a substrate temperature of 650 ℃ and an oxygen pressure of 150 mTorr. This layer was then annealed *in-situ* at the growth temperature for 20 min to improve the crystallinity. LSMO and CFO were deposited on LNO buffered LSAT, at an oxygen pressure of 150 mTorr with a substrate temperature of 650 ℃ and 600 ℃ respectively. These layers were annealed *in-situ* at 10 Torr of O_2 for 5 min and then naturally cooled down to room temperature. The junction size of 0.5 x 0.5 mm^2 is confined by a shadow mask during the fabrication. Pt electrode of 0.2 mm diameter was then deposited on top of CFO/LSMO/LNO buffered LSAT substrate.

The MR was measured by four point probe measurements with a constant current of 0.1 mA. The magnetic properties of CFO/LSMO LNO buffered LSAT of size 0.5 x 0.5 mm^2 are analyzed by VSM. Both MR and VSM measurement was performed with a applied magnetic field perpendicular to the current flows in the junctions.

7.3 Results and discussions

The magnetic properties of the 60 nm LSMO film fabricated on LNO buffered LAST is confirmed to be consistent with the one grown on LAO discussed in Chapter 3. Figure 7.2 shows the in-plane M-H measurement of the layer at 100 K. Both the saturation magnetic moment was about 500 μemu while the coercive field of the film was about 200 G.

Meanwhile, Figure 7.3 shows the M-H hysteresis loop of 15 nm CFO single layer. Its feature matched with those has been published in literatures [12-13]. Our CFO film has a the coercive field 1500 G and reaches saturation at 4000 G with magnetic moment 100 μemu.

Double coercivity behavior of the junction was observed at 100 K as shown in Figure 7.4. The hysteresis loops (blank in colour) shows two distinct coercive fields, which is contributed from two different magnetic layers: “soft” LSMO layer (minor loop at lower field region) and “hard” CFO layer (major loop at higher field region) respectively.

Figure 7.5 shows a typical magnetoresistance curves with the peaks having good consistency with the coercive field of the M-H hysteresis loop. As the magnetic field was decreased from 5000 to -80 G, the MR ratio of these heteroepitaxial junctions is 6%. These changes are corresponded to the switching of LSMO

magnetization, which gives result in the change of parallel to anti-parallel magnetization in the CFO and LSMO layer. By further decrease in the magnetic field, the alignment of spin between CFO and LSMO becomes parallel again, and is attributed to the switching from high resistance state to low resistance state.

Thus, magnetic modulation of charge carrier transportation has been demonstrated in this all-oxide CFO/LSMO junction. Further investigation of this junction characteristic is needed to determine the exact switch mechanisms. For example, we are not able to conclude, at least at the present stage, the MR effect is OMR, AMR or TMR.

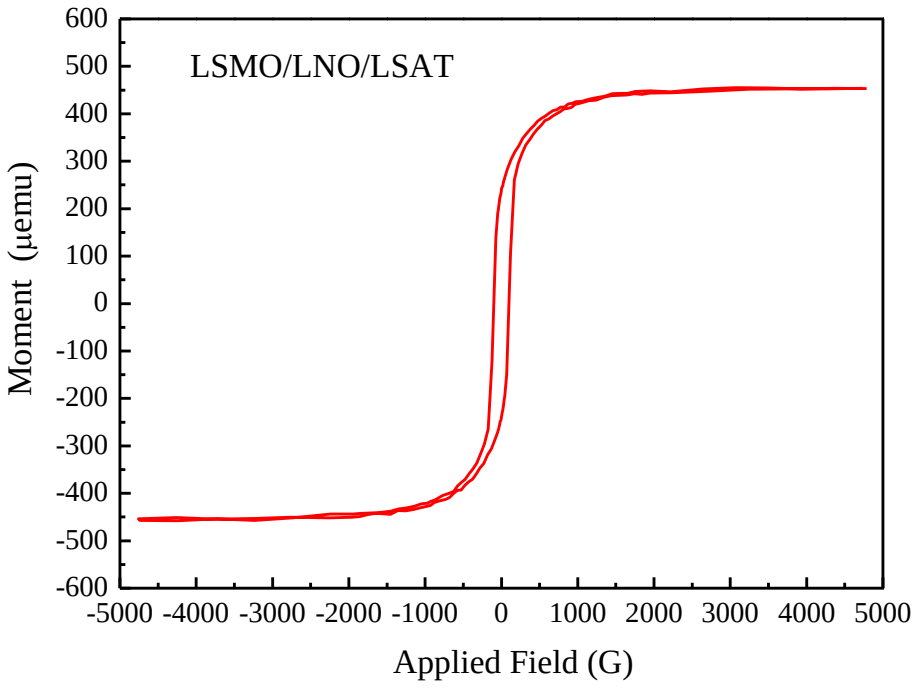

Figure 7.2 M-H plot of LSMO on LNO buffered LSAT at 100 K

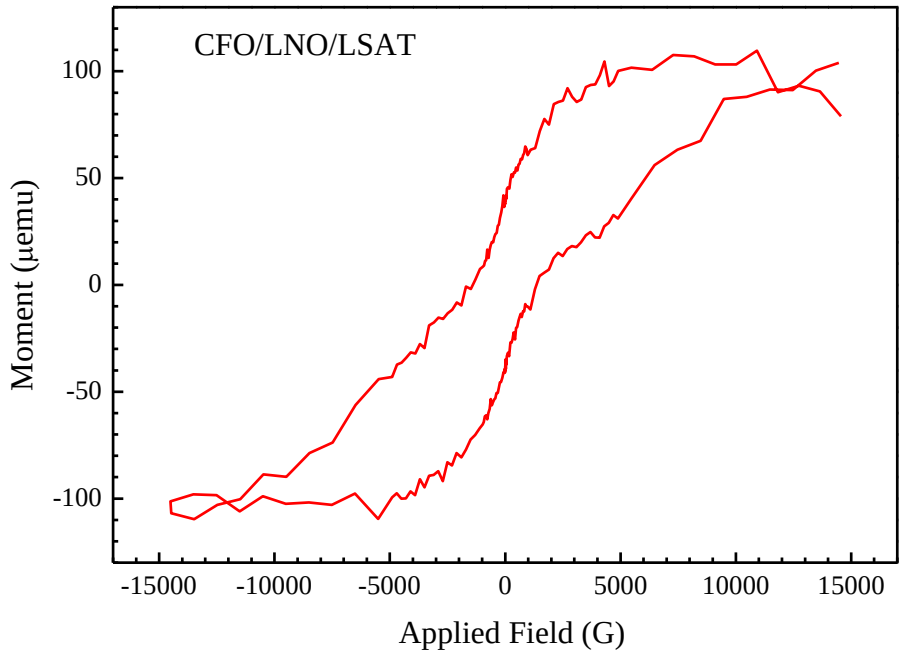

Figure 7.3 M-H plot of CFO on LNO buffered LSAT at 100 K

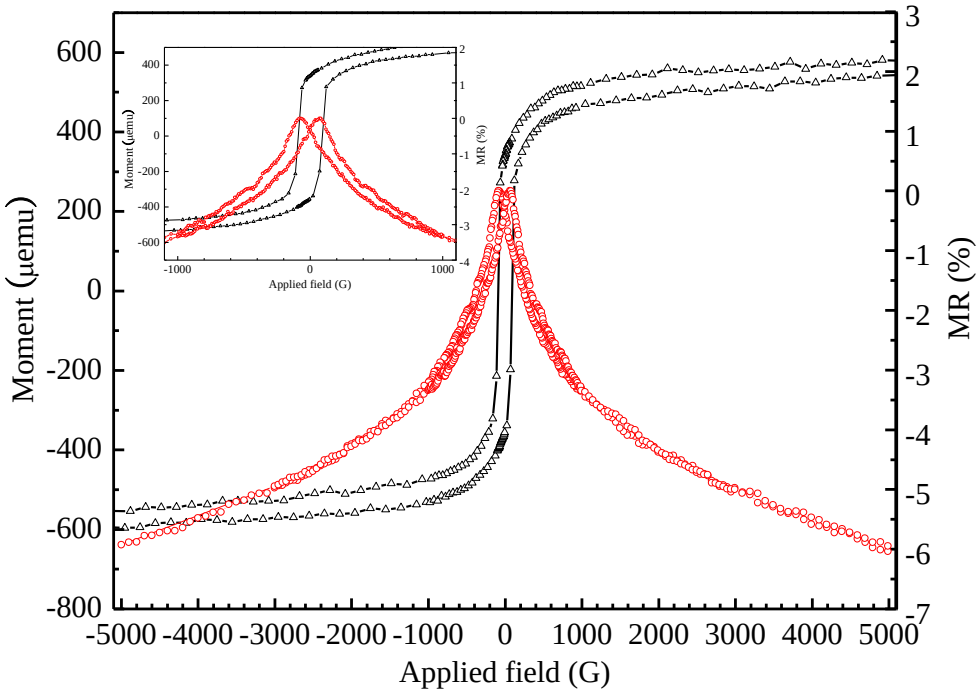

Figure 7.4 The hysteresis loops and magnoetoresistance of CFO/LSMO/LNO junction at 100 K. The inset is the hysteresis loops of CFO and LSMO grown on LNO/LSAT. All experiment is measured at 100 K.

7.4 References

1 J. X. Zhang, J. Y. Dai, W. Lu, H. L. W. Chan, B. Wu & D. X. Li, “A novel nanostructure and multiferroic properties in Pb(Zr0.52Ti0.48)O3/ CoFe2O4 nanocomposite films grown by pulsed-laser deposition”, *J. Phys. D: Appl. Phys.*, vol. 41, p.235405, 2008.

2 J. X. Zhang, J. Y. Dai, C. K. Chow, C. L. Sun, V. C. Lo, & H. L. W. Chan, “Magnetoelectric coupling in CFO /PZT heteroepitaxial thin film structure ”, *Appl. Phys. Lett.*, vol. 92, p. 022901, 2008.

3 A.V. Ramos, T.S. Santos, G. X. Miao, M.-J. Guittet, J.-B. Moussy, & J. S. Moodera, "Influence of oxidation on the spin-filtering properties of $CoFe_2O_4$ and the resultant spin polarization," *Phys. Rev. B,* vol. 78, p. 180402, 2008.

4 A. K. Giri, E. M. Kirkpatrick, P. Moongkhamklang, S. A. Majetich, & V.G. Harris, "Photomagnetism and structure in cobalt ferrite nanoparticles," *Appl. Phys. Lett.*, vol. 80, p. 2341, 2002.

5 L. Stichauer, G. Gavoille, & Z. Simsa, "Optical and magneto-optical properties of nanocrystalline cobalt ferrite films," *J. Appl. Phys.*, vol. 79, p. 3645, 1996.

6 J. A. Paulsen, A. P. Ring, C. C. H. Lo, J. E. Snyder, & D. C. Jiles, "Manganese-substituted cobalt ferrite magnetostrictive materials for magnetic stress sensor applications," *J. Appl. Phys.*, vol. 97, p. 044502 , 2005.

7 Y.-Q. Chu, Z.-W. Fu, & Q.-Z. Qin, "Cobalt ferrite thin films as anode material for lithium ion batteries," *Electrochim. Acta.*, vol. 49, p. 4915, 2004.

8 S. H. Song, C. C. H. Lo, S. J. Lee, S. T. Aldini, J. E. Snyder, & D. C. Jiles, " Magnetic and magnetoelastic properties of Ga-substituted cobalt ferrite," *J. Appl. Phys.*, vol. 101, p. 09C517, 2007.

9 S. J. Lee, C. C. H. Lo, P. N. Maltage, S. H. Song, Y. Melikhov, J. E. Snyder, & D. C. Jiles, "Magnetic and magnetoelastic properties of Cr-substituted cobalt ferrite," *J. Appl. Phys.*, vol. 102, p. 073910, 2007.

10 N. Ranvah, Y. Melikhov, I. C. Nlebedim, D. C. Jiles, J. E. Snyder, A. J. Moses, & P. I. Williams, "Temperature dependence of magnetic anisotropy of germanium/cobalt cosubstituted cobalt ferrite,"*J. Appl. Phys.*, vol. 105, p. 07A518 , 2009.

11 C. C. H. Lo, A. P. Ring, J. E. Snyder, & D. C. Jiles, "Improvement of magnetomechanical properties of cobalt ferrite by magnetic annealing**,**" *IEEE Trans. Magn.*, vol. 41, no. 10, p. 3676, 2005.

12 A. Raghunathan, I. C. Nlebedim, D. C. Jiles, & J. E. Snyder, " Growth of crystalline cobalt ferrite thin films at lower temperatures using pulsed-laser deposition technique," *J. Appl. Phys.*, vol. 107, p. 09A516, 2010.

13 S.C. Sahoo, N. Venkataramani, Shiva Prasad, Murtaza Bohra, & R. Krishnan,

"Pulse Laser Deposited Nanocrystalline Cobalt Ferrite Thin Films," *J. Nanosci. Nanotechnol.*, vol. 10, p. 3112, 2010.

Chapter 8 Conclusions

We have intensively studied spin-polarized transport in all-oxide junction and its potential application in spintronic devices. Firstly, we have addressed the structural and electrical properties of the Co doped TiO_2/LSMO heterostructure. Under optimized fabrication conditions the $Co_xTi_{1-x}O2/La_{0.7}Sr_{0.3}MnO_3$ [x = 0.05 and 0.1] junction revealed a heteroepitaxial relationship of (004) CTO||(001)LSMO||(001)LAO. Electrical characterization of these p-n junctions yielded excellent rectifying characteristics with a current rectifying ratio over 1000 at room temperature. We have demonstrated that spintronic devices based on heteroepitaxial growth of room temperature ferromagnetic oxides are possible.

Since the mechanism of ferromagnetic properties of cobalt doped titianium dioxide is still in controversy. Some authors claimed that it arises from Co clusters. Other groups suggested that it originates from the uniform distribution of Co atoms which have substituted for Ti cations in the anatase films. Several dopants, such as Co, Cr, Fe, have been utilized to realize ferromagnetism above room temperature. However, it is more worth while to study carbon doped TiO_2 which is also found to be a room ferromagnetic material and can replace Co-doped TiO_2 for the future study.

Carbon is a non-ferromagnetic material. The issue of ferromagnetism due to clustering of dopant therefore does not occur in a carbon doped TiO_2 system. Our

investigation has clearly demonstrated the prominent ferromagnetic properties of C-TiO_2 and paved the way for further development of C-TiO_2 for use in spintronics devices.

For spin valve application, it is important to verify the magnetic properties of the heterojunction by measurement using Vibrating Sample Magnetometer (VSM) with a higher sensitivity and measure the MR in CPP configuration. Such configuration have been applied to the investigation of CFO/LSMO heterojunction on LNO buffered LSAT substrate. We have demonstrated the double coercivity and the MR properties of this junction device. Although a spin valve nature has been shown in CFO/LSMO heterojunction, it is not a proper p-n junction consisting of magnetic property. Electrical modulation at the CFO/LSMO junction has not been demonstrated. The near insulating characteristic of CFO is the major obstacle. In the future we will attempt to dope CFO with other transition elements such as indium to enhance the conductivity of CFO.

All together we have identified and studied three n-type ferromagnetic semiconducting oxides. They all have been successfully fabricated on LSMO to form heteroepitaxial junctions. Although we have yet to demonstrate simultaneous electric and magnetic switching in these junctions, their separated and independent electric and magnetic switching capabilities have been satisfactorily revealed. Indeed these heterojunctions are very promising for developing future spintronic devices.